BULGARIAN CHEMICAL COMMUNICATIONS

2011 Volume 43 / Number 4

Journal of the Chemical Institutes
of the Bulgarian Academy of Sciences
and of the Union of Chemists in Bulgaria

Bulgarian Chemical Communications, Volume 43, Number 4 (pp 477 – 482) 2011

Effect of lanthanum on the activity and thermal stability of copper-cobalt oxide catalysts supported on alumina

D. D. Stoyanova*, G. M. Ivanov, M. S. Khristova

Institute of General and Inorganic Chemistry, Bulgarian Academy of Sciences, Acad. G. Bontchev Str., 11, 1113 Sofia, Bulgaria

Received November 29, 2010; Accepted March 4, 2011

La-modified alumina-supported copper oxide and cobalt oxide catalysts were investigated. The catalyst samples were prepared by impregnation of supports (γ-Al_2O_3 or La-modified γ-Al_2O_3) with a mixed aqueous solution of Cu and Co nitrates. The samples were characterized by ICP analysis, X-ray powder diffraction (XRD) and BET method. The catalytic reduction of NO by CO and the catalytic oxidation of CO and C_6H_6 by O_2 were carried out over non-modified and La-modified catalysts. The modification of γ-Al_2O_3 support with La at a loading below 3 wt. % has a positive effect on the catalytic performance of supported Cu-Co oxide catalysts. Lanthanum plays a stabilizing role on the specific surface area of the carriers and Cu-Co oxide catalysts; the addition of La suppresses the α-transformation of the alumina support and its interaction with the active Cu-Co oxide phase to produce aluminates. The modification of the support with La prevents the intercalation of Cu ions into the γ-Al_2O_3 during the impregnation with Cu-Co nitrates. Thus, the active Cu-Co oxide spinel supported on La/Al_2O_3 has a higher Co:Cu ratio, which is close to that in the stoichiometric $CuCo_2O_4$ spinel. La-modified catalysts have higher activity in the NO+CO, CO+O_2 and C_6H_6+O_2 reactions, compared to the non-modified catalysts. Incorporation of La into the support does not change the energy level of catalytically active sites but rather increases the number of these sites.

Keywords: La-modified alumina, Cu-Co oxide spinel catalysts, NO reduction, oxidation of CO and C_6H_6 by O_2

.

1. INTRODUCTION

Transition metal oxides are active catalysts for a wide range of reactions for environmental protection such as NO reduction, CO and hydrocarbons (HC) oxidation [1]. On the other hand, lanthanum oxide exerts considerable influence on the thermal stabilization of alumina [2] and modification by La leads to a high catalytic activity in the CH_4 reforming with CO_2 [3]. It was found out [4] that Mn and Cu performance was better, when dispersed onto alumina in the presence of La and that La increased the insertion of copper into alumina. The addition of La_2O_3 promotes the dispersion of the active phase all over the alumina support [5-7], thus decreasing the degree of crystallinity and decreasing the particle size. Barrera *et al*. [8] established that the La_2O_3 in the Pd/Al-La catalysts, prepared by the sol–gel method, promotes the oxidation of Pd and dissociation of NO at low temperatures favoring the formation of N_2. A lanthanum-promoted Pd/Al_2O_3 catalyst [9] shows a higher activity for the hydrogenation of phenol with H_2 than non-promoted Pd/Al_2O_3 catalyst and the dispersion of Pd could strongly depend on the dispersion of lanthanum on Al_2O_3. It was found out that Cu-Co oxide spinels such as $Cu_xCo_{(3-x)}O_4$ [10, 11] and $CuCo_2O_4$/γ-Al_2O_3 [12] are catalysts demonstrating high activity in the reduction of NO with CO. The presence of copper ions in the impregnation solution sharply lowers the adsorption capacity of alumina with respect to the cobalt ion from solution in case of depositing Cu-Co oxide spinels onto γ-Al_2O_3 [13]. As a result of this the so called "chromatographic effect" appears, which is due to the stronger selective adsorption of one of the ions in the solution on the surface of the support.

The purpose of the present work was to investigate the process of copper oxide and cobalt oxide deposition on alumina and on La-modified alumina as well as the catalytic reactions of NO reduction with CO and oxidation of CO and C_6H_6 by O_2 on these catalysts.

2. EXPERIMENTAL

Catalyst preparation

The support γ-Al_2O_3 (Rhone-Poulenc) has a specific surface area of 260 m^2g^{-1}. The La-modified samples were prepared by impregnation of γ-Al_2O_3

* To whom all correspondence should be sent:
E-mail: dsto@svr.igic.bas.bg

(sieve fraction with grain size 0.3-0.6 mm) with an aqueous solution of lanthanum nitrate (the content of La was 1.31 g La/100 cm^3). The catalyst samples were prepared by impregnation of the supports (γ-Al_2O_3 or La-modified γ-Al_2O_3) with a mixed aqueous solution of the nitrates of Cu and Co. The concentrations used were (7.04 g Cu + 13.98 g Co)/100 cm^3 in order to ensure a ratio Co:Cu = 1.99, which is close to the weight ratio Co:Cu = 1.85 for the stoichiometric $CuCo_2O_4$ spinel. Separate samples of the so prepared catalysts were dried in air for 2 h at 120°C and calcined for 3h at 550°C and at 1050°C. In this way, the following samples were obtained:

A_550, γ -Al_2O_3 → calcination at 550°C;

A_1050, γ -Al_2O_3 → calcination at 1050°C;

LA_550, obtained by impregnation of γ-Al_2O_3 with aqueous solution of lanthanum nitrate → calcination at 550°C;

LA_1050, obtained by impregnation of γ-Al_2O_3 with aqueous solution of lanthanum nitrate → calcination at 1050°C;

SA_550, obtained by simultaneous impregnation of γ-Al_2O_3 with copper and cobalt present in the impregnating solutions → calcination at 550˚C;

SA_1050, obtained by simultaneous impregnation of γ-Al_2O_3 with copper and cobalt present in the impregnating solutions → calcination at 1050˚C;

SLA_550, obtained by impregnation of γ-Al_2O_3 with aqueous solution of lanthanum nitrate → calcination at 550°C → impregnation with copper and cobalt present in the impregnating solutions → calcination at 550°C;

SLA_1050, obtained by impregnation of γ-Al_2O_3 with aqueous solution of lanthanum nitrate → calcination at 1050°C → impregnation with copper and cobalt present in the impregnating solutions → calcination at 1050°C.

Catalyst characterization

The La, Cu and Co contents in the impregnating solutions and in the synthesized catalysts were determined using inductively coupled plasma atomic emission spectrometry (ICP-AES) on a spectral analyzer JY38 (Jobin Yvon, France).

X-ray diffraction (XRD) data were obtained using a Bruker D8 Advance diffractometer with Cu-Kα radiation and SolX detector.

The texture characteristics were determined by low-temperature (77.4 K) nitrogen adsorption in a conventional volumetric apparatus. The specific surface area was evaluated by the single-point BET method.

Catalytic activity measurements

The catalytic activity experiments were carried out in a continuous flow reactor described previously [10]. The NO reduction with CO was investigated in the temperature range 25-500°C. The catalytic activity tests were performed with a NO+CO+Ar feed gaseous mixture, containing 1200 ppm NO and 1200 ppm CO. Argon was used as a carrier gas at a total gaseous hourly space velocity of 433 cm^3min^{-1} (GHSV 33 000 h^{-1}). A 1 cm^3 sample of a catalyst (0.3 - 0.6 mm sieve fraction) was charged in the reactor representing a quartz tube of internal diameter d=10 mm. The concentrations of NO and CO were continuously measured by gas analyzers. The concentrations of NO and CO in the converted mixture were controlled using the UNOR 5 –Maihak and the CO_2 – using the Infralyt 2106 gas analyzer. The concentrations of NO, CO and CO_2 were continuously measured by gas analyzers and the data were collected on a CSY-10 personal data station. Specord 75 IR spectrophotometer with a 1 m folded path gas cell (Specac) was used for determination of the N_2O content at the outlet. The N_2 concentration in the outlet gas was determined on the basis of the material balance with respect to NO consumption. Before the catalytic activity test, the catalysts were treated thermally in an Ar flow at 500°C for 1 h. Afterwards the catalyst bed temperature was decreased down to room temperature. The chronology of this set of experiments involves a reaction step (NO+CO+Ar) and an isothermal desorption step (Ar flow) carried out at successively higher and higher temperatures in the range from 50 to 500°C. Temperature programmed reaction (TPR) experiments with NO+CO+Ar feed mixture were carried out on the same catalytic apparatus at a heating rate of 13°C/min in an Ar flow (440 cm^3 min^{-1}) continuously fed into the reactor. The catalytic tests for CO+O_2 and C_6H_6+O_2 reactions were performed in an analogous flow apparatus at a carrier gas (Ar flow) space velocity of 20 000 h^{-1}. The inlet and the outlet concentrations of CO and CO_2 were controlled on an Infralyt 2106, NDIR gas analyzer. A Pye Unicam (UK) gas chromatograph with a FID detector was used for the C_6H_6 converted mixture analysis. A dosing pump Ismatex MS2/6 (Switzerland) was utilized to control the feed concentrations of CO and C_6H_6.

Table1. Chemical composition, BET specific surface areas and phase composition of the samples.

Sample	Metal content (wt. %)			Co:Cu	S_{BET} (m^2 g^{-1})	Phase composition
	La	Cu	Co			
A_550	-	-	-	-	190	γ-Al_2O_3
LA_550	0.30	-		-	172	γ-Al_2O_3
A_1050	-	-		-	40	θ-Al_2O_3, α-Al_2O_3
LA_1050	0.20	-	-	-	109	θ-Al_2O_3
SA_550	-	5.69	4.68	0.82	129	γ-Al_2O_3, Co_3O_4 ($CuCo_2O_4$)
SLA_550	0.23	4.23	8.05	1.90	138	γ-Al_2O_3, $CuCo_2O_4$
SA_1050	-	2.74	3.65	1.33	32	α-Al_2O_3, $CuAl_2O_4$ and $CoAl_2O_4$
SLA_1050	0.15	2.52	3.98	1.58	69	θ-Al_2O_3, α-Al_2O_3, traces of $CuAl_2O_4$ and $CoAl_2O_4$

3. RESULTS AND DISCUSSION

The data in Table 1 show that the Cu and Co contents for the La-modified catalyst differ from those obtained for the non-modified catalyst. The Co:Cu weight ratio for the unmodified SA_550 sample (0.82) is lower than that in the (Cu+Co) impregnating solution (1.99). This discrepancy in

the Co:Cu ratios was attributed to the so called "chromatographic effect" of the support [12] and was related to the different affinities of the Al_2O_3 support towards the Cu and Co ions in the impregnating solution. Doping the support with La prevented this effect and the Co:Cu ratio for La-modified catalyst SLA_550 was 1.90, which was close to that in the impregnating solution (1.99).

Therefore, the modification with La is an efficient way to eliminate the selective adsorption of metal ions during impregnation of alumina with nitrate solution, which is important for the multi-component oxide catalyst preparations. The data in Table 1 clearly reveal the stabilization role of La on the specific surface area of the carriers. The surface area of a La-doped catalyst aged at 1050°C (SLA_1050) is twice as higher than that of the corresponding non-doped with La (SA_1050) catalyst. The XRD data on the support (A_550) indicate the presence of γ-Al_2O_3 phase and this pure γ-Al_2O_3, treated at 1050°C (A_1050), is being transformed into θ-Al_2O_3 and α-Al_2O_3 phases. The La-modified alumina (LA_1050) did not contain any α-Al_2O_3 phase, as it can be seen in Table 1. No La-containing phases are observable in the XRD pattern of La-modified samples and the probable reason for it is the low concentration of the well-dispersed La on the surfaces of the supports [14, 6].

Reflections due to aluminates $CuAl_2O_4$ and $CoAl_2O_4$ emerge from the XRD patterns of both non-doped and La-doped Cu-Co catalysts. However, aluminate formation is much less pronounced in the case of the La-modified sample SLA_1050. This implies that the modification with La hampers the interaction of the parent alumina with the active Cu-Co phase. This is in agreement with the findings by Bettman *et al*. [15], who reported that aluminate phases did not form at temperatures lower than 1100°C, when the La_2O_3 content was less than 4 wt.%. The catalytic

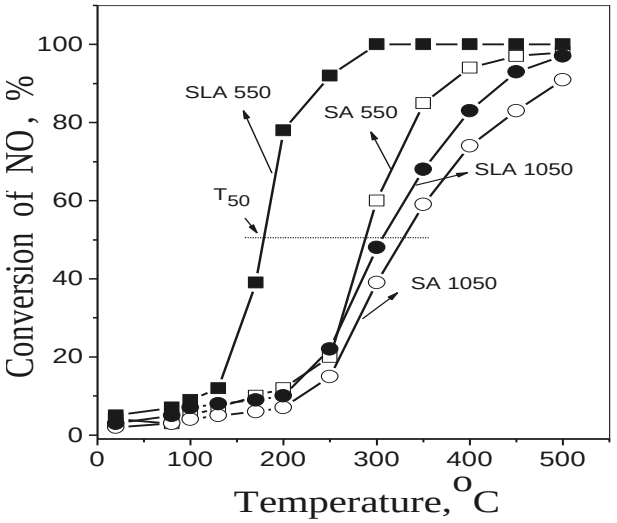

Fig. 1. Temperature dependence of the conversion degree of NO with samples: La-modified - SLA_550 (■) and SLA_1050 (●) and non-modified SA_550 (□) and SA_1050 (○).

reduction of NO by CO and the catalytic oxidation of CO and C_6H_6 by O_2 were carried out on non-modified SA_550 and SA_1050 samples and also on La-modified SLA_550 and SLA_1050 catalysts. The NO conversion – temperature data are presented in Figure 1.The La-modified catalyst has a higher activity in the NO+CO reaction, compared to non-modified catalysts. The temperature T_{50} for the modified catalyst SLA_550 is by 100°C lower than that measured with the unmodified catalyst SA_550. Modification of the γ-Al_2O_3 support with La has a positive effect on the activity of Cu-Co catalysts in the NO reduction reaction.

Figure 2 presents data from the temperature programmed reaction (TPR) experiments with (NO+CO) gaseous mixture, performed both with the SA_550 and the SLA_550 catalysts. These catalysts have close surface area values and similar XRD patterns. The catalysts were initially treated for 1h at 200°C with the same NO+CO+Ar reaction gas mixture, which has been used for the catalytic activity tests (Fig. 1). Thereafter the catalysts were cooled down to room temperature in an Ar flow and adsorption of NO+CO+Ar gas mixture was carried out at the same temperature for 30 min.

As it is seen in the TPR patterns (Fig. 2) CO, CO_2 and NO are being simultaneously desorbed within a narrow temperature region 50-90°C with both types of catalysts. The TD profiles and the TD_{max}≅60°C for CO desorption from both catalysts is similarly quite close. However, the integrated surface area of the CO TD peak in the case of La-modified sample, SLA_550, is twice as large as that measured with the non-modified catalyst SA_550. The TD pattern of CO_2 for the SLA_550 catalyst has a wide peak with TD_{max} ≅ 125°C, which is not present in the pattern of the SA_550 sample. The TD profile for NO desorption in the case of SLA_550 catalyst is slightly widened towards the lower temperatures. Therefore, on the basis of the (NO+CO)-TPR data it can be concluded that the main difference between the SA_550 and SLA_550 catalysts, is the increased amount of desorbed gases from the latter catalyst. This means that the La-

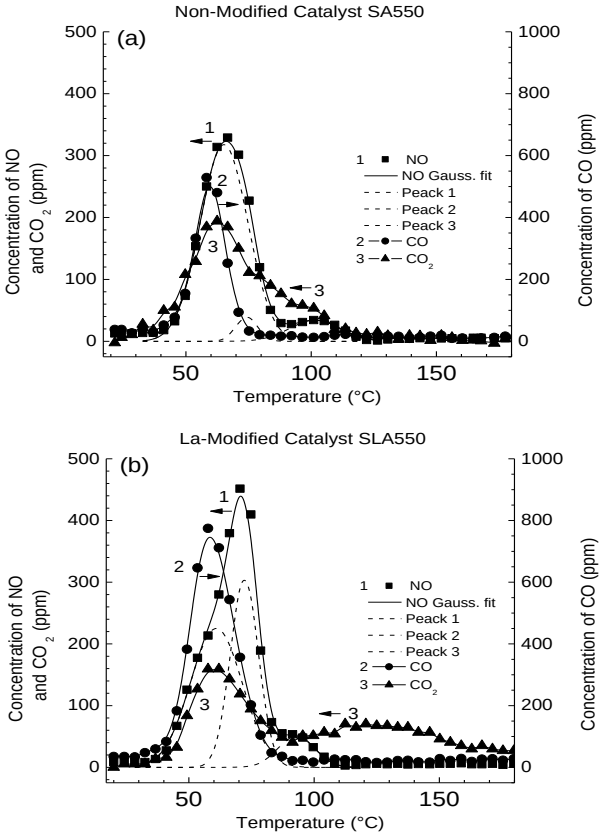

Figure 2. TD patterns of NO, CO and CO_2 obtained after initial adsorption of a NO+CO+Ar gas mixture at 25°C.

modified catalyst has an increased number of active sites for adsorption of NO, CO and CO_2. Both reactants, namely NO and CO, should be adsorbed on the surface of the catalyst for the reaction to occur. As it was discussed above, La ensures Co:Cu ratios for the supported active CuCo-spinel, which are close to that in the stoichiometric $CuCo_2O_4$ spinel. The presence of bivalent catalytically active sites playing the role of donor-acceptor pairs is a well-established requirement for the activity of oxide catalysts in different redox reactions [6, 16].

The results obtained for the oxidation of CO by molecular O_2 are presented in Fig. 3. The reaction conditions were as follows: 0.5 vol. % CO, 1 vol.% O_2, balance Ar and GHSV 20 000 h^{-1}. Comparison of T_{50} measured with non-modified

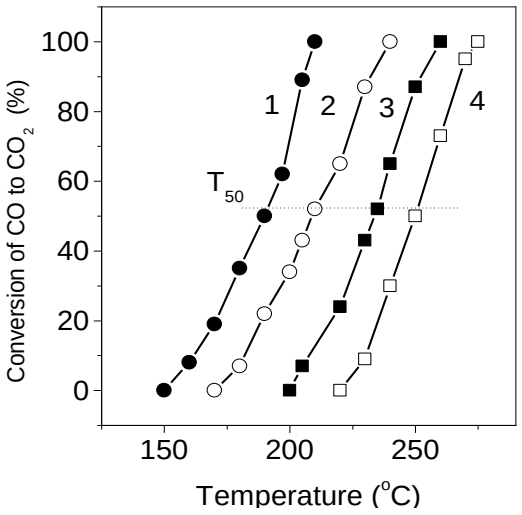

Fig. 3. Comparison of the activity of non-modified and La-modified Cu-Co oxide catalysts in the reaction of catalytic oxidation of CO by O_2. 1–SLA_550, 2–SA_550, 3– SLA_1050, 4–SA_1050.

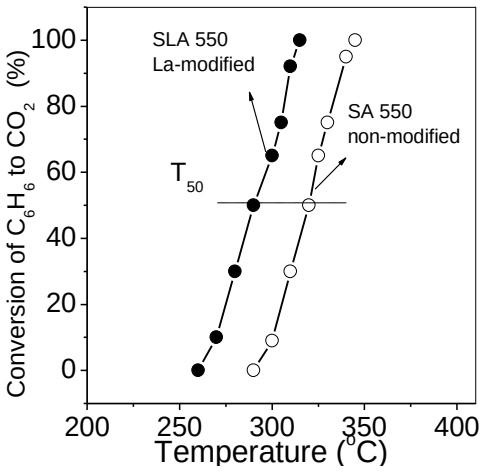

Fig. 4. Comparison of the activity of non-modified and La-modified Cu-Co oxide catalysts in the reaction of complete oxidation of C_6H_6 by O_2.

and La-modified catalysts clearly indicates the beneficial role of La modification for thermal stabilization of the catalytic activity with respect to CO oxidation. A thermal treatment at 1050^0C strongly hinders the $CO+O_2$ reaction on non-modified SA_550 catalyst causing a 50°C shift in T_{50} towards the higher temperature. In the case of La-modified catalyst SLA_550, thermal ageing at 1050°C leads to a T_{50} shift of only 20°C to the higher temperatures. Modification with La improves the catalytic performance of Cu-Co catalysts in the reaction of complete oxidation of C_6H_6 with molecular O_2 as well. The reaction conditions were: 0.04 vol. % C_6H_6, 1 vol. % O_2, ballast Ar and GHSV 20 000 h^{-1}. The promoting effect of La concerns both the activity and the thermal stability of catalysts, as it is seen in Figure 4. The temperature for 50 % conversion of NO in the case of La-modified catalyst SLA_550 is with 30°C lower than T_{50} measured for the unmodified catalyst SA_550. The role of La-modification of Cu-Co oxide catalysts is to prevent the interaction of the active Cu-Co oxide phase with the alumina support to form aluminates, and as a result of this to preserve the surface area and the number of catalytically active sites. The results of this paper show that the simultaneous presence of Cu, Co and La on the catalyst surface has a synergistic effect with respect to the thermal durability of the Cu-Co oxide catalysts supported on alumina and a positive effect on the NO+CO, $CO+O_2$ and $C_6H_6+O_2$ reactions.

4. CONCLUSIONS

The modification of γ-Al_2O_3 support with La at a loading below 3 wt. % has a positive effect on the catalytic performance of supported Cu-Co oxide catalysts. Lanthanum plays a stabilizing role for the specific surface area of carriers and Cu-Co oxide catalysts; the addition of La suppresses the $\gamma \rightarrow \alpha$ transformation of the alumina support and its interaction with the active Cu-Co oxide phase to produce aluminates. Modification of the support with La prevents the dissolution of Cu ions into the γ-Al_2O_3 during the impregnation with Cu-Co nitrates. Thus, the active Cu-Co oxide spinel phase supported on La/Al_2O_3 has a higher Co:Cu ratio, which is close to that in the stoichiometric $CuCo_2O_4$ spinel. The La-modified catalysts have higher activity towards the NO+CO, $CO+O_2$ and $C_6H_6+O_2$ reactions, compared to non-modified catalysts. Incorporation of La into the support does not change the energetic status of catalytic active sites but rather increases the number of these sites.

Acknowledgements: *The authors thank the National Science Fund of Bulgaria (Grants DTK 02-64/2009) for the financial support.*

REFERENCES

1. M. Sheleff, K. Otto, H. Gandhi, *J. Catal*., **12**, 361(1968)**.**
2. X. Jiang, R. Zhou, P. Pan, B. Zhu, X. Yuan, X. Zheng, *Appl. Catal. A*, **150**, 131 (1997).
3. L. Xiancai, H. Quanhong, Y. Yifeng, CH. Juanrong, L. Zhihua, *J. Rare Earths*, **26**, 864 (2008).
4. M. Ferrandon, E. Björnbom, *J. Catal*., **200**, 148 (2001).
5. Y.-Z. Chena, B.-J. Liawb, W.-H. Lai, *Appl. Catal. A*, **230**, 73 (2002).
6. M. Ferrandon, B. Ferrand, E. Björnbom, F. Klingstedt, A.K. Neyestanaki, H. Karhu, I. J. Väyrynenz, *J. Catal*., **202**, 354 (2001).
7. A. Barrera, M. Viniegra, P. Bosch, V.H. Lara, S. Fuentes, *Appl. Catal. B*, **34**, 97 (2001).
8. A. Barrera, M. Viniegra, S. Fuentes, G. Dı´az, *Appl. Catal. B*, **56**, 279 (2005).
9. Y Xiang, L. Kong, Ch. Lu, L. Ma, X. Li, *Reac. Kinet. Mech. Cat.*, **100**, 227 (2010).
10. D. Panayotov, M. Khristova, D. Mehandjiev, *Appl. Catal.*, **34**, 49 (1987).
11. D. Panayotov, M. Khristova, D. Mehandjiev, *J. Catal*. **156**, 219 (1995).
12. D. Panayotov, M. Khristova, M. Velikova, *Appl. Catal.* B **9** 107 (1996).
13. D. Mehandjiev, P. Dimitrova, *React. Kinet. Catal. Lett*., **56**, 341 (1995).
14. S.-J. Huang, A.B. Walters, M.A. Vannice, *Appl. Catal. B*, **26,** 101 (2000).
15. M. Bettman, R.E. Chase, K. Otto, W.H. Weber, *J. Catal.*, **117**, 447 (1989).
16. N. R.E. Radwan, *Appl. Catal. A*, **257**, 177 (2004).

ВЛИЯНИЕТО НА La ВЪРХУ АКТИВНОСТТА И ТЕРМИЧНАТА СТАБИЛНОСТ НА CU-CO ОКСИДНИ КАТАЛИЗАТОРИ НАНЕСЕНИ ВЪРХУ НОСИТЕЛ ОТ ДВУАЛУМИНИЕВ ТРИОКСИД

Д. Д. Стоянова, Г. М. Иванов, М. С. Христова

Институт по обща и неорганична химия, Българска академия на науките, ул.»Акад. Г. Бончев» бл. 11, 1113 София, България

Постъпила на 29 ноември, 2010 г.; одобрена на 4 март, 2011 г.

(Резюме)

В работата са представени Cu-Co оксидни катализатори върху модифициран с La алуминиев носител. Образците са получени по метода на импрегниране от водни разтвори на нитрати съдържащи Cu и Co на носители (γ-Al_2O_3 и модифициран с La Al_2O_3). Образците са охарактеризирани чрез ICP анализ, рентгенофазово и по метода на БЕТ. Реакциите на редукция на NO с CO и окислението на CO и C_6H_6 с O_2 са осъществени върху модифицирани и немодифицирани с La катализатори. Модифицирането на γ-Al_2O_3 с La под 3тегл.% има позитивен ефект върху каталитичните отнасяния на нанесените Cu-Co оксидни катализатори, като добавянето на La потиска образуването на α-Al_2O_3, както и възпрепятства взаимодействието на активната Cu-Co оксидна фаза с носителя и образуването на алуминати. Модифицирането на носителя с La предотвратява внедряването на Cu йони в γ-Al_2O_3 по време на импрегнирането с Cu-Co нитрати. Така активния Cu-Co оксиден шпинел, нанесен върху La/Al_2O_3 има съотношение Co:Cu, което е близо до това на стехиометричния $CuCo_2O_4$ шпинел. Модифицираните с La катализатори притежават висока активност по отношение на NO+CO, CO+O_2 и C_6H_6+O_2 реакциите, в сравнение с немодифицираните катализатори. Вграждането на La в носителя не променя енергетичната природа на каталитично - активните центрове, а по-скоро увеличава броя на тези центрове.

Bulgarian Chemical Communications, Volume 43, Number 4 (pp 483 – 488) 2011

Effect of activated carbons derived from agricultural by-products on the hydrogen storage properties of magnesium

E. Grigorova[a*], Ts. Mandzhukova[a], M. Khristov[a], P. Tzvetkov[a], B. Tsyntsarski[b]

[a] *Institute of General and Inorganic Chemistry, Bulgarian Academy of Sciences, bl.11, Acad. G. Bonchev str. 1113 Sofia, Bulgaria*

[b] *Institute of Organic Chemistry, Bulgarian Academy of Sciences, bl.9, Acad. G. Bonchev str., 1113 Sofia, Bulgaria*

Received February 15, 2011; Accepted April 4, 2011

The absorption-desorption characteristics towards hydrogen of the composites 95wt.% Mg-5wt.% activated carbons derived from bean pods and apricot stones, obtained by ball milling in argon atmosphere were investigated. Hydriding of the composites was performed at temperatures 573 K and 473 K and pressure of 1 MPa and dehydriding - at T = 623 K and P = 0.15 MPa. Absorption capacity values of 5.43 wt.% and 6.13 wt.% (at T = 573 K and P = 1 MPa) were reached for the composites containing activated carbons derived from bean pods and from apricot stones, respectively. The hydriding/dehydriding characteristics of the studied composites were compared with those of pure magnesium. It was established that the activated carbons derived from bean pods and apricot stones improved the hydrogen sorption kinetics of magnesium.

Keywords: hydrogen storage materials; metal hydrides; mechanochemical processing; gas-solid reactions.

INTRODUCTION

Magnesium is considered as a promising material for hydrogen storage due to its high theoretical absorption capacity of 7.6 wt%, volumetric density, availability and low cost. The limitation of its practical application is due to two main reasons: i) sluggish hydriding/dehydriding kinetics and ii) high temperatures of hydrogen absorption and desorption. The mechanochemical treatment, along with the use of an appropriate additive, could resolve these drawbacks. Mechanical grinding in high-energy ball mills consists of repetitive cold welding and fracturing. Its application for the preparation of hydrogen storage materials leads to an increase in the specific surface area and appearance of different defects, which modify the hydriding kinetics of the composites. Several types of additives to magnesium based materials were used, such as: 3d metals [1,2], metal oxides [3-7], intermetallic [8,9] and carbon containing compounds as: graphite [10-15,17,18,20-22,24], multi and single-walled carbon nanotubes [16-19, 24], carbon black [17,18, 23], nanodiamonds [23], amorphous carbon soot [23] and carbon nano-fibers [24]. Depending of the nature of the additive the mechanism of its catalytic effect is different.

Some aspects of the role of carbon containing additives on the hydrogen sorption properties of magnesium are not clarified in the literature. This was discussed and well illustrated by V. Fuster *et al.* [20]. Many authors agreed that carbon containing additives improved the hydrogen sorption properties of magnesium. Some of them have proved that graphite protects magnesium from oxidation and acts as a process controlling agent during ball milling due to its lubricant properties. There are some controversial opinions about the catalytic role of graphite on hydrogen sorption properties. As a conclusion it should be mentioned that the effect of carbon containing additives to magnesium is complex and not yet sufficiently clarified.

Activated carbons are often synthesized from precursors based on expensive and depleting fossil fuels. They can also be prepared from biomass or agricultural by-products with lower price.

The subject of the present work was to investigate the effect of activated carbons prepared from plant precursors as bean pods and apricot stones on the hydrogen sorption properties of magnesium. The hydriding/dehydriding characteristics of the studied composites were compared with those of pure magnesium.

EXPERIMENTAL

Activated carbons were prepared by steam pyrolysis from apricot stones and bean pods. The raw material was heated up to the carbonization

*To whom all correspondence should be sent: E-mail: egeorg@svr.igic.bas.bg

temperature (873 K) and the solid product was activated with water vapour for 60 min at 1073 K for bean pods and 973 K for apricot stones. Details on the preparation procedure of activated carbons can be found in [25-28].

The mixtures of 95 wt% powdery Mg with 99.9% purity and 5 wt% activated carbons derived from bean pods (BP) and apricot stones (AS) were ball milled in the planetary monomill Fritsch Pulverisette 6 for 30 min and 180 min under argon with rotation speed 200 rpm and 1:10 sample-to-balls weight ratio. Only the composite with 5 wt% BP was subjected to prolonged ball milling. Further in the text, these composites will be denoted as follows: Mg-BP-30: 95 wt% Mg-5 wt% activated carbon derived from bean pods after 30 min ball milling; Mg-BP-180: 95 wt% Mg-5 wt% activated carbon derived from bean pods after 180 min ball milling and Mg-AS: 95 wt% Mg-5 wt% activated carbon derived from apricot stones ball milled for 30 min. The purity of the argon and hydrogen gases used was 99.998% and 99.999%, respectively.

All composites were characterized by X- ray diffraction analyses on a Bruker D8 Advance diffractometer using CuKα radiation and by scanning electron microscopy on a Philips 515 electron microscope. The hydrogen absorption/desorption measurements were performed on a Sivert type apparatus. Particle size measurements of the ball milled samples were performed in distilled water using the Fritsch Analysette 22 Compact device with ultrasonic equipment. Textural characterization of the activated carbons was carried out by measuring the nitrogen adsorption isotherms in an automatic apparatus (Tristar 3000, Micromeritics).

RESULTS AND DISCUSSION

The X-ray diffraction patterns of the activated carbons are presented in Fig.1. The broad diffuse peaks at 24 and 43 degrees 2θ can be indexed as *002* and *100* lines in the graphite structure. Minor quantities of inorganic compounds like $CaCO_3$ and MgO were detected, notably in the activated carbon derived from bean pods. The higher and narrower peak at 24 2θ (*002*) for the activated carbon from AS in comparison with the activated carbon from BP points to the higher degree of graphitization and the more ordered structure of the former.

The X-ray diffraction patterns of the composites Mg-BP-30, Mg-BP-180 and Mg-AS, obtained after ball milling under argon, showed no substantial difference (Fig.2). The main phase is magnesium with traces of $Mg(OH)_2$. One of the composites (Mg-BP) was subjected to prolonged ball milling under argon. Due to the decrease in the crystallite

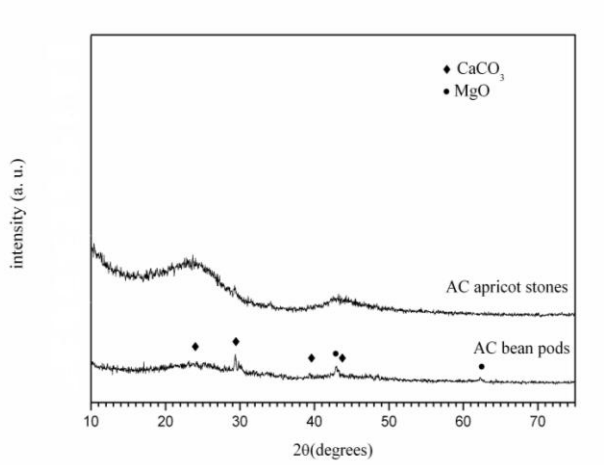

Fig. 1 X-ray diffraction patterns of activated carbon derived from: a) bean pods and b) apricot stones

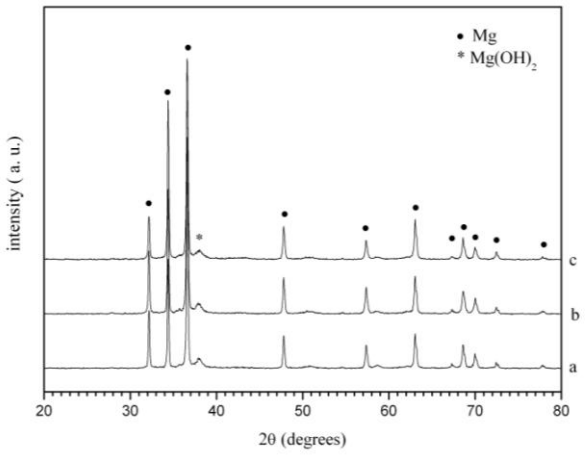

Fig.2 X-ray diffraction patterns of the composites obtained after ball milling under argon a) Mg-AS); b) Mg-BP-30min and c) Mg-BP-180 min.

size and the accumulation of lattice stresses and defects, broadening of the Mg diffraction peaks after prolonger ball milling could be expected. Even after ball milling of the composite Mg-BP for 180 min, the diffraction peaks have the same shape, position and intensity as for the composite ball milled for 30 min. After hydriding at T= 573 K and P= 1 MPa, the X-ray diffraction patterns of the composites showed main phase of MgH_2, small amount of unreacted magnesium and presence of MgO (Fig.3).

The kinetic curves obtained at temperatures 623 K for the first cycle and 573 K for the fifth cycle and pressure of 1 MPa are given in Fig 4. The effect of ball milling duration on the hydrogen sorption properties of the composite Mg-BP was investigated. The sample ball milled for 180 min

showed easier activation than that, ball milled for only 30 min. Nevertheless, after few cycles of hydriding/dehydriding, no substantial difference in

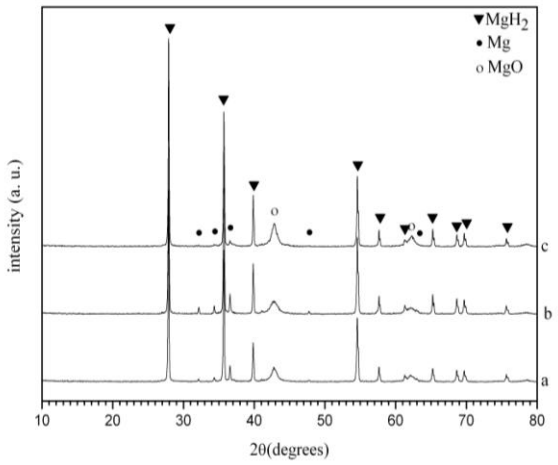

Fig. 3. X-ray diffraction patterns of the composites obtained after hydriding at T= 573 K and P= 1 MPa a) Mg-AS; b) Mg-BP-30min and c) Mg-BP-180 min.

the hydriding curves was observed. The two composites reached about 5.4 wt.% hydrogen storage capacity after 60 min hydriding at temperature 573 K and a pressure of 1MPa. The samples Mg-BP-30 and Mg-BP-180 displayed better absorption kinetics and reached higher hydrogen absorption capacity than pure magnesium at the same conditions.

The effect of activated carbons as additives on the hydriding properties of magnesium at 573 K and 1 MPa is illustrated in Fig.5. The specific surface area may be considered as an important characteristic which has a positive effect on the hydrogen sorption properties of Mg. The specific surface area of activated carbon derived from bean pods is about three times lower (280 m^2/g) than that of activated carbon derived from apricot stones (960 m^2/g). Improved kinetics was observed for the composite containing activated carbon with higher specific surface area. With advance of hydriding process the rate of reaction for Mg-BP-30 and Mg-BP-180 decreased in comparison with the Mg-AS sample. The composites reached maximum hydriding capacity of 5.43 wt% for Mg-BP-30; 5.35 wt% for Mg-BP-180 and 6.13 wt% for Mg-AS. At T = 473 K the kinetics of the hydriding reaction for all samples decreased and the hydrogen absorption capacity values after 60 min of hydriding were close to 1 wt%.

The composite Mg-AS desorbs 50% of the absorbed hydrogen within 17 min (Fig.6). The desorption curves of Mg-BP-180 and Mg-AS are quite similar up to 20 min. The worst hydrogen desorption properties manifests pure magnesium followed by Mg-BP-30. When the processes of

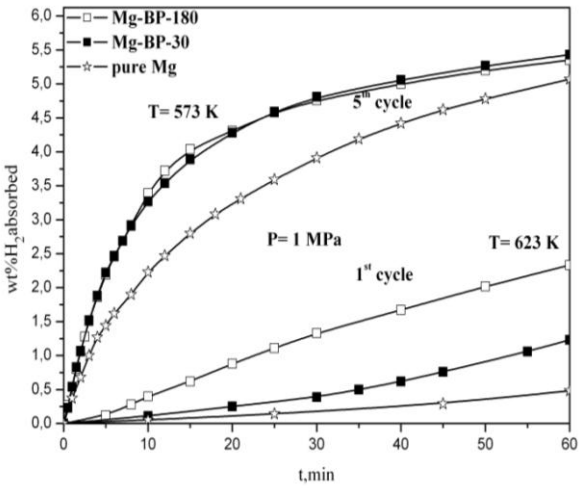

Fig. 4 Kinetic curves at the first and fifth cycles of hydriding of the composites Mg- BP ball milled 30 min or 180 min and pure magnesium.

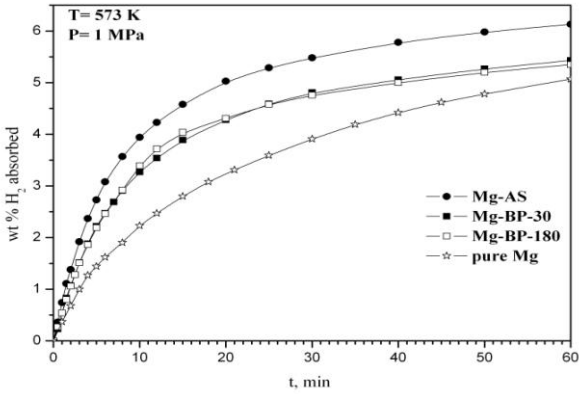

Fig. 5 Kinetic curves of hydriding of the composites Mg-BP-30, Mg-BP-180, Mg-AS and pure magnesium.

hydrogen dissociation and recombination during desorption are faster, the hydrogen molecules should diffuse through the growing metal layer and the rate controlling step should change earlier. The growing metal layer during desorption plays the role of a diffusion barrier. The desorption curves of the composite ball milled for a longer time indicate a slightly faster rate of the reaction at the beginning of the process and a lower hydrogen absorption capacity, which could explain the earlier tendency of saturation.

As it is evident from Figs. 4, 5 and 6, the addition of activated carbons derived from apricot stones more favourably affects the hydrogen sorption characteristics than activated carbon from bean pods. It should be noted that compared to pure magnesium, the composites under consideration have better absorption/desorption characteristics.

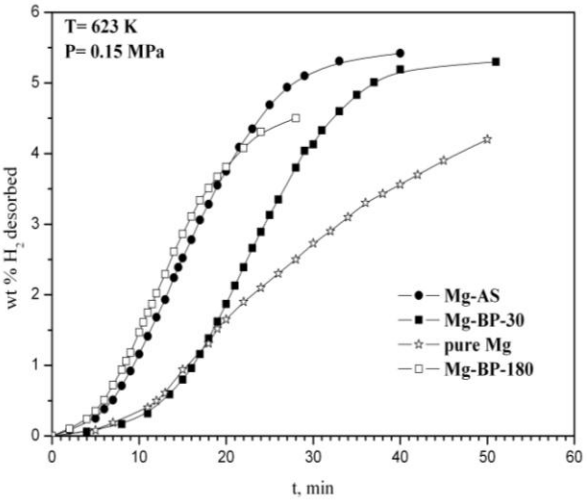

Fig. 6 Kinetic curves of dehydriding of the composites Mg-BP-30, Mg-BP-180, Mg-AS and pure magnesium.

Both the destruction of the MgO layer covering magnesium and the presence of more defects and active sites help and accelerate hydrogen dissociative chemisorption and nucleation. The activated carbon derived from apricot stones has a more favourable effect on the hydriding kinetics of magnesium probably because of the more effective destruction of the MgO layer and the prevention of its restoration, hindering oxygen back diffusion (Fig.4).

It should be noted that the activated carbons were prepared from various precursors and they differed not only by specific surface area. It was shown in the literature that the electrochemical hydrogen storage is favoured in carbon materials with a well developed porosity and a low content of surface oxygen complexes [29]. The ash content was 22.8 % for activated carbon derived from bean pods and 2.0 % for activated carbon derived from apricot stones. The functional groups on the surface of the activated carbons have a strong effect on the adsorption properties. The surface of both activated carbons is of basic nature. The amount of acidic groups determined by Boehm's method, was higher for AC derived from apricot stones than that for AC derived from bean pods [25- 28]. According to Su *et al.* [30], the adsorption capacity of activated carbon for non-polar molecules such as hydrogen, increased with the increase in the amount of surface acidic groups. Moreover, Gergova *et al.* [25] established that higher amount of chemical groups containing oxygen (or another heteroatom) on the surface of activated carbons derived from apricot stones and other agricultural by-products provided higher concentrations of active sites. The micropore volume of the activated carbon derived from apricot stones (AS) is higher than that of the activated carbon derived from bean pods (BP). AS has the highest microporosity and total pore volume. The relatively high microporosity of the carbon from apricot stones may be partly attributed to the higher cellulose content of this precursor. On the other hand, the activated carbon derived from bean pods is characterized by meso- and macroporous structure [27, 28].

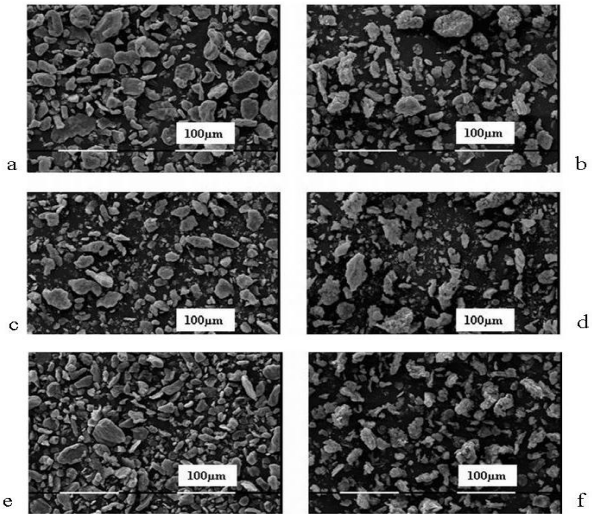

Fig. 7 SEM microphotographs of the composites: a) Mg-BP-30; b) Mg-BP-30 hydrided at 573K; c) Mg-BP-180; d) Mg-BP-180 hydrided at 573 K; e) Mg-AS after ball milling and f) Mg- AS hydrided at 573K

In Fig. 7 scanning electron microscopy images are presented for the composites after ball milling and hydriding. For all samples the size of the larger particles is from 20 to maximum 50 μm and for the smaller particles - a few μm. More small particles are visible in the sample ball milled 180 min with activated carbon derived from bean pods. After hydriding, the particles of the two samples with activated carbon derived from bean pods displayed similar size and shape. After hydriding of the composites, the surface was not so flat and some roughness and cracks are visible.

In Table 1 the particle size distribution of the ball milled composites is given. For all composites the median diameter $d_{0.5}$ is almost the same. Only for the composite Mg-AC-180 a lower $d_{0.1}$ value was registered. The span ($d_{0.9}$-$d_{0.1}$/$d_{0.5}$) for this sample slightly increases compared to the other

composites ball milled for 30 min which have the same particle size distribution. These results are in good agreement with the scanning electron microscopy images showed in Fig. 6. The $d_{0.9}$ value for all composites is about 50 μm. The increase in the duration of ball milling of Mg-BP lead to some diminution of the particle size and probably to better reduction of the oxide layer on the surface. These facts could explain the easier activation during the hydriding process and the better hydrogen desorption properties of the sample ball milled for 180 min. Despite their close particle size values, the composites ball milled for 30 min displayed different hydrogen sorption properties. These observations confirmed the assumption that the carbon containing additives to magnesium not only acted as process controlling agents to diminish cold welding during ball milling, but their effect appears to be much more complex.

Table 1. Particles size distribution, measured in water. The $d_{0.1}$ and $d_{0.9}$ is the maximal diameter of 10 and 90% of the particles. The $d_{0.5}$ is the median diameter.

Sample	$d_{0.1}$ (μm)	$d_{0.5}$ (μm)	$d_{0.9}$ (μm)	span $d_{0.9}$-$d_{0.1}$/$d_{0.5}$
Mg-BP-30	8.5	22.6	52.1	1.9
Mg-BP-180	5.1	20.9	53.8	2.3
Mg-AS	8.6	22.6	49.9	1.8

Mg-BP: 95wt% Mg-5 wt% activated carbon derived from bean pods, ball mill 30 min and 180 min; Mg-AS: 95wt% Mg-5 wt% activated carbon derived from apricot stones.

CONCLUSIONS

The role of new carbon based additives synthesized from agricultural by-products on the hydrogen sorption characteristics of magnesium was studied. The 95wt% Mg-5 wt% activated carbon derived from apricot stones reached the maximum value of hydrogen absorption capacity of 6.13 wt% at 573 K and 1 MPa after 60 min of hydriding. The composite containing activated carbon derived from apricot stones showed a more pronounced positive effect on the hydrogen sorption characteristics of magnesium. Ball milling for 180 min under argon for the composite Mg-BP-180 lead to easier activation, but after few cycles of hydriding/dehydriding, the absorption kinetics of the two samples ball milled for a longer or a shorter time did not show any difference.

The higher specific surface area of the activated carbon additive reflected favourably on the hydrogen sorption kinetics. Some other characteristics of activated carbons, such as surface chemistry and porosity, also affected these processes. It was established that the activated carbons derived from bean pods and apricot stones improved the hydrogen sorption kinetics of magnesium.

Acknowledgement: *The financial support of Bulgarian Ministry of Science and Education, the National Science Fund of Bulgaria under contracts YS No02 -220/2008 and National Centre for New Materials UNION, No DCVP-02/2/2009 is highly appreciated.*

REFERENCES

1. E. Yu. Ivanov, I. G. Konstanchuk, A. A. Stepanov and V. V. Boldyrev, *Dokl. Akad. Nauk SSSR* **286**, 385 (1986).
2. C.X. Shang, M. Bououdina, Y. Song, Z.X. Guo, *Int. J. Hydrogen Energ.* **29**, 73 (2004).
3. M. Khrussanova, M. Terzieva, P. Peshev, *Int. J. Hydrogen Energ.* **15**, 799 (1990).
4. Z. Dehouche, T. Klassen, W. Oelerich, J. Goyette, T.K. Bose, R. Schulz, *J. Alloys Compd.* **347**, 319 (2002).
5. J.-L. Bobet, F.J. Castro, B. Chevalier, *Scr. Mater.* **52**, 33 (2005).
6. F.J. Castro, J.-L. Bobet, *J. Alloys Compd*. **366**, 303 (2004).
7. G. Barkhordarian, T. Klassen, R. Bormann, *Scr. Mater*. **49**, 213 (2003).
8. M. Khrussanova, J.-L. Bobet, M. Terzieva, B. Chevalier, D. Radev, P. Peshev, B. Darriet, *J. Alloys Compd.* **307**, 283 (2000).
9. R. Vijay, R. Sundaresan, M. P. Maiya, S. Srinivasa Murthy, Y. Fu, H.-P. Klein and M. Groll, *J. Alloys Compd.* **384**, 283 (2004).
10. C. X. Shang, Z. X. Guo, *J. Power Sources* **129**, 73 (2004).
11. S. Bouaricha, J.-P. Dodelet, D. Guay, J. Huot, R. Schulz, *J. Mater. Res.* **16**, 2893 (2001).
12. J.-L. Bobet, E. Grigorova, M. Khrussanova, M. Khristov, P. Stefanov, P. Peshev, *J. Alloys Compd.* **366**, 298 (2004).
13. C. Iwakura, H. Inoue, S. G. Zhang, S. Nohara, *J. Alloys Compd.* **293-295**, 653 (1999).
14. S. Bouaricha, J. P. Dodelet, D. Guay, J. Huot, S. Boily, R. Schulz, *J. Alloys Compd.* **307**, 226 (2000).
15. S. S. Ruggeri, L. Roué, G. Liang, J. Huot, R. Schulz, *J. Alloys Compd.* **343**, 170 (2002).
16. F.X. Wang, X.P. Gao, Z.W. Lu, S.H. Ye, J.Q. Qu,F. Wu, H.T. Yuan, D.Y. Song , *J. Alloys Compd.* **370**, 326 (2004).
17. C.Z. Wu, P. Wang, X. Yao, C. Liu, D.M. Chen, G.Q. Lu, H.M. Cheng, *J. Alloys Compd.* **414**, 259 (2006).

18. Z.G. Huang, Z.P. Guo, A. Calka, D. Wexler, H. K. Liu, *J. Alloys Compd.* **427**, 94 (2007).
19. C. S. Goh, J. Wei, L. C. Lee, M. Gupta, *Compos. Sci. Technol.* **68**, 1432 (2008).
20. V. Fuster, G. Urretavizcaya, F.J. Castro, *J. Alloys Compd.* **481**, 673 (2009).
21. C. Milanese, A. Girella, S. Garroni, G. Bruni, V. Berbenni, P. Matteazzi, A. Marini, *Int. J. Hydrogen Energ.* **35**, 9027 (2010).
22. E. Grigorova, M. Khristov, M. Khrussanova, *Cent. Eur. J. Chem.* **8**, 737 (2010) DOI: 10.2478/s11532-010-0040-0.
23. Tony Spassov, Zlatina Zlatanova, Maya Spassova, Stanislava Todorova, *Int. J. Hydrogen Energ.* **35**, 10396 (2010).
24. M.A. Lillo-Ródenas, Z.X. Guo, K.F. Aguey-Zinsou, D. Cazorla-Amorós, *Carbon* **46**, 126 (2008).
25. K. Gergova, N. Petrov and S. Eser, *Carbon* **32**, 693 (1994).
26. B. Cabal, T. Budinova, C. O. Ania, B. Tsyntsarski, J. B. Parra, B. Petrova, *J. Hazard. Mater.* **161**, 1150 (2009).
27. B. Petrova, T. Budinova, B.Tsyntsarski, N. Petrov, G. Bardarska, C. Ania, J. Parra, *Bulg. Chem. Commun.* **42**, 141 (2010).
28. N. Petrov, T. Budinova, B. Tsyntsarski, B. Petrova, D. Teodosiev, N. Boncheva, *Bulg. Chem. Commun.* **42**, 19 (2010).
29. M.J. Bleda-Martinez, J.M. Pérez, A. Linares-Solano, E. Morallón, D. Cazorla-Amorós, *Carbon* **46**, 1053 (2008).
30. W. Su, Y. Zhou, L. Wei, Y. Sun, L. Zhou, *New carbon mater.* **22**, 135 (2007).
31. A. Nithya, S. Rajendran, *Bulg. Chem. Commun.*, **42** 119 (2010).

ВЛИЯНИЕ НА ДОБАВКАТА ОТ АКТИВНИ ВЪГЛЕНИ ПОЛУЧЕНИ ОТ СЕЛСКОСТОПАНСКИ ПРОДУКТИ ВЪРХУ СВОЙСТВАТА НА МАГНЕЗИЙ ЗА СЪХРАНЕНИЕ НА ВОДОРОД

Е. Григорова[а]*, Цв. Манджукова[а], М. Христов[а], Петър Цветков[а] и Бойко Цинцарски[б]

[а] Институт по обща и неорганична химия, Българска академия на науките, ул. Акад. Г. Бончев, блок 11, София 1113
[б] Институт по органична химия с център по фитохимия, Българска академия на науките, ул. Акад. Г. Бончев, блок 9, София 1113

Постъпила на 15 февруари, 2011 г. ; приета на 4 април, 2011 г.

(Резюме)

Изследвани са абсорбционно- десорбционните характеристики по отношение на водород на композитите 95 мас.% Mg- 5 мас.% активен въглен, синтезиран от кайсиеви костилки или бобени шушулки, получени чрез механоактивиране под аргон. Процесът на хидриране е извършен при температура 573 K и 473 K и налягане 1 MPa, а на дехидриране - при T = 623 K и P = 0.15 MPa. Достигнатите стойности на абсорбционния капацитет са 5.43 мас.% за композита, съдържащ активен въглен от бобови шушулки и 6.13 мас.% за композита, съдържащ активен въглен от кайсиеви костилки (при T = 573 K и P = 1 MPa). Характеристиките на хидриране/дехидриране на изследваните композити са сравнени с тези на чистия магнезий. Установено е, че активните въглени, получени от бобови шушулки и кайсиеви костилки, подобряват сорбционните характеристики на магнезия по отношение на водорода

Bulgarian Chemical Communications, Volume 43, Number 4, (pp. 489 - 501) 2011

Lanthanide oxide doped titania photocatalysts for degradation of organic pollutants under UV and visible light illumination

D. Tz. Dimitrov*, M. M. Milanova, R. P. Kralshevska

Department of General and Inorganic Chemistry, Faculty of Chemistry, University of Sofia, 1, J. Bourchier Blvd., Sofia 1164, Bulgaria

Received November 2, 2010; Revised January 5, 2011

The main goal of this short review is to present the most valuable attempts that have been made in the past decades to shift the absorption of TiO_2 from UV- to the visible-light region by lanthanide doping. In order to understand the other factors by which doping of TiO_2 with lanthanides can increase the photocatalytic activity under solar irradiation, the first short chapter is devoted to the physical mechanisms responsible for the degradation of organic pollutants by lanthanide oxide doped titania under UV-light exposure. This aspect has been studied for a long time and is better understood. The second chapter deals with the same features, but extended for the visible-light exposure of catalysts. The most typical observations for bathochromic shift, effect of co-doping and organic dye sensitizing on the photocatalytic activity of lanthanide oxide doped titania are considered in detail.

Key words: photocatalysts, titania, lanthanides-doped titania, visible light.

INTRODUCTION

The heterogeneous photocatalysis based on oxide semiconductors is a promising technology for remedying environmental pollution and solving energy depletion and has become one of the most active research fields in recent years. So far, researchers have developed many materials that have the potential to act as photocatalysts for a wide range of applications including TiO_2, WO_3, $SrTiO_3$, α-Fe_2O_3, ZnO and $NaBiO_3$. Among them, TiO_2 has proven to be a benchmark catalyst for detoxification of organic pollutants [1-4]. The photoexcitation of a semiconductor leads to the formation of an electron-hole pair. The excited-state conduction band electrons can: recombine with the holes and dissipate the input energy; get trapped in surface states; react with electron donors and electron acceptors adsorbed on the semiconductor surface [5].

In particular, because of their unique 4*f*-electronic configuration and spectral characteristics, lanthanides are ideal dopants for modifying the crystal structure, electronic structure, optical properties and surface adsorption of TiO_2 and forming a series of novel promising photocatalysts. On the other hand, as a group of elements that both resemble each other and show particular differences between them, lanthanides provide an opportunity for an in-depth study of the electronic structure that can influence the performance of TiO_2 photocatalysts [6]. However, as a wide band gap oxide semiconductor (E_g = 3.23 eV), anatase TiO_2 shows a photocatalytic activity only under UV-light irradiation (λ < 384 nm), which accounts for only a small fraction of the solar energy (~5%). The sun is an abundant source of photons, where visible light accounts for a large fraction of spectrum (~45%) [7]. Therefore, how to effectively utilize sunlight is the most challenging subject for extensive application of TiO_2. The main goal of the present article is to consider the most important attempts that have been made in past decades to shift the TiO_2 absorption from the UV region to the visible-light region. In order to understand all factors that can increase the photocatalytic activity under solar irradiation, the first short part of this review is devoted to the physical mechanisms responsible for the degradation of organic pollutants by lanthanide oxide doped titania under UV-light exposure.

1. PHYSICAL MECHANISMS RESPONSIBLE FOR THE DEGRADATION OF ORGANIC POLLUTANTS BY LANTHANIDE OXIDE DOPED TITANIA UNDER UV-LIGHT EXPOSURE

1.1 Enhancing of the photocatalytic activity of TiO_2 powder by suppressing electron-hole

* To whom all correspondence should be sent:
E-mail: DTsenov@wmail.chem.uni-sofia.bg

recombination with trapping of photogenerated electrons at the interface

Li *et al.* [8] have studied the effect of electrons, shallowly trapped by Gd^{3+} in nanocrystalline $La_{1.5}Gd_{0.5}Ti_2O_7$ solid solution and in Gd^{3+}-doped TiO_2, on the photocatalytic activity in the liquid phase. They claim that the half-filled ***f***–shells of Gd^{3+} ions play a mechanistic role because it is more stable and when such a configuration is destroyed, it has a strong tendency to return to the original stable state. This particular characteristic of a dopant ion with a half-filled electronic configuration can promote the charge transfer and efficiently separate the electron–hole pairs by shallowly trapping electrons. Even though other metal ions can also trap the photo-excited electrons, the detrapping is more difficult on these ions.

Rengaraj *et al.* [9] have discovered the synergetic effect of neodymium ions deposited on the TiO_2 surface, which behave as sites where electrons and sacrificial electron donors such as formic acid accumulate. The transfer of photo-induced electrons from the TiO_2 conduction band to the metallic Nd particles at the interface is thermodynamically possible because the Fermi level of TiO_2 is higher than that of Nd metal [10].The proposed mechanism of the effect of both Nd particles and formic acid added as a hole scavenger is shown in Fig. 1.

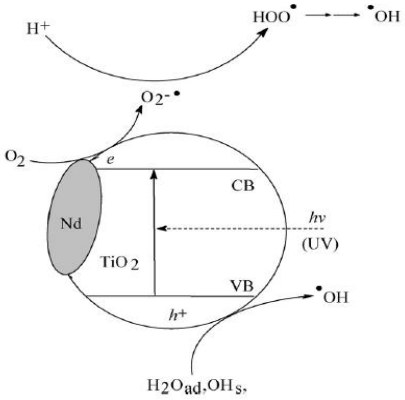

Fig. 1. Mechanism of the photocatalytic reaction on a Nd–TiO_2 catalyst under UV [9].

The metallic Nd particles at the interface will act as electron traps, enhancing the electron–hole separation and the subsequent transfer of trapped electrons to the adsorbed O_2 or Cr(VI) acting as an electron acceptor. This can be explained by the surface electronic effect induced by neodymium. This reaction enables the positive photoholes p^+ to react with adsorbed OH^- species in order to create $^\bullet$OH radical, as shown in the sequence of Eqs. (1-3):

$$(TiO_2) + h\nu \rightarrow e^- + p^+ \quad (1)$$

$$Nd + e^- \rightarrow e_{Nd}^- \quad (2)$$

$$OH^- + p^+ \rightarrow {}^\bullet OH \quad (3)$$

The $^\bullet$OH species formed from the holes will be accepted by HCOOH specially added for that purpose (Eq. (4)):

$$^\bullet OH + HCOOH \rightarrow \text{intermediates} \rightarrow CO_2 + H_2O \quad (4)$$

By this way HCOOH suppresses the electron–hole recombination process and increases the reduction efficiency. In the presence of formic acid, the Cr(VI) reduction reaction can be described as follows:

$$Cr_2O_7^{2-} + 14H^+ + 6e^- \rightarrow 2\,Cr^{3+} + 7H_2O \quad (5)$$

In this reaction, 1 mol of Cr(VI) requires 3 mol of electrons to be reduced to Cr(III), which needs an equivalent of 3 mol of HCOOH to scavenge the holes. The enhanced reduction of oxygen through better electron-hole separation in Nd–TiO_2 particles compared to pure TiO_2 increases the rate of HCOOH degradation while simultaneously increasing the rate of reduction of Cr(VI).

Yang *et al.* [11] have studied the photocatalytic activity of CeO_2/TiO_2 mixed oxide nanoparticles. They claim that the Ce^{4+}/Ce^{3+} redox couple increases the separation of electron-hole pairs. Doped cerium only may be present as the so-called second phase on the surface of TiO_2. CeO_2 can trap photo-generated electrons at the interface while reducing to Ce^{3+} according to the reaction (6):

$$e^- + Ce^{4+} \rightarrow Ce^{3+} \quad (6)$$

In this case, the role of Ce^{4+} is the removal of electrons from electron–hole recombination sites with simultaneous production of oxidizable species.

Mele *et al.* [12] have used lanthanide diphthalocyanine sensitizers on a polycrystalline anatase TiO_2 surface. These sensitizers work because of the positions of conduction and valence band energy levels of anatase TiO_2 relative to the redox potentials of the sensitizers allow charge transfer by injection of an electron from the excited sensitizers to the conduction band of TiO_2 and from the conduction band of TiO_2 to the sensitizers.

Jiang *et al.* [13] have studied TiO_2 composite nanoparticles doped with low amount of Yb^{3+}; the doping increases the number of hydroxyl groups on the TiO_2 surface because Ti^{4+} replaces Yb^{3+} in the

Yb_2O_3 crystal lattice and creates a charge imbalance. In order to restore the charge balance, more hydroxide ions will be adsorbed on the surface, which could enhance the lifetime of electron-hole pairs.

Ökte and Yılmaz [14] have investigated the synergy between ZSM-5, TiO_2 and La_2O_3 of lanthanum loaded TiO_2-ZSM-5 photocatalysts where TiO_2 and La_2O_3 nanoparticles are dispersed on the support surface. The benefit of La^{3+} ion incorporation is due to the capability of these ions to trap electrons, inhibit electron–hole recombination reactions and concentrate pollutant molecules on the catalyst surface. ZSM-5 acts as a hole trap (ZSM is abbreviation for Zeolite Sieve of Molecular porosity). This is possible because the high Si/Al ratio in ZSM-5 presents a limited number of Lewis acid sites in the framework. This property decreases the electron-delocalizing ability, but simultaneously allows capturing of photogenerated holes of TiO_2.

1.2 Enhancing of the photocatalytic activity of TiO_2 powder caused by the different effect of mesoporous walls

Peng *et al.* [15] have suggested that the presence of lanthanum ions in the TiO_2 mesostructure increases the photoactivity due to the larger surface area and more active sites for combining with molecules of the pollutant. The high degree of crystallinity also plays an important role in the photoactivity of TiO_2.

Zhao *et al.* [16] have shown that the absorption edge of TiO_2 shifts to the visible light range and the band-gap narrows, when TiO_2 is doped with Nd^{3+}. The Nd species are distributed in the bulk of nanoparticle instead of concentrating on its surface. Density functional theory calculations are used to interpret the narrowing of the band-gap. The density of states (DOS) profiles of the undoped TiO_2 and Nd^{3+}-doped anatase TiO_2 are shown in Fig. 2. The calculated value of the band-gap for undoped TiO_2 is 3.20 eV, which is in good agreement with the experimental value of 3.22 eV. The band-gap is formed between the O 2***p*** orbitals and Ti 3***d*** orbitals.

The main contribution to the valence band comes from O 2*p* orbitals, while the states at the conduction band are predominantly Ti 3*d* orbitals. A $NdTi_3O_8$ super cell models the Nd^{3+}-doped anatase with Nd atoms in the substitutional sites. The DOS for this structure is shown in Fig. 2 b with a much smaller band-gap value (1.93 eV) calculated. Obviously, the existence of DOS of Nd 4*f* orbitals means that some electronic states are introduced into the band-gap of TiO_2 by Nd 4*f* electron levels located close to the lower edge of conduction band to form new LUMO (lowest unoccupied molecular orbitals). Consequently, the photoexcited electron for Nd-doped material can be transferred from O 2*p* to Nd 4*f* instead of Ti 3*d*, which is different from the situation of undoped TiO_2.

1.3 The effect of co-doping on the photocatalytic activity

Shi *et al.* [17] have found a marked improvement of the photocatalytic activity of TiO_2 by co-doping with Fe^{3+} and Ho^{3+}. Fe^{3+}-doping improves the photoutilization of TiO_2 and generates more electron–hole pairs under photoirradiation, which helps to improve the photocatalytic activity of TiO_2.

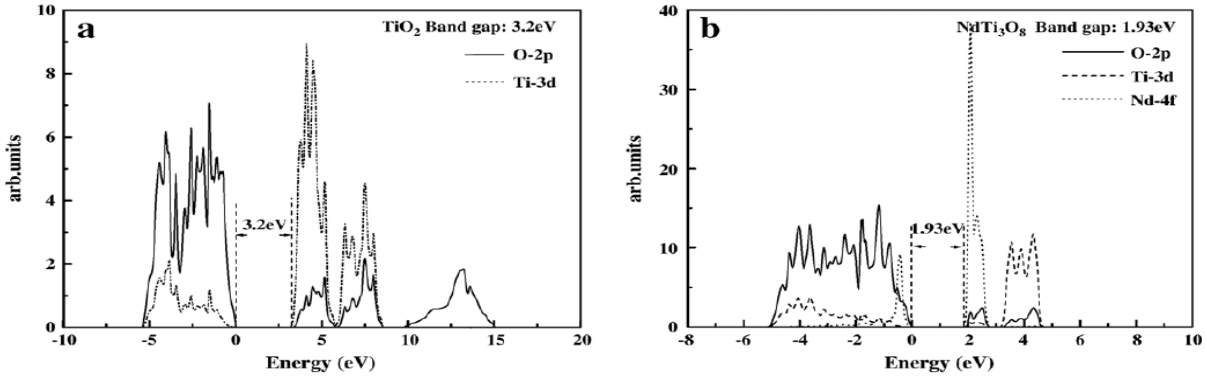

Fig. 2. Theoretically calculated density of states for undoped (a) and Nd-doped (b) TiO_2 [16].

The crystal expansion and matrix distortion of TiO_2 caused by Ho^{3+}-doping creates oxygen vacancies, which generate shallow energy states in the bottom of conduction band and serve as electron trap sites in nanocrystalline TiO_2. Meanwhile, shallow energy states introduced by the rare earth ions in the top valence band serve as hole trap sites. The separation of charge carriers is attributed to such trapping. Subsequently, the charge carriers transfer to the surface of photocatalyst to cause there redox reactions so that the photocatalytic activity of doped TiO_2 is promoted. When both Fe^3+ and Ho^{3+} are co-doped into the nanocrystalline TiO_2 particles, a synergistic effect will be produced. Fe^{3+}-doping broadens the absorption profile, improves the photoutilization of TiO_2, and thereby generates more electron–hole pairs. Ho^{3+}-doping prevents the increase of grain sizes, leads to a crystal expansion and matrix distortion and retards the recombination of photoexcited charge carriers. The photocatalytic activity of TiO_2 co-doped with Fe^{3+} and Ho^{3+} is markedly improved.

1.4 The effect of intrinsic surface properties on the photocatalytic activity

Zhang *et al.* [18] have investigated the poperties of $Dy_2Ti_2O_7$ prepared by two different methods: citric-acid sol–gel soft chemistry and solid state reaction route. $Dy_2Ti_2O_7$ nanocrystals prepared by the citric acid method have an oxygen content that is much lower than the theoretical value; the oxygen-deficiency on the $Dy_2Ti_2O_7$ surface is about 40%. This oxygen deficiency helps the catalyst to absorb more O_2 and is very benificial to achieve a good photocatalytic activity. Both the morphology and the degree, by which it can be dispersed, are quite different from those of samples produced by the solid state reaction. The $Dy_2Ti_2O_7$ crystals of samples obtained by the citric acid method are quadrilateral and have a good dispersibility, while the average crystal size is about 50 nm. It is very difficult to identify the morphology of $Dy_2Ti_2O_7$ produced by the solid state reaction and its dispersibility is quite low. The BET surface area of $Dy_2Ti_2O_7$ prepared by the citric acid method is 25 m^2/g, which is much larger than that of samples prepared by traditional solid state reaction (2 m^2/g) and other soft chemistry routes. The good physical properties of the sample obtained by the citric acid method result in a better photoactivity than that of the sample prepared by solid state reaction. For the first, the photodegradation of methyl orange is 98.6% within 60 min, whereas for the second, the degree of decomposition is only 16.0%.

2. PHYSICAL MECHANISMS RESPONSIBLE FOR THE DEGRADATION OF ORGANIC POLLUTANTS BY LANTHANIDE OXIDE DOPED TITANIA UNDER VISIBLE-LIGHT EXPOSURE

The effects of lanthanide doping on the electronic structures and optical properties of anatase TiO_2 are studied by Zhao and Liu [6]. They presented electronic structures and optical properties of pure anatase TiO_2 and lanthanide-doped TiO_2, based on calculations of the crystal structures. The results indicate that the lanthanide doping could remarkably improve the photocatalytic activity of TiO_2, and that the effect of improvement is sensitive to the atomic electronic configuration and ionic radius. Most lanthanide doping could narrow the band gap of TiO_2, so the fundamental absorption edges shift to the visible light region and simultaneously maintain strong redox potentials. In terms of the correlation of electronic structure and optical properties, the ref. [6] describes that there are three kinds of electronic transitions in lanthanide-doped TiO_2: intraband transition in lanthanide 4***f*** states, interband transition between O p_π states and lanthanide 4***f*** states and interband transition between IELs and valance band maximum or conduction band minimum (IELs is abbreviation for imputity energy levels).

2.1 Shift of the absorption from UV-light region to visible-light region by lanthanide doping

Parida and Sahu [19] have found a high photocatalytic activity for the reduction of hexavalent chromium and methylene blue degradation under visible light by La^{3+}-TiO_2 containing 0.4 mol% lanthanum, prepared by incipient wetness impregnation method and activated at 400°C. The photocatalytic activity of TiO_2 doped with lanthanides is shifted to the visible part of the spectrum (bathochromic shift). It was observed (see Fig. 3) that the absorption edges of La^{3+} doped TiO_2 shift slightly towards a longer wavelength (red shift) compared to that of pure TiO_2, for which the samples are active under visible light of the solar spectrum.

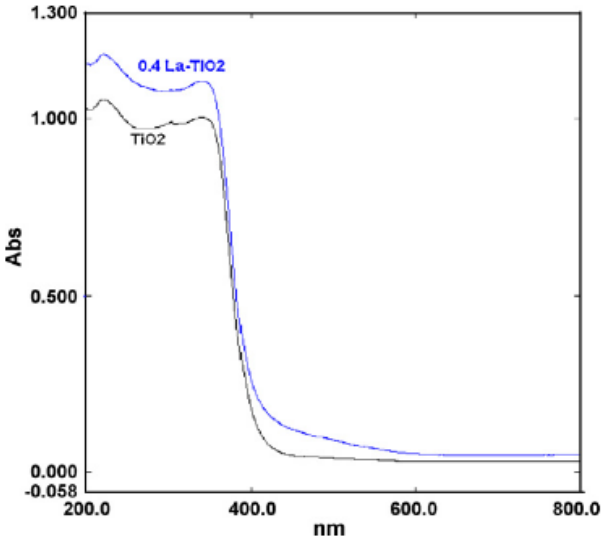

Fig. 3. UV–vis spectra of pure and La^{3+} doped TiO_2 [19].

Xiao *et al.* [20] have studied the visible light photocatalytic decomposition of methylene blue by 0.5 mol% Sm^{3+} doped TiO_2 produced by sol-gel auto-combustion synthesis. To investigate the optical absorption properties of their catalysts, they have examined the diffuse reflectance spectra (DRS) of TiO_2 and Sm^{3+}-doped TiO_2 in the range of 220–850 nm. They have found that while TiO_2 has no absorption in the visible region (>400 nm), Sm^{3+}-doped TiO_2 shows a significant absorption between 400 and 500 nm, which increases with increasing the samarium ion content. The photocatalytic activity of Sm^{3+}-TiO_2 is higher than that of undoped TiO_2, which is consistent with the larger specific surface area of Sm^{3+}-TiO_2 compared to undoped TiO_2. However, it is noticeable that the larger specific surface area of Sm^{3+}-TiO_2, resulting from a higher samarium ion dosage does not lead to a higher photocatalytic activity, which might be limited by a lower separation efficiency of electron–hole pairs.

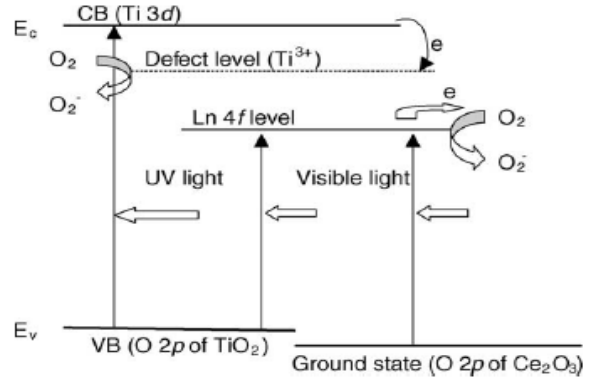

Fig. 4. The photoluminescence emission mechanmisms of TiO_2 and Ce^{3+}–TiO_2 catalysts at 77 K [21].

Li *et al.* [21] have found enhanced photocatalytic activity of Ce^{3+}–TiO_2 prepared by a sol–gel process for the degradation of 2-mercaptobenzothiazole in aqueous suspension for odor control. They have investigated the optical absorption properties of TiO_2 and Ce^{3+}–TiO_2 catalysts in the range of 220–850 nm and have found that while TiO_2 has no absorption in the visible region (>400 nm), Ce^{3+}–TiO_2 has a significant absorption between 400 and 500 nm, which increases with increasing the cerium content. CeO_2 is a n-type semiconductor with a band gap of about 3.2 eV [22,23]. Therefore, the absorption at 400–500 nm can not be attributed to CeO_2, but should rather be due to Ce_2O_3. In contrast to the closed shell of Ce^{4+}-ion ($4\boldsymbol{f}^0$), the Ce^{3+}-ion possesses a single optically active electron with the ground-state configuration in the $4\boldsymbol{f}^1$-orbital. Within this configuration, there are only two electronic levels, the $^2F_{7/2}$ excited state and the $^2F_{5/2}$ ground state. The $4\boldsymbol{f}$–$4\boldsymbol{f}$ transitions attributed to Ce^{3+} can only be observed in the infrared spectral region. However, Ce^{3+} has a first state configuration $5\boldsymbol{d}^1$ that is rather close in energy. The electronic dipole transitions $4\boldsymbol{f}^1 \leftrightarrow 5\boldsymbol{d}^1$ may occur in either the UV or visible region. Based on the valence band of Ce^{3+}–TiO_2 as determined by XPS, the authors propose that electron hole pairs are generated in both types of catalysts (Ce^{3+}-TiO_2 and Ce_2O_3) by two mechanisms shown in Fig. 4. According to Eq. (7) , an electron can be excited from the valence band of Ce^{3+}–TiO_2 into the Ce 4 ***f***-level when the energy of the photon is more than ($\boldsymbol{E_{Ce4f} - E_v}$). Equation (8) shows the excitation of an electron from the ground state of Ce_2O_3 into the Ce 4 ***f***-level.

Therefore, the red shift of the absorption edge for Ce^{3+}–TiO_2 is explained by the following two reactions. The Ce 4***f*** levels may play a crucial role in generating electron-hole pairs under visible light illumination.

$$Ce^{3+}-TiO_2 + h\nu \rightarrow e^- + h^+ \quad (7)$$

$$Ce_2O_3 + h\nu \rightarrow e^- + h^+ \quad (8)$$

The optimal dosage of cerium under visible light illumination is found to be 0.7%, while for UV illumination it is 1.2%. Ikeda *et al.* [24] have proposed that the rate of electron-holes escaping from their recombination should be proportional to the light flux of excitation and to the probability of light absorption to produce an electron-hole couple (F). This means that the optimal dosage may be

dependent on the reaction conditions. The value of F under visible light illumination is much lower than that under UV illumination in this study. The lower F value might lead to a lower Ti^{3+} content. Therefore, the optimal dosage of ceria under visible light illumination is lower than that under UV illumination at these experimental conditions.

2.2 The effect of co-doping on the photocatalytic activity

Xu *et al.* [25] have prepared Ce, C-codoped TiO_2 nanoparticles through a modified sol–gel method under mild conditions and have studied their photocatalytic activity under visible light. The UV–vis spectra of the TiO_2 samples (plotted in Fig. 5) show that Ce, C-codoped titania has a greatly improved absorption of visible light.

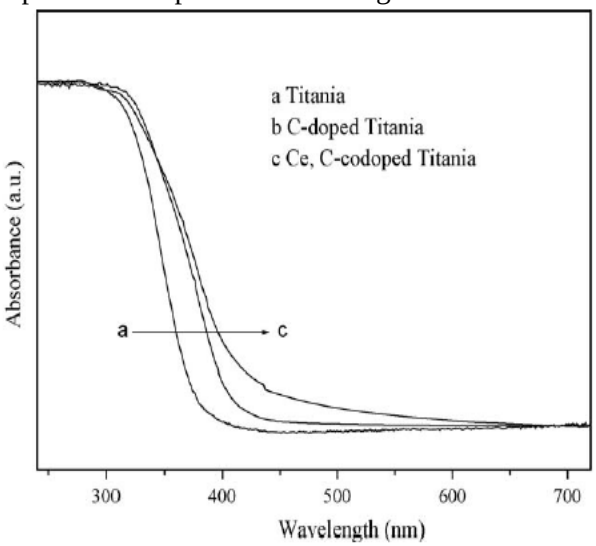

Fig. 5. UV-Vis spectra of Ce, C-codoped titania particles [25].

The authors claim that the distance of charge transfer between the ***f***-electrons of the cerium ions (or the C dopant) and the conduction or valence band of TiO_2 is narrowed, thus allowing visible light absorption. The energy level of Ce^{4+}/Ce^{3+} is 1.8 eV. The introduction of such energy level in the band-gap can give rise to the red-shift in the band-gap transition. The Ce 4***f*** level also plays an important role in the interfacial charge transfer and elimination of the electron-hole recombination.

2.3 Shift of the absorption from the UV region to the visible light region by organic dye sensitizing

Xie and Yuan [26] have demonstrated an effective photodegradation of reactive brilliant red dye (X-3B) with the reaction system dye/Ce^{4+}-TiO_2/visible-light prepared by chemical coprecipitation–peptization and hydrothermal synthesis. The optical band gap energy of TiO_2 sol is estimated to be 350 nm by measuring the UV-Vis spectra for TiO_2 and Ce^{4+}-TiO_2 sol. Both TiO_2 and Ce^{4+}-TiO_2 sols have similar UV-Vis absorption spectra except for the absorption intensity at the maximum wavelength (λ_{max} = 202 nm). There was no apparent absorption in the visible-light range ($\lambda >$ 400 nm). This means that the sol–sol system cannot be directly excited by visible light irradiation. The absorption band shows a blue shift, which is due to the quantum size effect of sol nanoparticles. The experimental results, however, show that the dye photobleaching reaction occurs on Ce^{4+}-TiO_2 (both sol and nanocrystalline system) under visible light. The photosensitized photocatalysis reaction mechanism of dye bleaching in the Ce^{4+}-TiO_2 sol system is shown in Fig. 6.

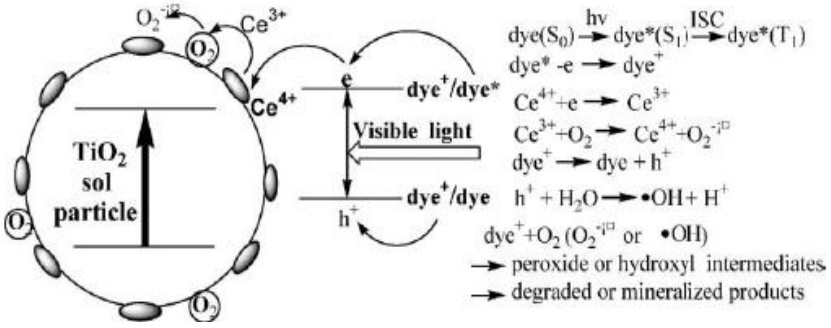

Fig. 6. Photosensitized photocatalysis mechanism of the Ce^{4+}-TiO_2 sol system [26].

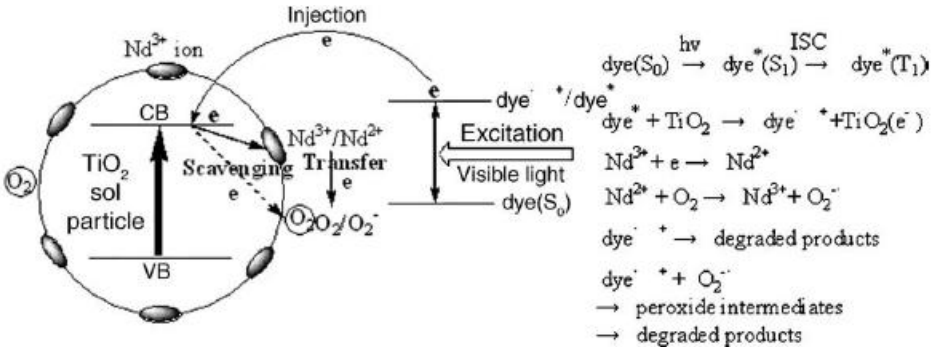

Fig. 7. Sensitized photocatalysis mechanism in the Nd^{3+}–TiO_2 sol system (S_0 = singlet ground state, S_1 = first excited singlet, T_1 = first excited triplet state, ISC = intersystem crossing) [27].

It can be seen from Fig. 6 that the Ce^{4+}-TiO_2 sol particles are physically adsorbed on the surface of sol particles and a dye molecule is excited by the absorption of a visible-light photon. The dye molecule in the excited state can then transfer electrons to the Ce^{4+} ion. Meanwhile, the positively charged vacancies (h^+) remaining on the dye molecule can extract electrons from hydroxyl species in the solution to produce hydroxyl radicals ($HO^•$). These radicals are strong electrophiles capable of oxidizing and destroying organic molecules in aqueous media. In this process, the Ce^{4+} species act as electron scavengers to trap the excitation electrons of the excited dye molecules. In this way they behave as being apparently superior to the oxygen molecule (O_2) which is also able to do that. The electrons trapped in Ce^{4+} sites are subsequently transferred to the adsorbed surrounding O_2. The presence of Ce^{4+} on the surface of sol nanoparticles may promote the following reactions: $Ce^{4+} + e^- \rightarrow Ce^{3+}$ and $Ce^{3+} + O_2 \rightarrow Ce^{4+} + O^{•-}_2$. This is then also followed by the destruction of dye molecules with the interaction of holes (h^+) and hydroxyl radicals ($HO^•$).

Xie and Yuan [27] have also studied the enhanced photocatalytic activity of active brilliant red dye X-3B in a hydrosol reaction system of Nd^{3+}–TiO_2 sol in comparison to TiO_2 sol. They have ascribed the obtained enhancement to the electron trapping effect of the modified Nd^{3+} ions on TiO_2 sol particles. The neodymium-ion modified titania sol is prepared by a chemical coprecipitation–peptization and its photoactivity is studied by investigating the photodegradation efficiency of active dye X-3B in the hydrosol reaction system. Under visible light irradiation (λ > 400 nm), Nd^{3+}–TiO_2 sol shows a higher photocatalytic activity than the TiO_2 sol, which is ascribed to the electron trapping effect of modified Nd^{3+} ions on the TiO_2 sol particles. The photosensitization-photocatalysis mechanism is also discussed; the authors have proposed that the mechanism starts with the excitation of a X-3B dye molecule with visible light, followed by electron injection or electron transfer from the excited dye molecule to the conduction band of the semiconductor TiO_2, as shown in Fig. 7.

In this sol photocatalysis system, a dye molecule physically adsorbed on the surface of a sol particle is excited by the absorption of a suitable visible light photon. The electron from the excited dye molecule can be injected into the conduction band of TiO_2. Then these electrons can be trapped by electron scavengers (usually oxygen molecules). However, the electrons are also extremely susceptible for recombination with the cation radicals if the injected electrons accumulate in the conduction band of TiO_2. Therefore, the electron trapping and electron transfer are the two key steps to inhibit electron–cation radical recombination. The cation radical ($dye^{•+}$) produced by the electron injection is less stable than the ground state of the compound (dye). As a result, the unstable cation radical of dye may either directly degrade to products or react with superoxide radical anion ($O_2^{•-}$) to produce degradation products. The photocatalysis of TiO_2 sol and P25 TiO_2 powder can be explained by the above reaction mechanism. However, in the photocatalysis with Nd^{3+}–TiO_2 sol system, the Nd^{3+} species can act as effective electron scavengers to trap the conduction band electrons of TiO_2 that have been injected from the excited dye molecules. Nd^{3+} ions, as a Lewis acid, apparently are superior to oxygen molecules (O_2) in their ability to trap electrons. The electrons trapped

on Nd^{3+} sites (Nd^{2+}) are subsequently transferred to the surrounding adsorbed O_2 by an oxidation process. The presence of Nd^{3+} on the surface of TiO_2 sol nanoparticle may promote the following processes: $Nd^{3+} + e^- \rightarrow Nd^{2+}$ and $Nd^{2+} + O_2 \rightarrow Nd^{3+} + O_2^{\bullet -}$. More effective electron trapping and transferring will produce more cation radicals, which are more active to undergo degradation. Therefore, Nd^{3+} TiO_2 sol shows a superior photocatalytic activity in comparison with the TiO_2 sol and P25 TiO_2 powder.

Xie and Yuan [28] have also studied the activity of Nd^{3+}–TiO_2 nanocolloids for the photodegradation of phenol in water solution by visibile light, and have explained the observed enhancement with self-sensitization and sub-band gap overlapping. The AFM micrograph and XRD show that sol particles (10 nm in size) are well developed in the whole dispersion system and have a semicrystalline structure. The difference in ion radius (1.13 nm for Nd^{3+} and 0.64 nm for Ti^{4+}) means that the neodymium(III) ion is unlikely to be built effectively into the crystal lattice of bulk TiO_2 when the Nd^{3+}–TiO_2 sol crystallizes at 62°C. However, during the peptizing and digesting processes, Nd^{3+} can bond with non-bridging oxygen ions at the surface of –Ti–O–Ti–O– bulk network structure. After crystallization, the sol system forms with individual TiO_2 particles crosslinked with neodymium cations at the surface, which form NdOCl molecules. NdOCl is sensitive to visible light, but its discrete energy levels cannot be split into well divided band gaps. Due to the character of electronic arrangement of neodymium with partially filled atomic ***d*** or ***f*** shells, electrons can be excited and transferred from the Nd^{3+} $4f^3$-orbitals by absorbing visible-light photons of the right energy. The surrounding Nd^{3+} ions may react with the Nd^{4+} produced by a self-sensitization process, thus forming a positively charged neodymium cluster $(Nd_n)^{m+}$ (m > 3n). This neodymium cluster has empty multi energy levels below the conduction band of crystalline TiO_2. Their presence allows a new electronic transition from the TiO_2 valence band to the empty energy levels of neodymium cluster known as a sub-band gap. This transition requires less energy than the TiO_2 valence-conduction band transition (3.2 eV) and can be induced by visible light. Simultaneously, the positively charged vacancies (h^+) in the TiO_2 valence band can extract electrons from the hydroxyl species to produce hydroxyl radicals ($^{\bullet}OH$), by which organic molecules as well as other oxidizable species can be degraded. Figure 8 shows the photocatalytic reaction mechanism in the Nd^{3+}–TiO_2 sol system.

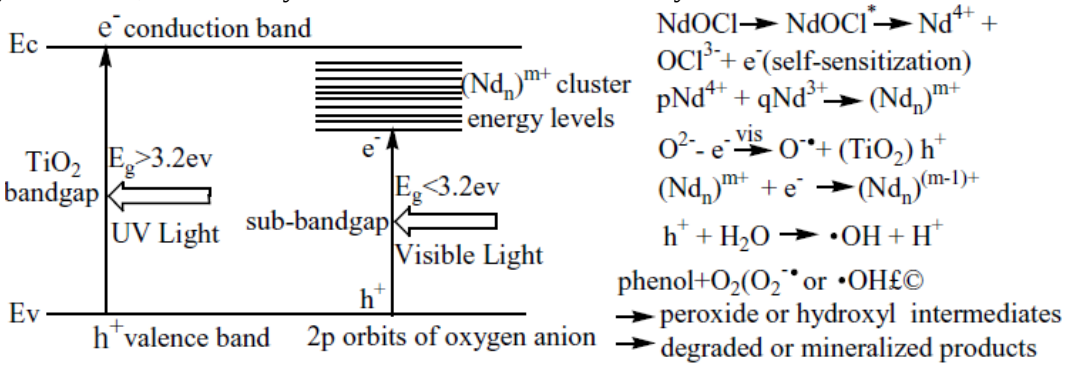

Fig. 8. Photocatalytic mechanism of Nd^{3+}–TiO_2 sol/visible light system [28].

Xie *et al.* [29] have then studied photosensitized and photocatalyzed degradation of azo dye using Ln^{n+}-TiO_2 sol in aqueous solution under visible light irradiation. They have developed a new method of chemical coprecipitation–peptization to synthesize a crystalline TiO_2 sol at a low temperature (<100°C), which is attractive to further improve the photocatalytic activity of TiO_2 catalysts. Compared to most TiO_2 powders, these TiO_2 sol catalysts have several advantages: (1) finer particle size with more uniform distribution and better dispersion in water; (2) stronger interfacial adsorption ability; and (3) easy coating on different supporting materials including substrates with a poor heat resistance such as polymers, optical fibers, plastics, wood, and paper.

It is generally believed that pure TiO_2 can not be directly excited by visible light due to its high band-gap of 3.2 eV. The system X-3B dye/Ln^{3+}-TiO_2 has an entirely different mechanism of photo-excitation under visible light illumination. The X-3B dye sensitization process involves the excitation of dye

molecules by absorbing visible light photons, followed by the electron injection from excited dye molecules to the TiO_2 conduction band. Then the electrons are transferred from the conduction band to the working electrode (ITO conductive film) and finally form out-circuit. In such as system (dye/Ln^{n+}-TiO_2/vis hydrosol), the Ln^{n+}-TiO_2 particles act as a bridge band connecting the X-3B dye and the working electrode. Some key reactions are shown in Eqs. (9–14):

$$\text{Dye} + h\nu \rightarrow \text{dye}^* \quad (9)$$

$$\text{Dye}^* + \text{TiO}_2 \rightarrow \text{TiO}_2(e^-) + \text{dye}^{\bullet+} \quad (10)$$

$$\text{TiO}_2(e^-) + \text{O}_2 \rightarrow \text{O}_2^{\bullet-} + \text{TiO}_2 \quad (11)$$

$$Ln^{n+} + \text{TiO}_2(e^-) \rightarrow Ln^{(n-1)+} + \text{TiO}_2 \quad (12)$$

$$Ln^{(n-1)+} + \text{O}_2 \rightarrow \text{O}_2^{\bullet-} + Ln^{n+} \quad (13)$$

$$\text{O}_2^{\bullet-} + \text{dye}^{\bullet+} \rightarrow \text{intermediates or final products} \quad (14)$$

In the above reactions, the dye can be excited under visible light illumination (Eq. 9). The dye molecule in the excited state can then transfer electrons into the conduction band of TiO_2 (Eq. 10) that may be trapped by the electron scavengers such as oxygen molecule that usually surround the sample (Eq. 11). If the transferred electrons accumulate in the conduction band of TiO_2, recombination between cationic radicals and the electrons is extremely likely. Therefore, the electron trapping (Eq. 12) and electron transfer (Eq. 13) are two key steps to inhibit electron-cationic radical recombination. The cationic radical ($dye^{\bullet+}$) produced by electron injection is less stable than the probe molecule in the ground state. As a result, the unstable dye cationic radicals can be directly degraded into decomposition products by reacting with super-oxidizing anionic radials or other active oxygen ($HO^{\bullet}$, $HOO^{\bullet}$ and $O_2^{\bullet-}$) (Eq. 14). The lanthanide ion that TiO_2 is doped with plays an important role in promoting significantly the electron trapping and electron transfer in the dye/Ln^{3+}-TiO_2 hydrosol system. The photosensitization reaction mechanism and potential states in the dye/Ln^{n+}-TiO_2/vis system are further illustrated in Figs. 9 and 10.

Su *et al.* [30] have studied the visible light photocatalysis on praseodymium(III)-nitrate-modified nanocrystalline TiO_2 5 nm in particle diameter, that is prepared by an ultrasound method in a sol–gel process at low temperature. The UV–vis diffuse reflectance spectra of the $Pr(NO_3)_3$-TiO_2 and undoped TiO_2 samples show that both samples have a strong absorption at wavelengths below 400 nm, which is attributed to the transitions of electrons from the valence band to the conduction band of TiO_2. Visible light absorptions at 444, 469, 482 and 590 nm are observed for $Pr(NO_3)_3$-TiO_2 only, which are attributed to the 4***f***-transitions $^3H_4 \rightarrow {}^3P_2$, $^3H_4 \rightarrow {}^3P_1$, $^3H_4 \rightarrow {}^3P_0$ and $^3H_4 \rightarrow {}^1D_2$ of praseodymium(III) ions. This absorption feature suggests that the photocatalyst can be activated throughout the visible wavelengths where the light absorption occurs. The sample shows a high activity and stability in the decomposition of rhodamine-B (RhB) and 4-chlorophenol (4-CP) under visible light

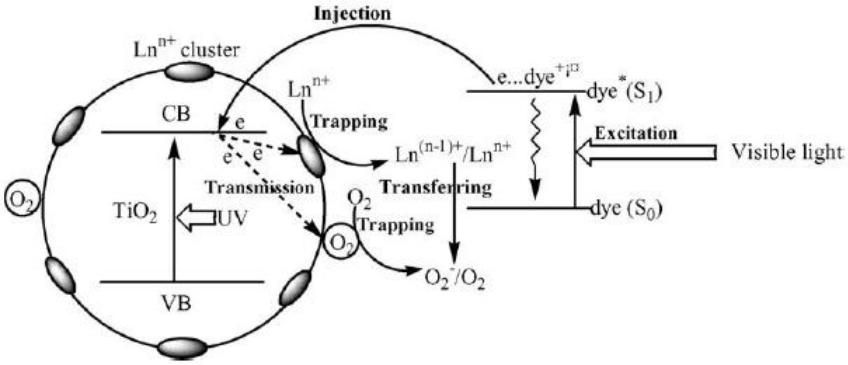

Fig. 9. Proposed mechanism of photosensitization reaction in the system dye/Ln^{n+}-TiO_2/vis [29].

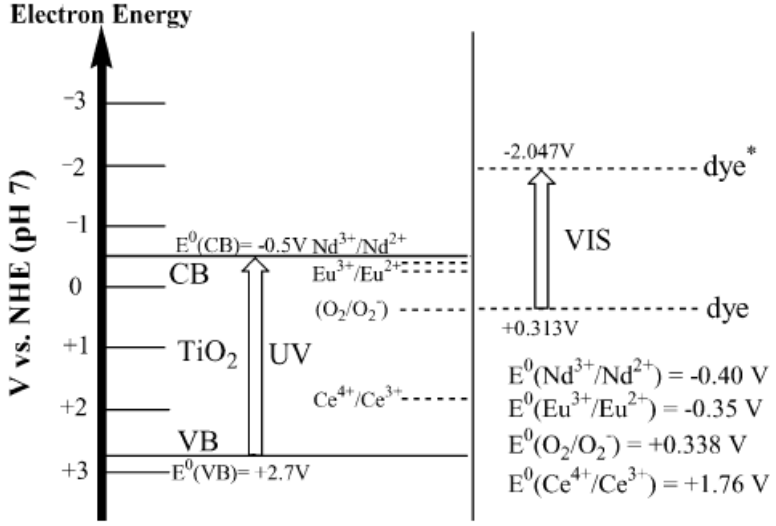

Fig. 10. Schematic illustration of the valence and conduction band potentials of TiO_2 and excitation and ground state potentials of the X-3B molecule along with the standard reduction potentials of lanthanide ion pairs [29].

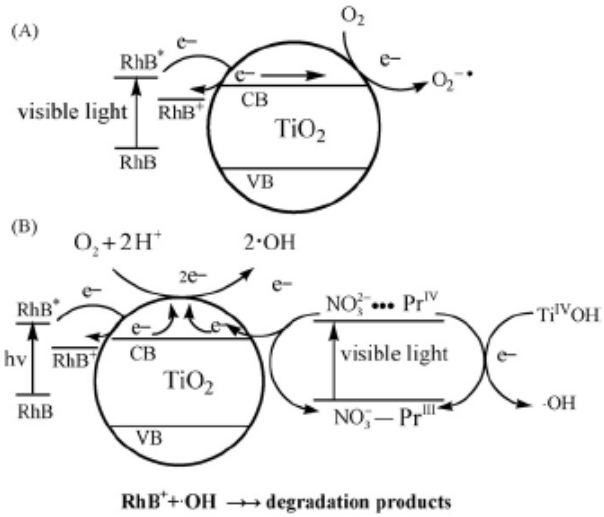

Fig. 11. Postulated mechanism for the visible light-induced oxidative degradation of RhB in aerobic aqueous media on TiO_2 (A) and $Pr(NO_3)_3$-TiO_2 (B) surfaces [30].

irradiation. From the investigation of photoinduced conversion of RhB, carried out under visible light illumination at wavelengths greater than 420 nm in aqueous $Pr(NO_3)_3$-TiO_2 dispersions, one can conclude that RhB photodegrades by a pathway that is distinct from the pathway prevailing in the pure TiO_2 dispersion. The latter pathway is related to self-photosensitization of RhB as shown in Fig. 11A.

The results presented above reveal that a completely different mechanism of charge generation must operate for the $Pr(NO_3)_3$-TiO_2 photocatalysts. The authors postulate as a working hypothesis a simple mechanism depicted in Fig. 11B. The local excitation of praseodymium(III) nitrate under visible light irradiation yields a metal-to-ligand charge-transfer transition $4f(Pr^{3+})(^3H_4 \rightarrow {}^3P_2, {}^3P_1, {}^3P_0$ and $^1D_2) \rightarrow \pi^*$ (NO_3^-), which produces Pr^{4+} and NO_3^{2-}-intermediates. The labile NO_3^{2-} anion intermediate will rapidly transfer electrons to the conduction band of TiO_2. The strong oxidizing Pr^{4+} ions (standard redox potentials of $E_0(Pr^{4+}/Pr^{3+}) = +2.86$ V, and $E_{vb}(TiO_2) = +2.7$ V) attract electrons from either the surface OH^- groups and/or the surface H_2O molecules to produce hydroxyl radicals through the reaction depicted in Fig. 11B (evidence for this is found in the ESR spectrum). This electron transfer leads to efficient charge separation and effectively suppresses the recombination between Pr(IV) and NO_3^{2-} by the surrounding TiO_2 matrix. In the absence of $Pr(NO_3)_3$, the titania cannot be directly excited by visible light due to its 3.2 eV band-gap, but the photobleaching reaction still occurs in the TiO_2/dye/visible light system due to the dye molecule acting as a photosensitizer. Molecular O_2 adsorbed on TiO_2 acts as an electron scavenger to trap the excitation electrons of the excited dye molecules, thus producing superoxide radical $(O_2^{\bullet-})$, so that the extent of photoactivity is somewhat lessened. The difference in ESR spectra observed with respect to the kind of active oxygen species produced between the $Pr(NO_3)_3$-TiO_2 and TiO_2 dispersions is then understandable. In addition to the local excited photocatalysis, the dye assisted photosensitization also plays an important role in the photo-oxidative degradation of RhB in the dye/TiO_2 system. The produced superoxide radical is reduced by the electron from NO_3^{2-} to form $^{\bullet}OH$,

as shown in Fig. 11B. Therefore, the photocatalysis and photosensitization simultaneously occur under visible light irradiation. It is clearly shown that the photocatalytic oxidation is superior to the photosensitized oxidation, and the photocatalytic process will surely help to improve the overall photodegradation efficiency and make the bleaching reaction more feasible.

Mele *et al.* [12] have compared the photocatalytic activity of TiO_2 samples impregnated with lanthanide diphthalocyanines with those impregnated with Cu(II)-porphyrin. The photocatalytic degradation of 4-nitrophenol (4-NP) in aqueous suspension is used as a probe reaction. Commercial anatase TiO_2 is impregnated with home-prepared double-decker phthalocyanine complexes of the lanthanide metals, such as Ce, Pr, Nd, Sm, Ho, and Gd. In particular, the impregnation with Ho, Sm, and Nd complexes, acting as sensitizers, proves beneficial for the photoactivity of studied systems. Significant improvements of the TiO_2-based catalytic system seem possible in terms of lower impregnation loading, enhanced photoreactivity under solar light irradiation, as well as chemical, thermal, and photochemical stability of the sensitizers in comparison with those using Cu(II)-porphyrin.

No appreciable shift of the band gap edge of TiO_2 can be observed for all of the samples from the diffuse reflectance spectra of bare TiO_2 and some $LnPc_2$-loaded TiO_2 photocatalysts recorded in the range of 250-800 nm. Nevertheless, all of them reflect less light than the bare support, and the absorption increases with increasing of loading. All of the spectra of the $LnPc_2$-TiO_2 samples present quite similar patterns, independent of the coordinated lanthanide metal, showing absorption maxima at nearly the same λ- value. The characteristic bands are due to the strong absorption, particularly within the Q-range (ca. 650-680 nm), by the $LnPc_2$ particles deposited on the TiO_2 grains. The bands are relatively broad compared to the respective solution spectra, and all of the studied samples show similar large absorptions that cover the visible range fairly well. Moreover, the spectra of $SmPc_2$, $GdPc_2$, and $HoPc_2$ show distinct absorption peaks at ca. 460 nm, similar to the pesaks in dichloromethane and in nujol suspension. The $LnPc_2$ sensitizers probably enhance the absorption of studied samples also within the near-UV range (ca. 300-350 nm, B band).

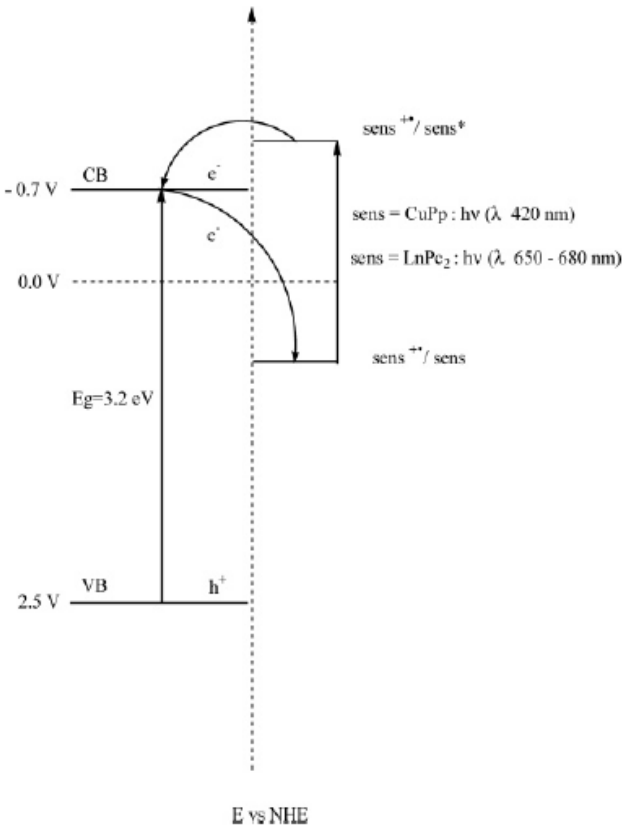

Fig. 12. Conduction Band (CB) and Valence Band (VB) energy levels of anatase TiO_2 at neutral pH and redox potentials of the various sensitizers considered in this study [12].

Figure 12 shows the conduction band and the valence band energy levels of anatase TiO_2 along with the redox potentials of some sensitizers similar to those used in this study and reported in the literature, as well as the possible charge transfer processes involving an injection of an electron from the excited sensitizers to the conduction band of TiO_2 and from the conduction band of TiO_2 to the sensitizers.

The presence of two phthalocyanine macrocycles in $LnPc_2$ favors probably a better delocalization of the positive charges during certain stages of the radical photocatalytic mechanism compared to "classic" porphyrins and phthalocyanine systems previously used as sensitizers. However, it is not easy to obtain a direct experimental evidence for this hypothesis. In addition, the formation of singlet oxygen [$^1O_2(^1\triangle)$] in higher quantities, promoted by the photoexcited $LnPc_2$ sensitizers (sens), as shown bellow by eqs 15 and 16, and suggested elsewhere, may not be excluded.

$$[\text{sens}] \xrightarrow{h\nu} {}^1[\text{sens}]^* \xrightarrow[(\text{isc})]{\text{intersystem crossing}} {}^3[\text{sens}]^* \quad (15)$$

$$^3[\text{sens}]^* + {}^3O_2 \rightarrow [\text{sens}] + {}^1O_2({}^1\Delta) \quad (16)$$

3. CONCLUSIONS

This review presents a summary of the attempts made by different researchers in the past decades to shift the absorption of TiO_2 from UV-light to the visible light region by lanthanide doping. To understand the factors, by which TiO_2 doping by lanthanides can increase the photocatalytic activity under solar irradiation, the first chapter presents brieflly the physical mechanisms responsible for the degradation of organic pollutants by lanthanide oxide doped titania under UV-light exposure. Some typical examples are presented, where the enhancement of photocatalytic activity of TiO_2 powder is due to the suppression of electron-hole recombination with trapping of photogenerated electrons at the interface, the different effects of mesoporous wall, the co-doping and the intrinsic surface properties. Based on these findings, the second chapter presents the ways of increasing the photocatalytic activity of catalysts under visible-light exposure. The shift of photocatalytic activity of catalysts towards visible-light by bathochromic shift, co-doping and organic dye sensitizing of lanthanide oxide doped titania are presented.

Acknowledgments. *This study was performed with the financial support of the NATO "Science for Peace" Programme (Contract SfP 982835) as well of project DO02-252 of the National Science Fund of Bulgaria. The authors are thankfull to Dr. C. Dushkin (Faculty of Chemistry, University of Sofia) and Dr. R. Smits (Catalysis Services International, Sofia) for the valuable discussions.*

REFERENCES

1. A. Fujishima, K. Honda, *Nature*, **238**, 37 (1972).
2. M. R. Hoffmann, S. T. Martin, W. Choi, D. W. Bahnemannt, *Chem. Rev*., **95**, 69 (1995).
3. A. M. Volodin, *Catal. Today*, **58**, 103 (2000).
4. T. Kako, Z. Zou, M. Katagiri, J. Ye, Chem. Mater., **19**, 198 (2007).
5. C. A. Koval, J. N. Howard, *Chem. Rev.*, **92**, 411(1992).
6. Z. Zhao Q. Liu, *J. Phys. D: Appl. Phys.*, **41**, 085417 (2008).
7. J. L. Gole, J. D. Stout, C. Burda, Y. Lou, X. Chen, *J. Phys. Chem. B*, **108**, 1230 (2004).
8. Z. Li, H. Xue, X. Wang, X. Fu, *J. Molec. Catal. A: Chem.*, **260**, 56 (2006).
9. S. Rengaraj, S. Venkataraj, Jei-Won Yeon, Y. Kim, X.Z. Li, G.K.H. Pang, *Appl. Catal. B: Env.*, **77**, 157 (2007).
10. A. Scalfani, J.M. Hermann, *J. Photochem. Photobiol. A*, **113**, 181(1998).
11. H. Yang, K. Zhang, R. Shi, A. Tang, *J. Am. Ceram. Soc*., **90**, 1370 (2007).
12. G. Mele, E. García-López, L. Palmisano, G. Dyrda, R. Słota, *J. Phys. Chem. C*, **111**, 6581 (2007).
13. H. Q. Jiang, P. Wang, X. L. Guo, and H. Z. Xian, *Rus. Chem. Bull.*, **55**, 1743 (2006).
14. A. N. Ökte, Ö. Yılmaz, *Appl. Catal. A: Gener.* **354** 132 (2009).
15. T. Peng, De Zhao, H. Song, C. Yan, *J. Molec. Catal. A: Chem.*, **238,** 119 (2005).
16. De Zhao, T. Peng, J. Xiao, C. Yan, X. Ke, *Mater. Lett.*, **61,** 105 (2007).
17. J.-W. Shi, J.-T. Zheng, Y. Hu, Y.-C. Zhao, *Mater. Chem. Phys.*, **106,** 247 (2007).
18. L. Zhang, H. Zhong, W. Zhang , L. Lu, X. Yang, X. Wang, *J. Alloy. Comp.*, **463,** 466 (2008).
19. K. M. Parida, N. Sahu, *J. Molec. Catal. A: Chem.*, **287**, 151 (2008).
20. Q. Xiao, Z. Si, Z. Yu, G. Qiu, *Mater. Sci. Eng.* B, **137**, 189 (2007).
21. F. B. Li, X. Z. Li, M. F. Hou, K.W. Cheah, W. C .H. Choy, *Appl. Catal. A: Gen.*, **285**, 181 (2005).
22. B. Elidrissi, M. Addou, M. Regragui, C. Monty, A. Bougrine, A. Kachouane, *Thin Solid Films*, **379,** 23 (2000).
23. S.Y. Zheng, A. M. Andersson-Faldt, C. G. Granqvist, *Appl. Opt.*, **32**, 6303 (1993).
24. S. Ikeda, N. Sugiyama, B. Pal, G. Marci, L. Palmisano, H. Noguchi, K. Uosaki, B. Ohtani, *Phys. Chem. Chem. Phys.*, **3**, 267 (2001).
25. J. Xu, Y. Ao, D. Fu, *Appl. Surf. Sci.*, **256,** 884 (2009).
26. Y. Xie, C. Yuan, App. Catal. B: Envir., **46**, 251 (2003).
27. Y. Xie, C. Yuan, X. Li, *Coll. Surf. A: Physicochem. Eng. Aspects*, **252**, 87 (2005).
28. Y. Xie, C. Yuan, *Appl. Surf. Sci.*, **221**, 17 (2004).
29. Y. Xie, C. Yuan, X. Li, *Mater. Sci. Engin. B*, **117**, 325 (2005).
30. W. Su, J. Chen, L. Wu, X. Wang, X. Wang, X. Fu, Appl. *Catal. B: Envir.*, **77**, 264 (2008).

ТИТАНОВ ДИОКСИД С ДОБАВКИ ОТ ЛАНТАНОИДИ КАТО ФОТОКАТАЛИЗАТОР ЗА РАЗГРАЖДАНЕ НА ОРГАНИЧНИ ЗАМЪРСИТЕЛИ ПРИ ОБЛЪЧВАНЕ С УЛТРАВИОЛЕТОВА И ВИДИМА СВЕЛИНА

Д. Ц. Димитров*, М. М. Миланова, Р. П. Кралчевска

Катедра Обща и неорганична химия, Химически факултет,Софийски университет, бул. Джеймс Баучър 1, София 1164, България

Постъпила на 2 Ноември 2010 г.; Преработена на 5 януари 2011 г.

(Резюме)

Основната цел поставена при написването на този кратък обзор е да представи най-значимите изследвания, които бяха проведени през последните десетилетия, свързани с изместването на поглъщането на TiO_2 от ултравиолетовата във видимата област чрез добавки от лантаноиди. С цел да се внесе ясност в другите фактори, чрез които внасянето на лантаноиди в TiO_2 увеличава неговата фотокаталитична активност при облъчването му с видима светлина, първата част на обзора е посветена на физическите механизми, причиняващи разграждането на органични замърсители от модифициран с лантаноиди TiO_2 при облъчването му с ултравиолетова светлина. Тази тема е изследвана много по-отдавна и по-добре изучена. Втората част на представения обзор представя отново тези механизми, но при облъчване на катализатора с видима светлина. Там подробно са разгледани най-типичните изследвания свързани с намаляването на ширината на забранената зона на TiO_2, ефекта на съвмесното модифициране едновременно с две добавки и ефекта на сенситизирането с помощта на органични оцветители при модифицираният с лантаноиди титанов диоксид.

Bulgarian Chemical Communications, Volume 43, Number 4 (pp 502 – 509) 2011

Kinetics of phenol degradation and growth of predominant *Pseudomonas* species in a simple batch stirred tank reactor

P. Saravanan[1*], K. Pakshirajan[2], P. Saha[3]

[1] *Department of Civil Engineering, University of Malaya, Kuala Lumpur -50603, Malaysia*
[2] *Department of Chemical Engineering, Indian Institute of Technology Guwahati, Guwahati-781039, India*
[3] *Department of Biotechnology, Indian Institute of Technology Guwahati, Guwahati-781039, India*

Received August 8, 2010; Accepted February 21, 2011

A culture predominantly consisting of the *Pseudomonas* species was isolated from a sewage treatment plant and was utilized to study phenol degradation and culture growth kinetics. The culture was capable of completely degrading phenol at a maximum initial concentration up to 400 mg/l in a simple batch stirred tank reactor. The maximum time taken to degrade phenol at this concentration level was 194 h. Kinetics of phenol degradation at various initial concentrations in the media largely exhibited zero order rate with a maximum value of the coefficient of determination (R^2) = 0.99 at 400 mg/l of phenol. Deterministic models such as those of Haldane, Han-Levenspiel, Luong, Edward, Yano and Koga, Tseng and Wayman were employed to fit the data of substrate inhibition on the kinetics of culture growth and phenol degradation. All models tested, except the Tseng and Wayman model fitted well the experimental data.

Keywords: Batch stirred tank reactor; biodegradation; phenol; substrate inhibition models; *Pseudomonas* sp.

1. INTRODUCTION

Synthetic organic chemicals like phenols and its derivatives lead to severe environmental contamination due to their toxicity towards aquatic biota. In particular, various types of industries such as pulp and paper mills, herbicides and fungicides production, etc., discharge phenols in their aqueous effluents [1,2]. The growing need of controlling the discharge of wastewater containing phenols and other organics into the environment has led to the search for better wastewater treatment methods.

Among the available methods for treating phenols in wastewater before its discharge into the environment, microbe based degradation of phenols seems more promising. Aerobic degradation of phenol using pure microbial cultures has been studied extensively; for example, *Pseudomonas putida* has been widely studied for its phenol biodegradation potential [3-5]. Aerobic degradation with a mixed culture may be advantageous in complete degradation of phenols without leaving any hazardous residues in the processed medium. Moreover, investigating the degradation kinetics of phenol in a suitable reactor system using mixed microbial culture further leads to its better applicability in a given wastewater treatment facility.

In order to evaluate the potential of a mixed microbial culture, isolated from a sewage treatment plant, in phenol degradation, batch experiments were performed in a simple stirred tank reactor with an objective to investigate the culture growth and degradation kinetics in the system and its modeling.

2. MATERIALS AND METHODS

2.1 Chemicals and reagents

Phenol was of analytical grade and was purchased from Merck®, India. Glucose and inorganic salts used in preparing microbial growth media were of reagent grade, obtained from Sisco Research Laboratories, India.

2.2 Microorganism and culture conditions

A mixed microbial culture, capable of phenol degradation, was isolated and enriched from a sewage treatment plant located in Guwahati, India. The isolation procedure, as reported by Nuhoglu and Yalcin [6], was adopted in this study. The

* To whom all correspondence should be addressed
E-mail: pichiahsaravanan@gmail.com

culture was identified as a mixture of *Pseudomonas* species according to the biochemical tests; scanning electron microscopy also confirmed the results. It was initially grown in a 250 ml Erlenmeyer flask containing 100 ml of mineral salt medium (MSM) of the following composition: $(NH_4)_2SO_4$ 230 mg/l, $CaCl_2$ 7.5 mg/l, $FeCl_3$ 1.0 mg/l, $MnSO_4 \cdot H_2O$ 100 mg/l, $MgSO_4 \cdot 7H_2O$ 100 mg/l, K_2HPO_4 500 mg/l, KH_2PO_4 250 mg/l and glucose 2 g/L at pH 7.0 under agitation (150 rpm). The culture was then acclimatized for a period of one month to grow in MSM containing phenol as the sole carbon source up to a concentration of 800 mg/l.

2.3 Experimental setup

The experimental setup used in this phenol biodegradation study consisted of a 5-liter glass vessel fitted with an impeller driven by a DC motor. Ports for sampling, liquid addition and withdrawal (phenol in MSM) through peristaltic pump, and thermometer for monitoring the temperature inside the vessel were provided in the setup. A schematic of the setup is illustrated in Fig. 1.

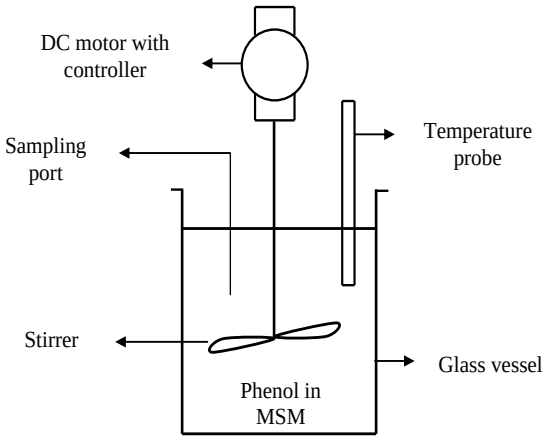

Fig. 1. Schematic of the simple batch stirred tank reactor.

2.4 Batch biodegradation study

Four batches of experiments were conducted with initial phenol concentration varying from 100 mg/l to 400 mg/l and a working volume of 4 liters of MSM using Milli-Q Elix® water. These concentration levels were chosen based on the total time taken by the culture for complete removal/degradation of phenol in the media. The experiments were carried out under batch mode at a constant temperature of 29º C ± 2º C with continuous stirring at 150 rpm. Samples were withdrawn at regular time intervals (approximately 6 hours). Samples were thereby centrifuged (10 000×g for 3 min) and analyzed for residual phenol concentration (Biofuge Pico, Rota No.3328, Heraeus). Each experiment was repeated until the residual phenol concentration in the media was reduced to nearly 0 mg/l. For each concentration duplicate experiments were performed under the same conditions and average values of each experiment were reported.

2.5 Analytical methods

Samples were centrifuged at 10 000×g for 3 min to separate the biomass. The phenol content in the biomass samples was determined quantitatively on a Perkin Elmer High Performance Liquid Chromatograph (HPLC) with a UV-Visible detector and C18 column. The dimensions of the column used were 250×4.6 mm and the particle size of the packing was 5 μm. The eluent used was a mixture of acetonitrile:water (80:20). The flow rate of the eluent was kept at 1 ml/min and the detection wavelength was 275 nm. The retention time for phenol was 3.05 min. Cell concentrations in the samples were measured as optical density at 600 nm (OD_{600}) wavelength using a Diode Array Spectrophotometer (Spekol 1200, Analytik Jena, Germany) and correlated to biomass concentration.

3. RESULTS AND DISCUSSION

In order to establish the potential of the culture in higher-scale phenol degradation, the kinetics of phenol degradation and growth of the culture in a simple batch stirred tank reactor of higher volume were investigated.

3.1 Biomass growth and phenol degradation at different initial phenol concentrations

Fig. 2(a-d) shows the time profile of biomass growth (OD_{600}) and phenol degradation by the culture. It is seen that the time taken by the culture to degrade phenol was dependent on the initial phenol concentration in the media. The culture could, however, degrade well up to a maximum concentration of 400 mg/l phenol in the media, which took a maximum time of about 194 hours. Comparing this result with our earlier batch degradation study [7] conducted in small-volume shake flasks (100 ml MSM), the time taken by the culture for complete degradation in batch stirred tank reactor was found to be much higher. The quantity of biomass (OD_{600}) produced was also less compared to the previous study. It should be mentioned here that in order to do a fair comparison

between the two modes of study (shake flasks and batch reactor), no attempt was made to control the main environmental parameter, the pH of the media, though it was continuously monitored. Although the same amount of inoculum (in %) and temperature were

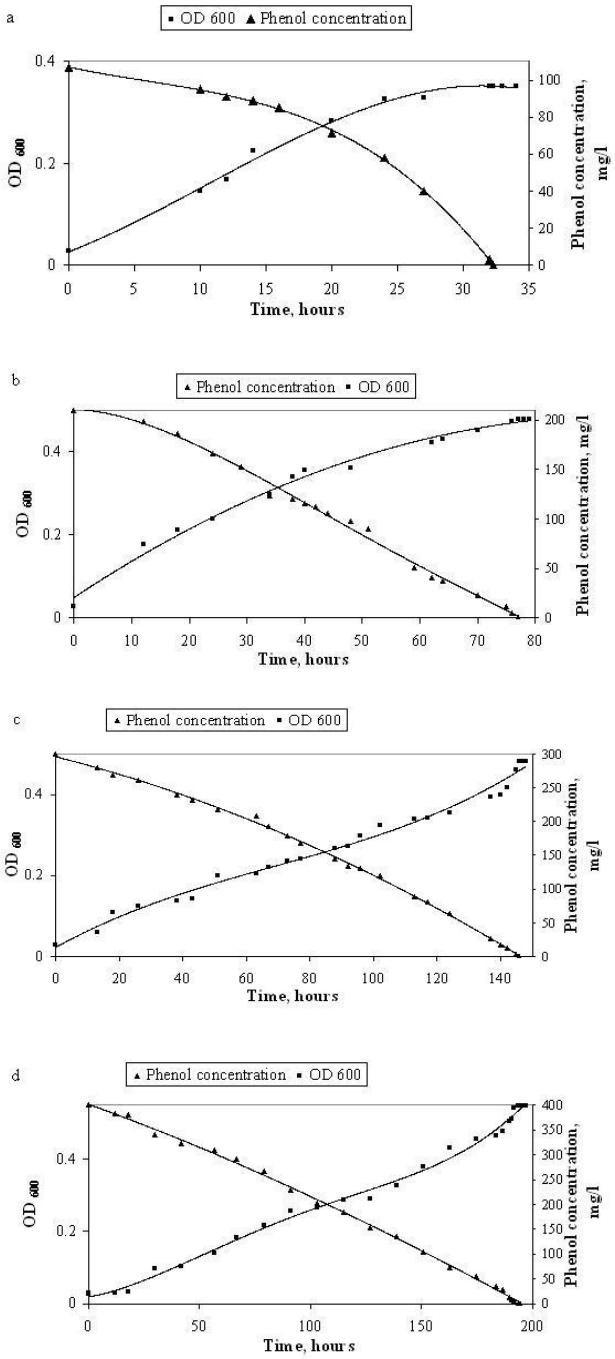

Fig. 2. Time profiles of biomass output (OD_{600}) and phenol degradation at different initial phenol concentrations: (a) 100 mg/l, (b) 200 mg/l, (c) 300 mg/l and (d) 400 mg/l.

maintained in the two studies, the time taken in this scaled up study was considerably higher than in the previous shake flasks study. This large difference in time could have been probably avoided by improving contact between the substrate and the microbes and/or by proper aeration of the system [5]. But this aspect needs further investigations to confirm.

Phenol has a significant inhibitory effect on the growth of microorganisms at its higher initial concentration [4, 5]. Therefore, acclimatization of the mixed culture, isolated from the sewage treatment plant, was carried out by allowing it to grow in presence of phenol as the sole carbon source. Maximum concentration of phenol, used for the above purpose, was 800 mg/l. Initially glucose was fed during acclimatization stage to boost up the initial growth of biomass; however the culture was grown only in presence of phenol in the later stage. From Fig. 2 (a-d) showing biomass concentration (OD_{600}) of the mixed culture at different initial concentrations of phenol, it was observed that phenol concentrations between 100 and 300 mg/l have no inhibitory effect on the microorganisms, as indicated by the nearly lacking lag phase. However, the maximum absorbance of the culture obtained at these phenol concentrations was found to be lower, as compared to that grown at a phenol concentration of 400 mg/l. Moreover, within this concentration range (100 - 300 mg/l), a stationary phase was reached and the time taken for this occurrence depended upon the initial concentration of phenol in the media. For example, at an initial phenol concentration of 300 mg/l the time taken by the culture to reach stationary growth phase was higher than that at lower initial concentrations of phenol. As regards the culture growth at 400 mg/l of phenol, the inhibition was found to be distinct and the culture took much longer time for its growth (maximum 194 h). However, the amount of biomass (OD_{600}) produced at this concentration was high, indicating that the mixed culture was capable of utilizing phenol very efficiently. From the findings on the biomass (OD_{600}) output at different times for various initial phenol concentrations, it is quite reasonable to state that both phenol and biomass amounts corresponded nearly well with each other indicating that phenol was well utilized in the process [4, 5].

3.2 Kinetics of culture growth and phenol degradation

To test the kinetics of phenol degradation by the mixed culture, the time profile of degradation, at all initial concentrations of phenol, was applied to growth associated and non-growth associated kinetic models, which are used to describe degradation of organics by microorganisms [8]. The

different types of models and their validity, in relation to initial substrate concentration, S_0, and half-saturation constant, K_s, are given in Table 1. Among the six different models tested, only the non-deterministic zero-order kinetic model could fit the data well with coefficient of determination (R^2) values greater than 0.97 at/above 200 mg/l initial phenol concentrations. However, for initial phenol concentration of 100 mg/l, the zero-order model fit

Table. 1. Kinetic models tested with the data on phenol degradation

	Model	Mathematical form	Valid for
Non-growth associated	Zero order	$S = S_0 - k_0 t$	$S_0 >> K_S$
	First order	$S = S_0 \exp(-k_1 t)$	$S_0 << K_S$
	Monod with no growth	$K_s \ln\frac{S}{S_0} + S - S_0 = -k_2 t$ $(k_2 = \mu_{max} X_0)$	$S_0 \sim K_S$
Growth associated	Logarithmic	$S = S_0 + X_0\left[1 - \exp(\mu_{max} t)\right]$	$S_0 >> K_S$
	Logistic	$S = \frac{S_0 + X_0}{1 + \frac{X_0}{S_0}[\exp(K(S_0 + X_0)t)]}$	$S_0 << K_S$
	Monod with growth	$K_s \ln\frac{S}{S_0} = (S_0 + X_0 + K_s)\ln\frac{X}{X_0} - (S_0 + X_0)\mu_{max} t$	$S_0 \sim K_S$

was slightly poorer as determined by its R^2 value of 0.79, which could be explained by the fact that the zero-order kinetic model is best valid for values of $S_0 >> K_S$; where K_S in this study, as presented later, was found to be ~40 mg/l.

All the other models gave a poor fit with R^2 values less than 0.5 at all initial concentrations of phenol. Although by fitting the zero-order kinetic model the culture proved complete degradation of phenol at/above these concentrations, a relationship between the rate of culture growth and phenol degradation could not be found. Therefore, in order to relate the pattern of phenol degradation with the culture growth in the system, the kinetics of these two phenomena were analyzed. This was achieved by calculating the specific growth rate (μ, h^{-1}) and specific substrate degradation rate (q, h^{-1}) from the biomass output and phenol degradation profiles, respectively, according to the following relationships:

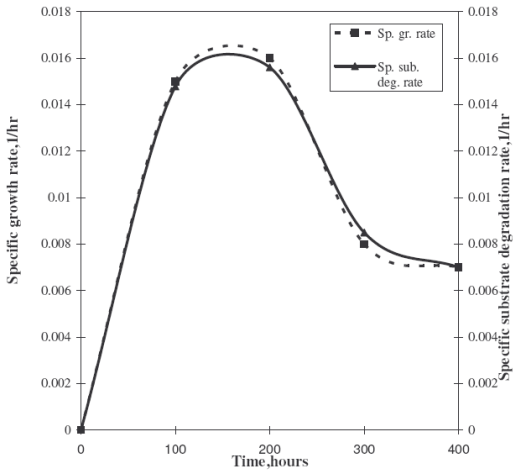

Fig. 3. Comparison of specific growth and specific substrate utilization rates at different initial phenol concentrations.

Specific growth rate:

$$\mu = \frac{1}{x}\frac{dx}{dt} \qquad (1)$$

Specific substrate degradation rate:

$$q = -\frac{1}{x}\frac{ds}{dt}, \qquad (2)$$

where x and s are the biomass and phenol concentrations in mg/l at a time, t in hours.

Table. 2. Models for substrate inhibition on growth rate of microorganisms

Model	Mathematical form	Reference
Haldane	$\mu = \frac{\mu_{\max} S}{K_s + S + \frac{S^2}{K_i}}$	Wang and Loh, [17]
Yano-Koga	$\mu = \frac{\mu_m}{(K_s / S) + 1 + \sum_{j=1}^{n} (S / K_j)^j}$	Yano and Koga [18]
Edward	$\mu_i = \mu_m \frac{S}{S + K_s + (S^2 / K_{si})(1 + S / K)}$	Mulchandani and Luong, [12]
Tseng-Wayman	$\mu = \mu_m \frac{S}{S + K_s}, S < S^*$	Tseng and Wayman [16]
Luong	$\mu = \frac{\mu_m S}{K_s + S}\left[1 - \frac{S}{S_m}\right]^n$	Luong [10]
Han-Levenspiel	$q = \frac{q_{\max} S\left[1 - \frac{S}{S_m}\right]^n}{K_s + S - \left[1 - \frac{s}{s_m}\right]^m}$	Han and Levenspiel [5]

Fig.3 illustrates a plot between the two rates calculated at different initial phenol concentrations in the media. This figure clearly indicates that both these rates correlate well with each other. However, the two rates declined after an initial rise thus revealing substrate inhibition characteristics in the system [9].

3.3 Modeling the kinetics of culture growth and phenol degradation

Because the rates of culture growth (μ) and phenol degradation (q) indicated substrate inhibition characteristics due to phenol, the variations of these two rates with respect to the phenol concentrations were modeled using suitable deterministic models, based on substrate inhibition on growth of microbial cultures, reported in the literature. These model equations are listed in Table 2 and a brief summary of each of these models is mentioned, as follows.

The earliest model on microbial growth kinetics, the Monod model, relates growth rate of microorganism to the concentration of a single growth controlling substrate as $\mu = f(s)$ via two parameters, maximum specific growth rate (μ_{max}) and half saturation constant (K_s), represented by the equation:

$$\mu = \frac{\mu_{\max} S}{K_S + S} \quad (3)$$

Since growth is a result of catabolic and anabolic enzymatic activities, these processes, i.e., substrate degradation or growth–associated product formation, can also be quantitatively described on the basis of Monod growth model [10]. But this model fails to explain substrate inhibition on either growth of microorganisms or substrate degradation. Haldane, cf. ref. [17], proposed the first and most popular model for substrate inhibition kinetics. This model was utilized by most of the researchers for growth inhibiting substrates like phenols and phenolics. Meric *et al.* [11] and Yano&Koga [12] models are based on a theoretical study on the dynamic behavior of single vessel continuous

fermentation subject to growth inhibition at high concentration of rate limiting substrate, *e.g.*, acetic acid fermentation from ethanol, gluconic acid fermentation from glucose, tannase fermentation with tannic acid as the sole carbon source, bacterium production from pentane, etc. The model resembles the Monod kinetic model with a slight modification [12].

Edward, cf. ref. [12] proposed a kinetic model, which is a modification of the Haldane model. After extensive evaluation he found that this model didn't show better results when compared to Haldane model and moreover, the value of the parameter K was very large [13].

Tseng&Wayman [14] in their model described substrate inhibition kinetics by accounting for the fact that below a threshold substrate concentration, S*, there is no growth inhibition. However, for concentrations above S*, microbial growth decreased linearly with respect to the concentration (S - S*) [13]. However, the discontinuous nature of the model is a major drawback. Luong [15] model, which appeared to be useful for representing the kinetics of substrate inhibition, is of generalized Monod type but accounts for substrate stimulation at its both, low and high, concentrations. The model has the capability to predict the values of S_m, the maximum substrate concentration, above which the growth is completely inhibited [15]. Mulchandani&Luong [13] stated that description of the microbial growth by the Haldane model did not prove that a similar mechanism is operative in the microbial growth. They particularly stressed on the importance of critical and maximum substrate concentrations [13]. Han&Levenspiel [16] proposed a model to express substrate degradation rate. This model involves a delay function, which has an exponential form and incorporates the critical product or substrate concentration corresponding to the inflection point on the growth [16].

The substrate inhibitions model equations were solved by the nonlinear regression method using MATLAB® 7.0 and were applied directly on the experimental data on specific growth rate of the mixed culture at different phenol concentrations. For applying the models to predict the specific substrate degradation rates, the term μ was replaced with q and then solved, as before. The fitness of these models in predicting the specific growth and specific substrate degradation rates is depicted in Figs. 4 and 5 respectively. From the figures, it could be seen that except the Tseng - Wayman model, all other models fit the data very well. The biokinetic constants of growth of the culture obtained from these models along with Root Mean Square (RMS) error between experimental and

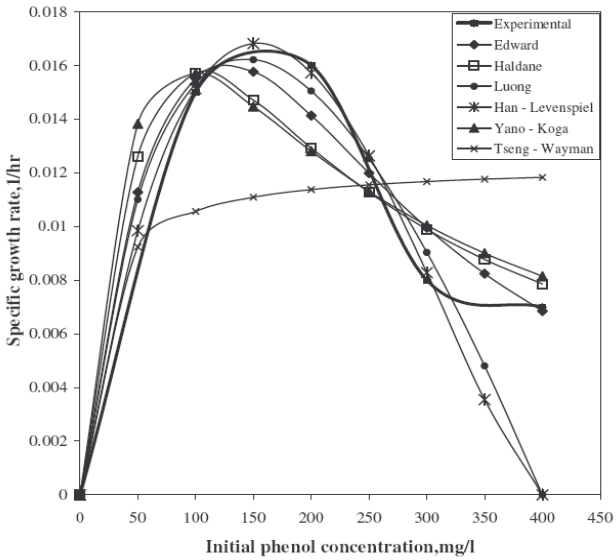

Fig. 4. Experimental and predicted specific growth rate of the culture according to the different models.

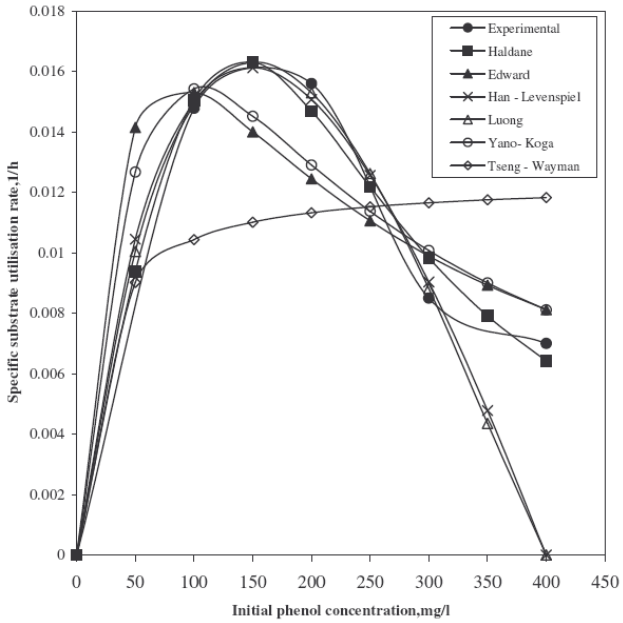

Fig. 5. Experimental and predicted specific substrate degradation rate obtained by applying different substrate inhibition models.

predicted values are shown in Table 3. These values of the constants obtained from the different models, but with the same set of experimental data, agree quite closely with each other except in case of the Tseng – Wayman model, which did not fit properly (RMS error $>70\times10^{-5}$). Edward, Haldane and Yano-Koga models predicted the substrate inhibition

Table. 3. Biokinetic constants estimated by fitting the various substrate inhibition models on the data on growth rate of the culture

Model	μ_{max} (h^{-1})	K_s(mg dm^{-1})	K_i(mg dm^{-1})	S_m(mg dm^{-1})	n	m	K	RMS error ($\times 10^{-5}$)
Edward	0.0290	63.77	100.00	-	-	-	6	1.15
Haldane	0.0324	40.57	140.65	-	-	-		1.86
Luong	0.0238	46.67	-	400	2.1	-		5.24
Han-Levenspiel	0.0257	40.55	-	400	0.6	1		5.62
Yano - Koga	0.0358	47.78	-	-	1	-	125	1.79
Tseng - Wayman	0.0123	16.74	-	-	-	-		77.70

constant (K_i) value, above which the specific growth and substrate degradation rates decline, more accurately and correlated well with the experimentally obtained value of 200 mg/l. Luong and Han - Levenspiel models also predicted the critical substrate concentration (S_m), at which critical growth rates fall to zero, to be ~ 400 mg/l, but this value was observed to be different from that obtained in the experiments. Similar observations on the specific substrate degradation rate were found to be valid for its biokinetic constants estimated from the models by applying the data on specific degradation rates, as well. Overall, the different models, despite their differences in background of origin, could well predict the behaviour of the system and the values of biokinetic constants obtained using these models revealed a fairly high potential of the microorganism in degrading phenol in a simple batch stirred tank reactor such as that used in this study.

4. CONCLUSIONS

The kinetics of phenol degradation was studied using a mixed microbial culture, isolated from a sewage treatment plant, in a simple stirred tank reactor operated under batch mode. The kinetics of phenol degradation was best explained by a non growth associated zero-order model with a maximum coefficient of determination value of >0.99 at 400 mg/l initial concentration of phenol in the media. The culture specific growth and phenol specific degradation rates correlated well with each other at all initial phenol concentrations. In the concentration range studied, phenol was found to exhibit substrate inhibition characteristics on these two rates, at 200 mg/l. The values of the biokinetic constants estimated from the models showed a good potential of the mixed microbial culture in treating phenol containing wastewaters using simple stirred tank reactors operated under batch mode.

NOTATIONS

k_0, k_1	zero, first order rate constants
K	positive constant in Yano – Koga
K	constant in Edward model
K_s	half saturation coefficient (mg dm^{-1})
K_i, K_{si}	substrate inhibition constants (mg dm^{-1})
m, n	empirical constants
q	specific substrate degradation rate (h^{-1})
q_{max}	maximum specific substrate degradation rate (h^{-1})
S	substrate concentration (mg dm^{-1}) at time t
S^*	substrate concentration (mg dm^{-1}) at which specific growth rate is maximum
S_0	substrate concentration (mg dm^{-3}) at time t=0
S_m	critical inhibitor concentration (mg dm^{-1}) above which the reactions stops
t	time (h)
x	biomass concentration (mg dm^{-1}) at time t
X_0	biomass concentration (mg dm^{-1}) at t=0
μ	specific growth rate (h^{-1})
μ_{max}	maximum specific growth rate (h^{-1})

REFERENCES

1. M. Latkar, K Swaminathan, T. Chakrabarti, *Bioresource Technol*., **88**, 69 (2003).
2. M. Kulkarni, A. Chaudhari, *Bioresource Technol*., **97**, 982 (2006).
3. T. Abuhamed, E. Bayraktar, T. Mehmetoğlu, U. Mehmetoğlu, *Process Biochem*., **39**, 983 (2004).
4. A. Kumar, S. Kumar, S. Kumar, *Biochem. Eng. J*., **22**, 151 (2005).
5. G.V. Rodriguez, C.B. Youssef, J.W. Vilanova, *Chem. Eng. J*., **117**, 245 (2006).
6. N. Nuhoglu, B. Yalcin, Process Biochem., **40**, 1233 (2005).
7. P. Saravanan, K., Pakshirajan, P. Saha, *Bioresource Technol*., **99**, 205 (2008).

8. M. Alexander, "Biodegradation and bioremediation". Academic Press, United Kingdom (1999).
9. S.J. Wang, K.C. Loh, *Enzyme Microb. Technol.*, **25**, 177 (1999).
10. K.K. Kovari, T. Elgi, *Microbiology&Molecular Biology Reviews*, **62**, 646 (1998).
11. S. Meric, O., Tunay, H.A. Alisan, *Environ. Technol*. **23**, 163 (2002).
12. T. Yano, S. Koga, *Biotechnol. Bioeng*., **11**, 139 (1969).
13. A. Mulchandani, J.H.T. Luong, *Enzyme Microb. Technol.* **11**, 66 (1989).
14. M.M. Tseng, M. Wayman, *Canad. J. Microbiol*., **21**, 994 (1975).
15. J.H.T. Luong, *Biotechnol. Bioeng*., **29**, 242 (1987).
16. K. Han, O. Levenspiel, *Biotechnol. Bioeng*., **32**, 430 (1998).

КИНЕТИКА НА РАЗЛАГАНЕ НА ФЕНОЛ И РАСТЕЖ НА ПРЕОБЛАДАВАЩИ ВИДОВЕ PSEUDOMONAS В ОБИКНОВЕН РЕАКТОР С ПЕРИОДИЧНО РАЗБЪРКВАНЕ

П. Сараванан[1*], К. Пакшираджан[2], П. Саха[3]

[1] *Катедра по строително инженерство , Университет Малая, Куала Лумпур – 50603, Малайзия*
[2] *Катедра по инженерна химия, Индийски технологичен институт Гувахати, Гувахати – 781039, Индия*
[3] *Катедра по биотехнологии, Индийски технологичен институт Гувахати, Гувахати – 781039, Индия*

Получена на 8 август 2010; приета на 21 февруари 2011

(Резюме)

Култура, съдържаща предимно видове *Pseudomonas,* изолирана от завод за третиране на канални води, се използува за изследване на кинетиката на разлагане на фенол и растеж на културата. Културата е способна да разложи фенол с максимална начална концентрация до 400 mg/l в обикновен реакторен съд с периодично разбъркване. Максималното време, необходимо за разлагане на фенол с такова концентрационно ниво, беше 194 h. Кинетиката на разлагане на фенола при различна начална концентрация в средата показва предимно скорост от нулев порядък с максимална стойност на коефициента на определеност (R^2) = 0.99 при 400 mg/l фенол. Детерминистични модели като тези на Халдейн, Хан-Левеншпиел, Луонг, Едуърд, Яно и Кога, Ценг и Уейман са използвани за описание на данните за инхибиране от субстрата в зависимост от кинетиката на растеж на културата и разлагане на фенола. Всички изпробвани модели описват добре експерименталните данни с изключение на модела на Ценг и Уейман.

Bulgarian Chemical Communications, Volume 43, Number 4 (pp 510 – 515) 2011

Study on thermal stability of composite mixtures on the base of wood ash

M.K. Mladenov*, E.S. Serafimova, Y.G. Pelovski

University of Chemical Technology and Metallurgy, Centre of Ecology, 1756 Sofia, 8, St. Kl. Ohridski blvd.

Received September 4, 2010; Accepted December 8, 2010

The results from thermogravimetric and differential thermal analysis (TG-DTA) of nine composite mixtures, based on ash from burning of wood biomass, green lye from pulp production and ammonium sulphate ($(NH_4)_2SO_4$) – by-product from cleaning of industrial waste gases, are presented. The content of different nutrients and the alkaline reaction of ashes are premise for their use as soil improvers. It is found that oxidation destruction and other reactions take place during the treatment and transformation of some compounds in the primary raw materials. The chemical reactions permit to assess the mixture behaviour in soil systems that refers to nutrients assimilation through the plants roots.

The determined temperature intervals for the transformation of the studied mixtures show that up to 70 ^oC no gaseous components are released by the nutrients and the studied products are relatively stable. The temperature intervals of the destruction processes occurring by oxidation or dehydration of the mixture components are determined. It is specified that destruction processes take place at higher temperatures, which could be achieved in the soil systems only after incidents with some chemicals or risk situations like fires.

Keywords: wood ash, composite mixtures, thermogravimetric and differential thermal analysis (TG-DTA), waste, soil improver

1. INTRODUCTION

The generation of solid and liquid wastes during thermal, mechanical-biological or physicochemical treatment of different raw materials or wastes, which include biodegradable components, specify the necessity to search for possibilities for their utilization as a secondary raw material or appropriate components for soils conditioners, with the aim to improve soils characteristics and productivity. Different methods and technologies for treatment and use of wastes from thermal processes of vegetable mass are proposed in some publications of Mladenov *et al.* [1], Artiaga-Diaz [2], Li [3], Soares and Menezes [4], [5], Petkova and Pelovski [6]. Brown [7] has used TG-DTA techniques to study the thermal stability and decomposition processes of some wastes.

In the present work the results of the TG-DTA investigations of composite mixtures based on wood ash, green lye and ammonium sulphate are presented.

2. EXPERIMENTAL

Research object are nine composite mixtures, obtained in quantities of 1 kg each, in presence of different contents of wood ash (WA) and green lye (GL). The wood ash contains: moisture – 0.40 %; organic substance (dry substance) ~ 0.37 %; nutrient elements (in the dry substance) - 0.032 % N, 0.72 % P_2O_5, 2.19 % K_2O, 48.7 % CaO, 1.3 % MgO; heavy metals (in the dry substance) - 2.79 mg/kg Cd, 88.5 mg/kg Pb, 22.45 mg/kg Cr, 17.35 mg/100g Ni, 154 mg/100g Cu, 201.5 mg/kg Zn, 11.25 mg/kg As; others (in the dry substance): 81.5 mg/100g Cl, 500-1000 mg/100g SO_4 and 30 - 300 mg/100g Na. Green lye contains: 5-6 % of organic mass, 17-18 % of active calcium and magnesium oxide, 15-16 % of other oxides. In the latter six mixtures different quantities of ammonium sulphate (AS) were added to compensate for the alkaline character of wood ash. The content of elements in ammonium sulphate used is presented in Mladenov *et al.* [1]. The content of different components in the obtained mixtures is shown in Table 1. All components are previously mixed by mechanical treatment for achieving the needed homogeneity.

Apparatus "MOM", 1500 D is used for the experiments. The apparatus is working in dynamic heating regime. The studies are performed in the temperature interval from 20 to 1 000 ^oC, with a heating rate of 10 ^oC/min. The range of the mass

*To whom all correspondence should be sent:
e-mail address: mladenov@uctm.edu.

Table 1. Components content in the obtained mixtures

№	WA, g	WA, %	GL, g	GL, %	AS, g	AS, %
S–1	500	50	500	50	0	0
S–2	550	55	450	45	0	0
S–3	600	60	400	40	0	0
S–4	300	30	400	40	300	30
S–5	450	45	350	35	200	20
S–6	500	50	400	40	100	10
S–7	350	35	300	30	350	35
S–8	500	50	250	25	250	25
S–9	550	55	200	20	250	25

balance is 500 mg, and the sensitivities of the recording device are – 500 μV for the TG curve, 500 μV for the DTG curve and 250 μV for the DTA curve. α-Al_2O_3 (Merck, Darmstadt, Germany) is used like as reference material. The sample mass is 500 mg.

RESULTS AND DISCUSSION

The obtained TG-DTA relationships are presented on Figs. 1-9, and the main results derived from them are given in Table 2.

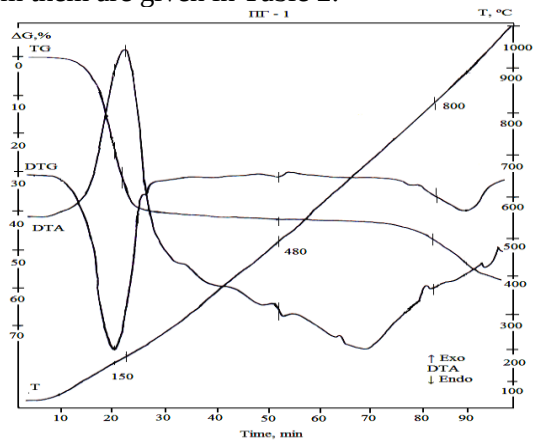

Fig. 1. Derivatogram of mixture S-1.

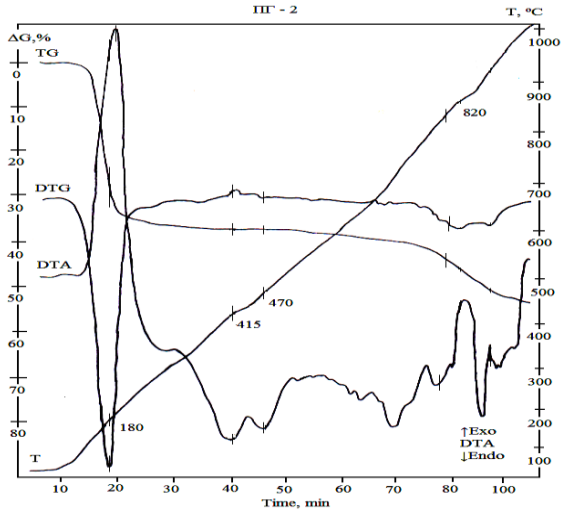

Fig. 2. Derivatogram of mixture S-2.

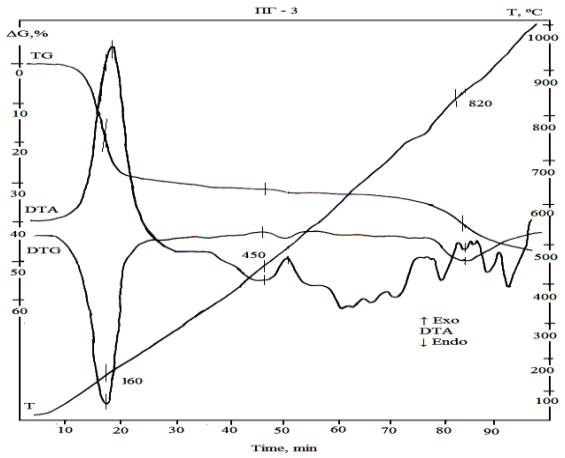

Fig. 3. Derivatogram of mixture S-3

For the mixtures with wood ash and green lye (Figs. 1-3) two main temperature intervals of mass losses are representative – from 45 to 280 °C, where the mass losses are 29.9-30 % and from 790 to 860 °C, where the losses are 2-5 %. The thermogravimetric dependences for the initial temperature interval are typical for auto-accelerating processes, at which mass losses decrease for a lower content of the green lye in the mixtures. The exothermic character of the thermal effect in this temperature interval shows that the mass losses are mainly related with oxidation and generation of gas emission from the organic components in the green lye. Higher mass losses at higher temperatures are registered. Mass losses increase in the same way when the ash content is higher, due to the dehydration and decarbonisation mainly of calcium compounds in the mixtures. This is also confirmed by the registered endothermic effects at the higher temperatures. The range of mass losses in the whole studied temperature range is from 41 to 46 %. The highest total mass losses are registered when the content of green lye in the products is 50 %.

As it is demonstrated on Figs. 4-9, adding of a third component to the system (10-35 % of ammonium sulphate) makes possible the interaction with other components from the mixtures, changing the rate and the character of the processes. The products with the highest content of ammonium sulphate (30-35 %) and green lye (30-40 %) determine the higher level of mass losses and control the rate of thermal decomposition processes. Both the increased content of ammonium sulphate (30-35 %) and the comparatively high content of green lye (30-40 %) show that in such cases no decarbonisation process (Figs. 4 and 7) takes place in the temperature range from 790 to

Table 2. Mass losses at different temperature stages and total mass loses for the studied mixtures.

Mixture	Oxidation of organic component			Dehydration of gypsum and calcium hydro-oxide			Decarbonisation of calcium carbonate			Total mass loses	
	Temperature range, °C	*Inflection point, °C*	*Mass loses, %*	*Temperature range, °C*	*Inflection point, °C*	*Mass loses, %*	*Temperature range, °C*	*Inflection point, °C*	*Mass loses, %*	*Temperature range, °C*	*Mass loses, %*
S-1	50 – 220	150	39.0	470 – 500	480	1.0	790 – 820	800	2.0	20 – 1 000	56.0
S-2	45 – 280	180	36.0	375 – 450 450 – 525	415 470	1.0 0.5	795 – 860	820	3.8	20 – 1 000	53.5
S-3	40 – 220	160	29.9	385 – 480	450	2.0	810 – 850	820	5.0	20 – 1 000	47.8
S-4	50 – 210	160	40.9	450 – 475	460	1.0	755 – 780 780 – 810	770 790	0.5 1.5	20 – 1 000	52.5
S-5	80 – 215	110	28.0	400 – 520	460	1.5	835 – 870	850	4.0	20 – 1 000	44.0
S-6	50 – 170	130	30.4	not detected			730 – 880	800	9.0	20 – 1 000	49.0
S-7	50 – 169	150	22.5	270 – 350	310	3.5	800 – 830	820	2.5	20 – 1 000	41.0
S-8	27 – 180	120	24.5	not detected			700 – 840 845 – 890	760 870	4.5 2.1	20 – 1 000	45.8
S-9	100 – 170	120	11.0	not detected			780 – 860 865 – 910	795 880	6.0 1.5	20 – 1 000	36.7

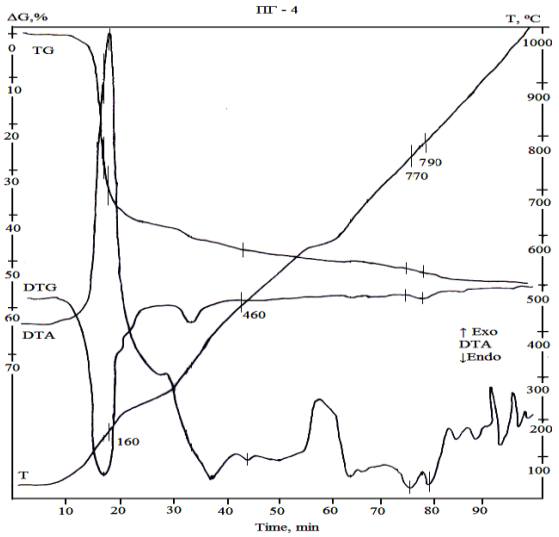

Fig. 4. Derivatogram of mixture S-4

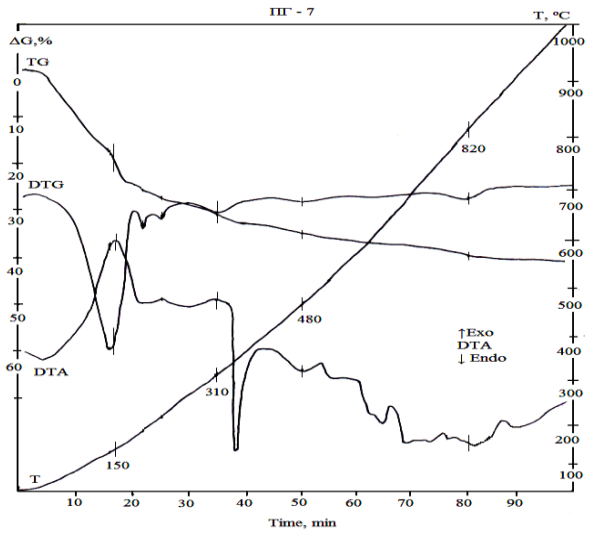

Fig. 7. Derivatogram of mixture S-7.

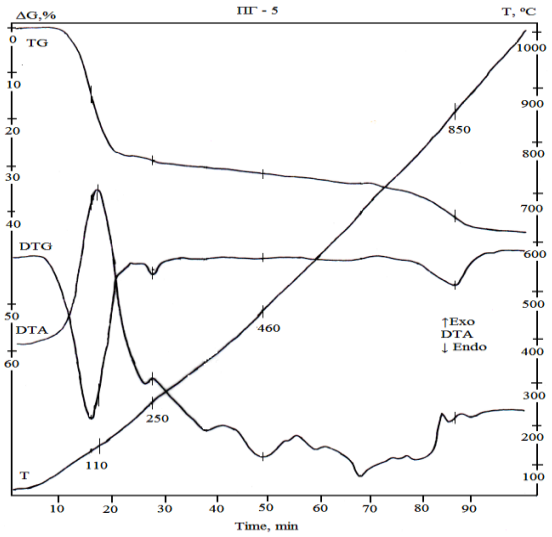

Fig. 5. Derivatogram of mixture S-5.

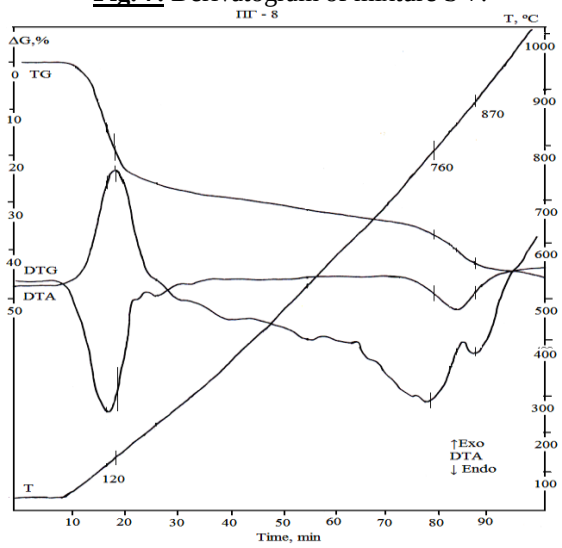

Fig. 8. Derivatogram of mixture S-8.

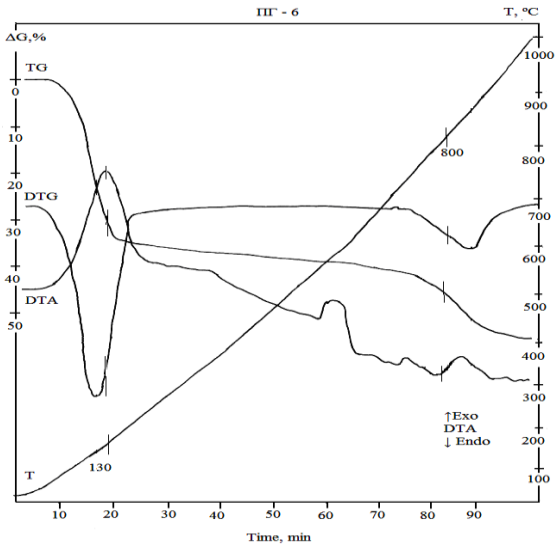

Fig. 6. Derivatogram of mixture S-6.

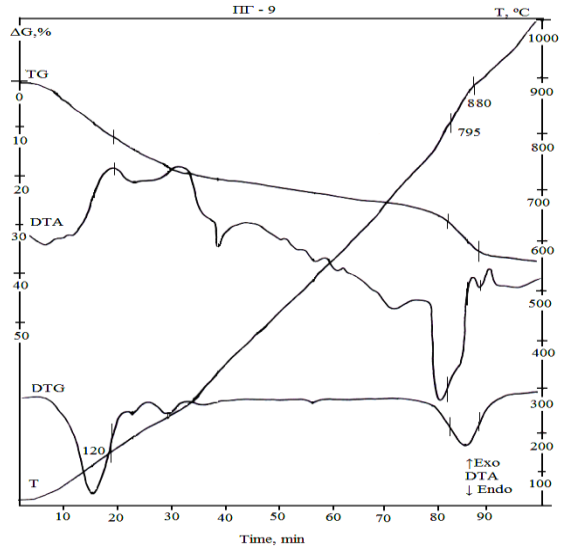

Fig. 9. Derivatogram of mixture S-9

860°C. This may be explained with an exchange reaction during the mixing process between ammonium sulphate and calcium compounds (hydroxide and carbonate).

All products obtained from wood ash, green lye and ammonium sulphate display a typical exothermic process in the temperature interval from 45 to 220 °C. Higher contents of ammonium sulphate and green lye accelerate the decomposition process and increase the mass losses in this temperature range up to 40.9 % for mixture S-4. Decreasing the content of ammonium sulphate to 25 % and green lye to 20 % (Fig. 9) controls mass losses during this stage in the same temperature range and determines lower mass losses – about 11 %. The same relationship is observed for the total mass losses of the mixtures. The total mass losses for mixture S-4 are 52.5 % and for mixture S-9 – 36.7 %.

The main data from TG-DTA studies are presented in Table 2. The weight ratio between the used components controls the temperature range of the reactions taking place and the released gas emissions by the oxidation of organic components in the green lye. Obviously, this is in accordance with the possibility for exchange reactions between ammonium sulphate and calcium compounds in the wood ash, starting with the mixing process.

The TG-DTA studies confirm that during thermal treatment different transformations may take place, changing the phase content of the solid products and releasing gas emissions. The weight ratio between the components in the studied system controls the rate of transformations and the level of enthalpies changes in the system. That allows determining the optimal ratio between the used components with a view to obtain products with desired thermal stability and physicochemical properties as soil improvers.

The obtained data from the investigations done with products from different mixtures and the relationships found permit to determine the main reactions taking place at different stages of the treatments made. The obtained results are in good agreement with the available literature data of Petkova and Pelovski [6], Dweck *et al*. [8], Vedalakshmi *et al*. [9] and Madarasz *et al*. [10]. The main chemical reactions expected during homogenization of the components and investigation of the thermal stability of the products are as follows:

1. Chemical reactions during homogenization:

$CaO + H_2O \Leftrightarrow Ca(OH)_2$

$CaO + (NH_4)_2SO_4 + H_2O \Leftrightarrow CaSO_4.2H_2O + NH_3 \uparrow$

$CaCO_3 + (NH_4)_2SO_4 + H_2O \Leftrightarrow CaSO_4.2H_2O + (NH_4)_2CO_3$

2. Chemical reactions during thermal treatment:

$R\text{-}COOH + O_2 \Leftrightarrow CO_2 + H_2O$

$CaSO_4.2H_2O \Leftrightarrow CaSO_4 + 2H_2O$

$(NH_4)_2SO_4 \Leftrightarrow NH_4HSO_4 + NH_3$

$Ca(OH)_2 \Leftrightarrow CaO + H_2O$

$CaCO_3 \Leftrightarrow CaO + CO_2$

Because of the impurities in the initial components we can not state that the given reactions represent all possible chemical reactions taking place during the processes studied.

CONCLUSIONS

The TG-DTA studies revealed that in temperature range 45 – 260 °C enthalpy and mass losses determine the exothermic oxidation of the organic components coming from the green lye and releasing water vapour and carbon dioxide emissions in the gas phase. At temperatures about 460 °C the processes of dehydration of gypsum and calcium hydro-oxide are completed; in the temperature range 700-910 °C decarbonisation of calcium carbonate takes place. On the base of the results obtained it could be stated that the products are suitable for use in agriculture as soil improvers.

Acknowledgements: *The authors would like to thank the Science and Research Programme (SRC) of UCTM – Sofia for the financial support (Contracts № 10 703/01.02.10 and 10828/ 11.02.2011).*

REFERENCES

1. M. Mladenov, Ek. Serafimova, Y. Pelovski, *J. Environ. Prot. Ecol.*, in press;
2. R. Artiga-Diaz, *J. Therm. Anal. Cal.*, **80,** 457 (2005);
3. R. Li, *Waste Management*, **27,** 1383 (2007);
4. R.W. Soares, V. J. Menezes, *J. Therm. Anal. Cal.*, **49**, 657 (1997);
5. Application of complex license to "Sviloza Plc" – city of Svishtov, Svishtov, April 2006 (in Bulgarian);
6. V. Petkova, Y. Pelovski, *J. Therm. Anal. Cal.*, **82**, 813 (2005);
7. M. Brown, Introduction to Thermal Analysis: techniques and applications, Chapman and Hill, 1988**;**
8. J. Dweck, P.M. Buchler, A.C. Coelho, F.K. Cartledge, *Thermochim. Acta*, **346**, 105 (2000);
9. R. Vedalakshmi, A.S. Raj, S. Srinivasan, K.G. Babu, *Thermochim. Acta*, **407**, 49 (2003);
10. J. Madarász, I.M. Szilágyi, F. Hange, G. Pokol, *J. Anal. Appl. Pyrolysis*, **72**, 197 (2004).

ИЗСЛЕДВАНЕ НА ТЕРМИЧНАТА СТАБИЛНОСТ НА КОМПОЗИТНИ СМЕСИ НА БАЗАТА НА ПЕПЕЛ ОТ ДЪРВЕСНА БИОМАСА

М. Младенов*, Ек. Серафимова, Й. Пеловски

Химикотехнологичен и металургичен университет, Център по екология, София 1756, бул. „Св. Климент Охридски", №8

Постъпила на 4 февруари, 2010 г.; одобрена на 8 декември, 2010 г.

(Резюме)

В настоящата статия са представени резултатите от проведения термогравиметричен и диференциален термичен анализ (ТГ-ДТА) на девет композитни смеси на основата на пепел от горене на дървесна биомаса, зелена луга от целулозно производство и амониев сулфат ($(NH_4)_2SO_4$) – страничен продукт от пречистване на отпадъчни индустриални газове. Съдържанието на различни хранителни елементи и алкалната реакция на пепелите са предпоставка за използването им като подобрители за почви. От проведените изследвания се установяват настъпващите процеси на окисление и деструкция на някои от компонентите в изходните суровини и дават възможност да се оцени тяхното поведение и трансформации в почвените системи, имащи отношение и към усвояването на хранителите елементи от кореновата система на отделните растителни видове.

Определените температурни интервали на трансформации в изследваните смеси показват, че до около 70 ^oC, от формулираните смеси не се генерират газови компоненти на хранителните елементи и не настъпват съществени изменения в структурата на органичните и неорганични компоненти на композитните смеси. Определени са температурните интервали на процесите на деструкция, изразени чрез окисление или дехидратация на отделни фази от композитните смеси. Установено е, че същите протичат при значително по-високи температурни интервали, които в почвените системи биха могли да бъдат постигнати при рискови ситуации на пожари или значимо химическо третиране.

Bulgarian Chemical Communications, Volume 43, Number 4 (pp 516–525) 2011

Spectroscopic and physical measurements on charge transfer complex of norfloxacin drug with iodine acceptor

M.S. Refat[a,b*], A. Elfalaky[c*], E. Elesh[d]

[a] *Department of Chemistry, Faculty of Science, Port Said University, Egypt*
[b] *Department of Chemistry, Faculty of Science, Taif University, 888 Taif, Kingdom Saudi Arabia*
[c] *Department of Physics, Faculty of Science, Zagazig University, Zagazig, Egypt*
[d] *Department of Physics, Faculty of Science, Port Said, Suez Canal,University, Egypt*

Received November 29, 2010; Revised March 15, 2011

The charge-transfer complex of the norfloxacin (nor) donor with iodine (I_2) acceptor has been studied spectrophotometrically in chloroform at room temperature using absorption spectrophotometer. The results pointed to the formation of CT complex. The stoichiometry of the complex was determined. The ratio method between donor and acceptor was found to be 1:1 by molar ratio method. The formation constant (K_{CT}), molar extinction coefficient (ε_{CT}), standard free energy (ΔG^o), oscillator strength (f), transition dipole moment (μ), resonance energy (R_N) and ionization potential (I_D) were estimated. IR, HNMR, mass spectra, UV-Vis techniques, elemental analyses (CHN) and TG-DTG/ DTA investigations were used to characterize the structure of charge-transfer complex. It was found that the CT interaction is associated with a proton migration from the donor to iodine followed by intermolecular hydrogen bond. In addition X-ray investigation was carried out to scrutinize the crystal structure of the complex.

Keywords: Norfloxacin, charge-transfer complexes, TG/DTG, IR, iodine.

1. INTRODUCTION

Norfloxacin (Formula I) is a synthetic chemo-therapeutic agent [1, 2] occasionally used to treat common as well as complicated urinary tract infections [3]. It is sold under various brand names with the most common being Noroxin. Norfloxacin is a second-generation synthetic fluoroquinolone (quinolone) developed by Kyorin Seiyaku .K.K. (Kyorin) [4].

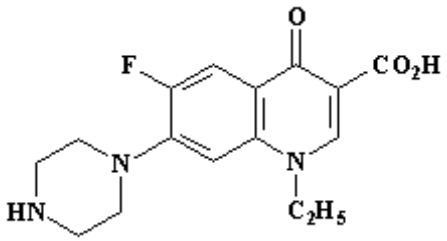

Formula I: Norfloxacin (nor)

Charge-transfer complexes are known to take part in many chemical reactions like addition, substitution and condensation [5, 6]. These complexes have drawn great attention for the production of non-linear optical materials and electrical conductors [7-10]. Electron donor-acceptor (EDA) interaction is also important in the field of drug-receptor binding mechanism [11], in solar energy storage [12] and in surface chemistry [13], as well as in many biological fields [14]. On the other hand, the EDA reactions of certain π- acceptors have successfully been applied in pharmaceutical analysis [15]. For such wide applications extensive studies on CT-complexes of π- acceptors have been performed [16]. Charge-transfer complexes of organic species are intensively studied because of their special type of interaction, accompanied by transfer of an electron from the donor to the acceptor [17, 18]. Also, protonation of the donor from acidic acceptors is generally root for the formation of ion pair adducts [19-21]. The solid charge-transfer complexes formed between iodine and several types of electron donors such as aromatic hydrocarbons, polycyclic amine, mixed oxygen/nitrogen cyclic bases, aromatic/aliphatic amines have been studied and categorized [22-30]. Some of charge-transfer complexes have very interesting applications in the analysis of some drugs in pure form or in pharmaceutical preparations [31, 32].

The charge-transfer reaction of (nor) with I_2 has not yet been reported in the literature; therefore the aim of the present study was directed to investigate these reactions. The results of the elemental analysis for the norfloxacin charge-transfer complex are listed in Table 1. From the table, it can be seen that values found are in agreement with the calculated

* To whom all correspondence should be sent:
E-mail: msrefat@yahoo.com

Table 1: Elemental analysis CHN and physical parameters data of the $[(nor)_2I^+].I_3^-$ CT-complex

Complexes	Mwt	C%		H%		N%		Physical data	
		Found	Calc.	Found	Calc.	Found	Calc.	Λm (μs)	mp (°C)
$[(nor)_2I^+].I_3^-$	1150	33.29	33.40	3.10	3.13	7.22	7.30	75	280

ones, and the composition of the CT-complex matches with the molar ratios obtained by photometric titration of (nor) and iodine σ-acceptors. This complex is insoluble in cold and hot water, but easily soluble in DMF and DMSO.

2. EXPERIMENTAL

Norfloxacin (MF= $C_{16}H_{18}FN_3O_3$), was of analytical reagent grade (Merck). The iodine acceptor was supplied from Aldrich. Stock solutions of norfloxacin or of iodine acceptor were freshly prepared and spectroscopic grade that used as received.

3.1. Synthesis of norfloxacin/iodine complex

The solid CT complex of (nor) with iodine was prepared by mixing (0.319 g, 1.0 mmol) of the donor in chloroform (10 ml), adding a solution of iodine (0.254 g, 1.0 mmol) in the same solvent (10 ml) and continuously stirring for about 4 h at room temperature. An orange yellow solid was isolated and the solution was allowed to evaporate slowly at room temperature. A solid complex was formed, washed several times with small amounts of chloroform, and dried under vacuum over anhydrous calcium chloride. The empirical formula of the complex $[(Nor)_2I]^+.I_3^-$ is $C_{32}H_{36}F_2N_6O_6I_4$ with molecular weight 1150 g/mol.

3.2.Instrumentation and physical measurements

3.2.1. Crystal structure.

Structural investigations were performed utilizing X-ray diffraction on a PHILIPS X-Pert Diffractometer, with Ni filter and CuKα radiation (λ = 1.5419).

3.2.2. Electronic spectra

The electronic spectra of the donors, acceptors and the resulting CT complexes were recorded in the region of 200-800 nm on a Jenway 6405 spectrophotometer with quartz cells, 1.0 cm path in length.

3.2.3. Infrared spectra

IR measurements (KBr discs) of the solid donors, acceptors and CT complexes were carried out on a Bruker FT-IR spectrophotometer (400-4000 cm^{-1}).

3.2.4. ^{1}H-NMR spectra

^{1}H-NMR spectra were obtained on a Varian Gemini 200 MHz spectrometer. ^{1}H-NMR data are expressed in parts per million (ppm), referenced internally to the residual proton impurity in DMSO solvent and the reported chemical shift, (m = multiplet, s = singlet and br = broad).

3.2.5. Mass spectra

The compositions of the complexes were confirmed from mass spectra at 70 eV taken on an AEI MS 30 mass spectrometer.

3.2.5. Thermal analysis

The thermal analysis (TGA/DTG/DTA) was carried in nitrogen atmosphere with a heating rate of 10ºC/min using a Shimadzu TGA-50H thermal analyzer.

4. RESULTS AND DISCUSSION

4.1. X-ray examination

For investigating the crystal structure of the obtained complex powdered samples were X-ray examined. In Fig. 1 the diffraction pattern is displayed, which reveals that the samples were in polycrystalline form. For the lack of structural data about the investigated materials, the CMPR program was applied in order to index the diffraction pattern [33]. Best fit of the diffraction pattern was carried out to estimate the unit cell and lattice parameters of norfloxacin: monoclinic unit cell with volume and lattice parameters 415.75 A^2, a=11.6535 A, b= 4.6922 A, and c= 7.6034 A for α= 90º, β= 124.046º and γ= 90º. Space group and average grain size were found to be P 2_1/m 1 1 and 109 nm, respectively.

4.2. *Electronic absorption spectrum of SZ/iodine system*

The UV-Vis absorption spectrum of the iodine complex was measured in $CHCl_3$ solvent. The complex was formed by adding X ml of 5.0×10^{-4} M iodine (X = 0.25, 0.50, 0.75, 1.00, 1.50, 2.00, 2.50 and 3.00 ml) to 1.00 ml of 5.0×10^{-4} M of norfloxacin. The volume of the mixtures in each case was completed to 10 ml with the $CHCl_3$ solvent. In the reaction mixture the concentration of (nor) was

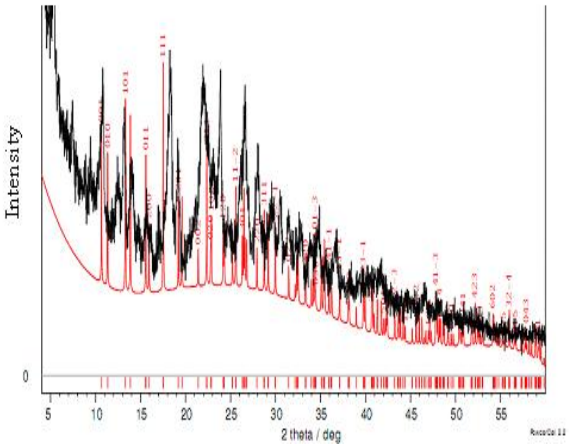

Fig. 1. X-ray diffraction pattern of norfloxacin with indexing.

kept fixed at 0.50×10^{-4} M, while the concentration of iodine was varied over the range from 0.125×10^{-4} M to 1.500×10^{-4} M. These concentrations produced (nor): I_2 ratios extending along the range from 1:0.25 to 1:3.00. Electronic absorption spectra of the 1:1 ratio in $CHCl_3$ together with the reactants I_2 and (nor) are shown in Figure 2.

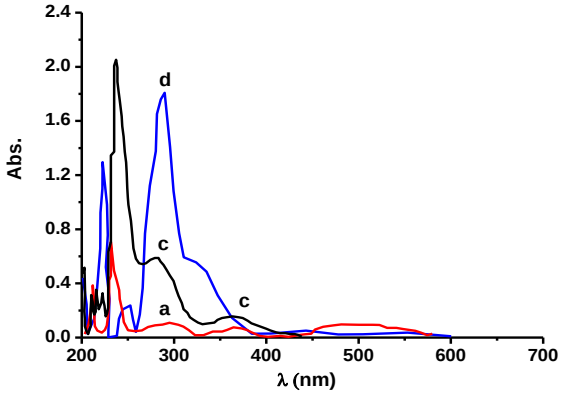

Fig. 2. Spectrum of electronic absorption of; norfloxacin-iodine reaction in $CHCl_3$, where (a) = acceptor (1.0×10^{-4}M), (c) = CT-complex and (d) = donor (1.0×10^{-4}M).

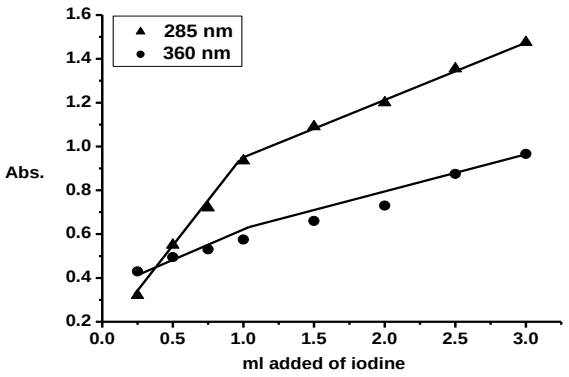

Fig. 3. Photometric titration curve for the norfloxacin-iodine system in $CHCl_3$ at 285 and 360 nm.

Characteristic absorption bands, which are not present in the spectra of the reactants free iodine and (nor), are shown in the spectra. These bands at about 360 and 290 nm were assigned to the CT-complex formed in the reaction. In other words, both (nor) and I_2 in the chloroform are not responsible for these bands. Table 2 gives the values of the absorbances obtained from photometric titrations based on the absorption bands at about 360 and 290 nm. Photometric titration curves based on these characteristic absorption bands are given in Figure 3. The photometric titration curve was obtained, according to the known methods, by plotting the absorbance against the ml added iodine σ-acceptor [33]. The equivalent points of this curve clearly indicate that the formed CT-complex between (nor) and iodine is 1:1. The formation of 1:1 complex was strongly supported by elemental analysis, mid-infrared, ^{1}H-NMR, mass spectra as well as by thermal analysis TG-DTG. However, the appearance of the two absorption bands around ≈ 360 and ≈ 290 nm is well known to be characteristic for the formation of the tri-iodide ion (I_3^-)[34-36]. Accordingly, the formed complex was formulated as $[nor_2I^+].I_3^-$.

Table 2. The electronic absorptions spectral data for nor-iodine CT-complex in $CHCl_3$ solvent (*1ml nor (5×10^{-4} M) + X ml iodine (5×10^{-4} M) + Y ml solvent = 10 ml*)

X ml of iodine	(nor : Iodine) ratio	Absorbance	
		285 nm	360 nm
0.25	1 : 0.25	0.32	0.43
0.50	1 : 0.50	0.55	0.49
0.75	1 : 0.75	0.72	0.53
1.00	1 : 1.00	0.94	0.57
1.50	1 : 1.50	1.09	0.66
2.00	1 : 2.00	1.20	0.73
2.50	1 : 2.50	1.36	0.88
3.00	1 : 3.00	1.48	0.97

It was of interest to study the effect of the solvent on the spectral intensities of the formed $[nor_2I^+].I_3^-$ complex. Calculations based upon the modified Benesi-Hildebrand equation, were executed for different (nor)-iodine ratios as follows [37]:

$$\frac{C_a^o C_d^o l}{A} = \frac{1}{K\varepsilon} + \frac{C_a^o + C_d^o}{\varepsilon} \qquad (1)$$

where C_a^o and C_d^o are the initial concentrations of the acceptor (I_2) and the norfloxacin donor, respectively. A is the absorbance of the definite bands at about 360 and 290 nm. Data for C_d^o of nor and C_a^o of (I_2), ($C_a^o + C_d^o$) and ($C_a^o . C_d^o$/A) in

Table 3. The values C_d^o, C_a^o, $C_d^o+C_a^o$ and $C_d^o.C_a^o/A$, for the nor-iodine system in $CHCl_3$ solvent

nor: Iodine ratio	C_d^o $\times10^{-4}$	C_a^o $\times10^{-4}$	$(C_d^o+C_a^o)$ $\times10^{-6}$	$(C_d^o.C_a^o) \times10^{-8}$	$(C_d^o.C_a^o/A)$ $\times10^{-10}$	
					285 nm	360 nm
1 : 0.25	0.5	0.125	62.50	0.0625	0.19	0.14
1 : 0.50	0.5	0.250	75.00	0.1250	0.23	0.25
1 : 0.75	0.5	0.375	87.50	0.1875	0.26	0.35
1 : 1.00	0.5	0.500	100.0	0.2500	0.27	0.43
1 : 1.50	0.5	0.750	125.0	0.3750	0.34	0.57
1 : 2.00	0.5	1.000	150.0	0.5000	0.42	0.68
1 : 2.50	0.5	1.250	175.0	0.6250	0.46	0.71
1 : 3.00	0.5	1.500	200.0	0.7500	0.51	0.78

Table 4. Spectrophotometric results of the $[(nor)_2I^+].I_3$ complex in $CHCl_3$ solvent at 25°C

λ_{max} (nm)	E_{CT} (eV)	K ($l.mol^{-1}$)	ε_{max} ($l.mol^{-1}.cm^{-1}$)	f *10^3	μ*10^3	I_p	D	R_N	ΔG^o(25°C) $KJmol^{-1}$
360	3.45	7.0*10^4	220*10^4	0.02	0.40	10.00	4.70	0.980	27800

$CHCl_3$ solvent, are presented in Table 3. By plotting the $C_a^o.C_d^o/A$ values for each solvent against the corresponding $(C_a^o+C_d^o)$values, straight lines were obtained with a slope of 1/ε and intercept of 1/kε as shown in Figure 4 for the reaction in $CHCl_3$. The oscillator strength f was obtained from the approximate formula [38]:

$$f = (4.319 \times 10^{-9})\ \varepsilon_{max}\ .\ \nu_{1/2} \qquad (2)$$

where $\nu_{1/2}$ is the band-width at half-intensity in cm^{-1}. The oscillator strength values together with the corresponding dielectric constants, D, of the solvent used are given in Table 4. From the data in Table 4 several conclusions may be drawn:

i) The $[(nor)_2I^+].I_3^-$ complex displays high values of both the equilibrium constant (K) and the extinction coefficient (ε). Such high value of (K) reflects the high stability of the (nor)/iodine complex as a result of the expected high donation ability of norfloxacin. On the other hand, the high value of (ε) of the (nor)/iodine CT-complex agrees quite well with the existence of a tri-iodide ion, I_3^-, which is known to have a high absorptivity value [34-36].

ii) The values of the oscillator strength, f, increase with increasing the dielectric constant (D) of the solvent. The general mechanism for the formation of $[(nor)_2I^+].I_3^-$complex was proposed as follows:

$$2nor+I_2 \rightarrow [nor]_2I^+.I^-$$

$$[nor]_2I^+.\ I^- + I_2 \rightarrow [(nor)_2I^+].I_3^-$$

The formation of the $[nor]_2I^+.I^-$ reaction intermediate is analogous to the well known species $[(donor)I]^+.I^-$ formed in the reaction of iodine with many donors [39-40].

The transition dipole moment (μ) of the norfloxacin CT-complex, Table 4, was calculated from the following equation [41]:

$$\mu = 0.0958[\varepsilon_{max}\ \nu_{1/2}\ /\nu_{max}]^{1/2} \qquad (3)$$

The ionization potential (I_p) of the free (nor) donor was determined according to the CT band of the iodine complex using the following relationship [42-43]:

$$I_p\ (ev) = 5.76 + 1.53\times10^{-4}\ \ \nu_{CT} \qquad (4)$$

The charge-transfer energy E_{CT} of the $[(nor)_2I^+].I_3^-$ complex was calculated using the following eq. [41]:

$$E_{CT} = (h\nu_{CT}) = 1243.667 / \lambda_{CT}\ (nm) \qquad (5)$$

The molar extinction coefficient of the complex at the maximum of the CT absorption (ε_{max}) can be calculated according to Briegleb and Czekalla [44] as follows:

$$\varepsilon_{max} = 7.7 \times 10^{-4} / [h\nu_{CT}/ [R_N] - 3.5\ ] \qquad (6)$$

where λ_{CT} is the wavelength of the complexation band, R_N is the resonance energy (R_N), ν_{CT} is the frequency of the CT peak and R_N is the resonance energy of the complex in the ground state, which obviously is a contributing factor to the stability constant of the complex (a ground state property). The values of R_N for the $[(nor)_2I^+].I_3^-$complex under study are shown in Table 4. The standard free energy change of complexation (ΔG^o) was calculated from the association constants by the following equation [45]:

$$\Delta G^o = -\ 2.303\ RT \log K_{CT} \qquad (7)$$

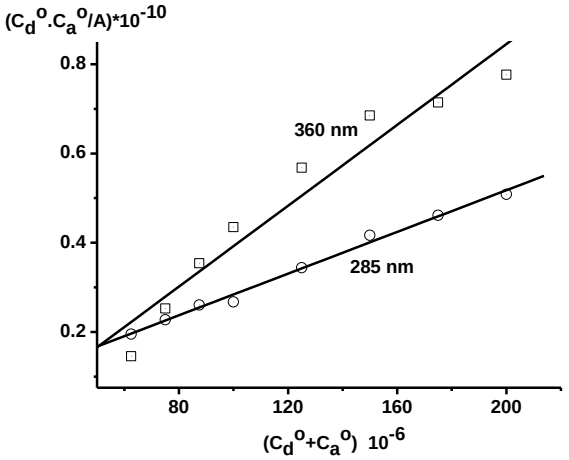

Fig. 4. The plot of (C_d^o+C_a^o) values against (C_d^o.C_a^o/A) values for the norfloxacin-iodine system in $CHCl_3$ at 360 and 285 nm.

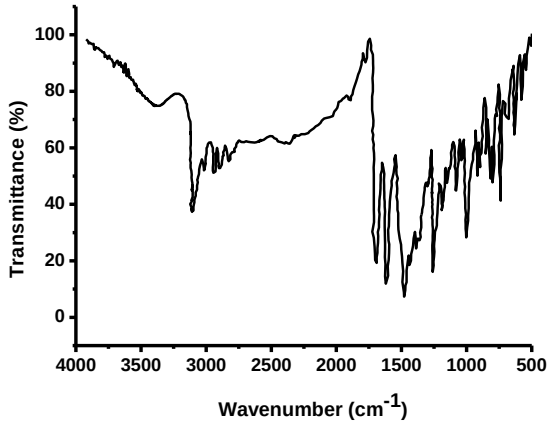

Fig. 5: Infrared spectra of $[(nor)_2I^+].I_3^-$ charge-transfer complex.

where ΔG^o is the free energy change of the complexes (KJ mol^{-1}), R is the gas constant (8.314 J mol^{-1} K), T is the temperature in Kelvin and K_{CT} is the association constant of the complexes (l mol^{-1}) in different solvents at room temperature. The values thus calculated are presented in Table 4.

4.3. *Infrared spectra of the $[(nor)_2I^+].I_3^-$*

The mid-infrared spectra of norfloxacin and the formed CT-complex, $[(nor)_2I^+].I_3^-$, were recorded from KBr discs. These spectra are shown in Figure 5. The spectral bands, assigned to their vibrational modes, are given in Table 5. As expected, the bands characteristic for the norfloxacin unit in the $[(nor)_2I^+].I_3^-$ CT-complex are displayed with small changes in band intensities and frequency values. For example, the ν(N-H) vibrations of -NH occur at 3400-3200 cm^{-1} for free (nor) due to ν_{as}(NH) and ν_s(NH), respectively. The hypsochromic effect (decreasing in the intensity) of ν(NH) vibrations in case of the iodine complex rather than in norfloxacin alone, as well as the presence of a new band at 3134 cm^{-1} with strong intensity point to the formation of a hydrogen bond. Such changes clearly indicate that the –NH group of the norfloxacin donor participates in the complexation process with iodine. On the other hand, the existence of a few bands at around 2700-2400 cm^{-1} (hydrogen bonding) in the $[(nor)_2I^+].I_3^-$ complex [46], strongly confirms the mode of interaction between (nor) and iodine through the hydrogen atom of –NH as (N-H---I).

The geometry of I_3^- in $[(SZ)_2]I^+.I_3^-$ may belong to one of the two structures: linear structure with ($D_{\infty h}$) symmetry and non-linear structure with (C_{2v}) symmetry. The linear I_3^- ion is shown in formula (II). It possesses an infinite rotation axis C_∞, an infinite number of C_2 axes, an infinite inversion axis S_∞, an infinite number of vertical planes $\infty\sigma_v$, a horizontal plane of symmetry σ_h, and a center of symmetry. The C_2 axes are perpendicular to C_∞, and thus it belongs to $D_{\infty h}$ symmetry.

I—I—I

(**II**)

The non-linear triiodide I_3^- ion formula (**III**) has two fold axis of symmetry, C_{2v}, and two σ_v planes of symmetry, thus it belongs to C_n, symmetry.

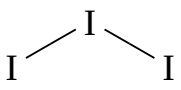

(**III**)

Accordingly, the number of vibrations (Γ_{vib}) for the non-linear I_3^- ion with C_{2v} symmetry is distributed as follows:

$$\Gamma_{vib} = 2A_1 \text{ (IR and R)} + B_2 \text{ (IR and R)}$$

where IR and R represent the infrared and Raman activities, respectively. Formula III describes the nature of these vibrational motions of the non-linear I_3^- ion with C_{2v} symmetry.

4.4. *^{1}H-NMR spectrum of $[(nor)_2I^+].I_3^-$ complex*

^{1}HNMR spectra of the (nor) free donor and the $[(nor)_2I^+].I_3^-$ CT-complex in DMSO at room temperature were measured. The chemical shifts

Table 5. Infrared frequencies[(a)] (cm^{-1}) and tentative assignments for norfoloxacin donor and $[(nor)_2I^+].I_3^-$ complex.

Nor	$[(nor)_2I^+].I_3^-$	Assignments
3399 ms	3421 w,br	ν(N-H) + ν(O-H)
3267 vw, 3228 vw 3189 vw,	3134 s, 3048 w	ν (C-H)
3130 vw 3021 w, 2927 m	2969 w, 2924w	ν (-$^+$N-H…I); hydrogen bond
	2856 w, 2662 w	
	2411 w, 2371 w	
1727 sh, 1716 ms	1705 vs	ν(C=O): (COOH)
1630 vs, 1552 w	1628 vs	ν(C=O) + $\delta_b(H_2O)$
		Phenyl breathing modes
1482 vs, 1454m 1396 s	1488 s, 1445 vw	CH; deformation of –CH_2–
	1396 w, 1373 w	
1307 vw	1308 w	$\delta_b(CH_2)$
1277 vw, 1263 s 1248 vw	1265 vs	ν(C-C)
1201 m	1197 m	ν(C-O)
1192 m		ν(C-N)
1153 vw, 1142 w 1132 w, 1115	1160 w, 1140 vw	$\delta_r(CH_2)$
w 1095 m, 1076 m	1086 ms, 1064 mw	
1051 vw, 1036 ms 1024 w, 1005	1008 s	
m		
982 m		
972 w, 935 ms	924 ms, 903 ms	CH- bend; phenyl
916 m, 899 m	857 ms, 823 ms	
887 m, 858 w	803 ms	
823 ms, 804 ms		
750 s, 706 m	750 s, 712 w	$\delta_b(COO^-)$
667 w, 631 w,br, 569 ms, 524 w	691 m, 643 ms	ring deformation
499 m, 474 m	590 ms, 558 w	
453 vw, 430 ms	521 vw, 496 ms	
	442 ms, 409 m	

(a): s = strong, w = weak, m = medium, sh = shoulder, v = very, br = broad; (b): ν, stretching; δ, bending.

(ppm) of proton NMR for the detected peaks were assigned and listed in Table 6. Evidently, the results obtained from elemental analysis, infrared spectra, and photometric titrations agreed with the ^{1}HNMR spectra to interpret the mode of interaction between donor and acceptor as follows:

i) In the $[(nor)_2I^+].I_3^-$ CT complex, the signal assigned to the H proton of -NH of norfloxacin at ~2.00 ppm was shifted upfield due to migration from donor to acceptor as –NH…I (formula IV).

ii) The shift of most signals in the $[(nor)_2I^+].I_3^-$ CT complex is due to the interaction between donor and acceptor. On the other hand, there is duplication in all bands due to the presence of two norfloxacin moieties.

4.5. Mass spectrum of $[(nor)_2I^+].I_3^-$ complex

Mass spectrometry was applied in order to study the main fragmentation routes of the$[(nor)_2I^+].I_3^-$ charge-transfer complex. Differences in fragmentation were caused by the nature of the attached acceptor through the intermolecular hydrogen bond between norfloxacin and iodine, while the observed peaks assigned to iodine and norfloxacin at *m/z* 128 (M+1) and 319 amu, were detected in the fragmentation of $[(nor)_2I^+].I_3^-$ CT-complex. The basic peak observed at *m/z*= 275 for $[(nor)_2I^+].I_3^-$ CT-complex was assigned to the loss of a COOH group. The intensities of these peaks give an idea of the stabilities of the fragments.

4.6. *Thermal analysis studies*

Norfloxacin melts at 232^{o}C with simultaneous decomposition [47]. The first mass loss was observed at 125 ^{o}C in the TG profile. The TG/DTG profiles of the ligand are shown in Figure 6A. From the TG curve it appears that the sample decomposes

Table 6: ^{1}HNMR spectral data of free nor and $[(nor)_2I^+].I_3^-$ complex

Nor	[(nor)2I+].I3$^-$	Assignments
1.13	1.218	δ H, -CH3
2.0	1.387, 1.419,	δ H, -NH; Piperazine
	1.453	
2.78, 3.10,	3.349, 3.532,	δ H, -CH2; Piperazine
3.47	4.591	δ H, -CH2; -CH2CH3
	4.626	
5.93, 7.12,	7.254, 7.219,	δ H, -CH aromatic
8.01	7.878	
	7.944, 8.809	
11.00	8.948	δ H, -COOH

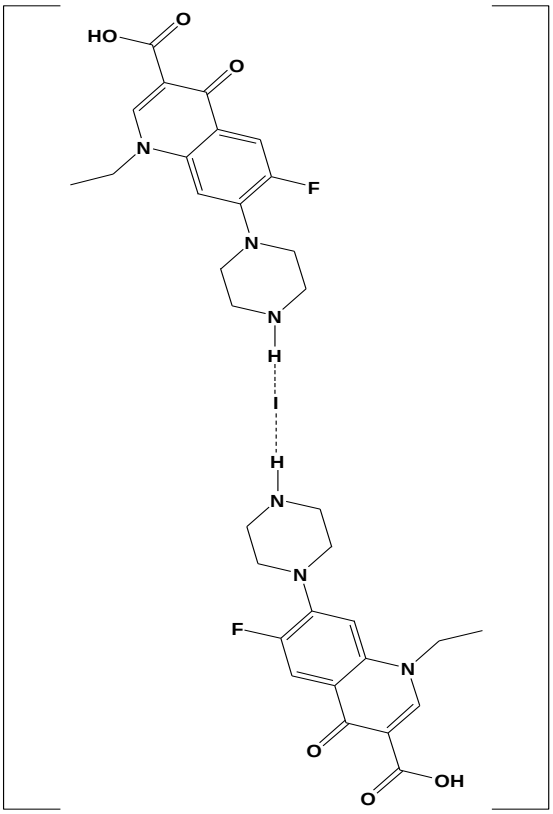

Formula IV: The structure of $[(nor)_2I^+].I_3^-$ CT complex

in three steps over the range 25-726 ^oC. The first decomposition step occurs between 25-270 ^oC with a mass loss of 8.38%; the second decomposition step starts at 270 ^oC and ends at 575 ^oC with a 69.80% mass loss. The next decomposition step occurs in the range 575-726 ^oC with a maximum at 650 ^oC and is accompanied by a weight loss of 19.56 %. Such a trend, which may be attributed to the loss of a pyrrole ring, ($2C_2H_2$+1/2N_2+1/2H_2), is in reasonable agreement with the theoretical value of 21.00 %.

In Figure 6B, the $[(nor)_2I^+].I_3^-$ CT-complex was thermally decomposed in four successive decomposition steps within the temperature range 25-800 ^oC. From Figure 6C (DTA curve), the decomposition steps located at 108, 217, 347 and 578 ^oC with experimental weight losses of 3.41, 19.66, 26.57 and 46.28%, respectively, were attributed to the liberation of two I_2 molecules and a $C_{25}H_{36}F_2N_6O_6$ organic moiety, with a contentious decomposition of the donor molecule to final residual carbons.

4.7. *Kinetic studies*

Three different methods were applied for the evaluation of the kinetic parameters as follows:

i) Freeman and Carroll (FC) differential method [48].

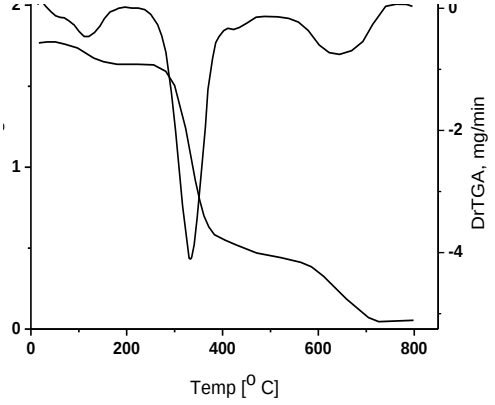

Fig. 6A. TG-DTG curve of norfloxacin free ligand.

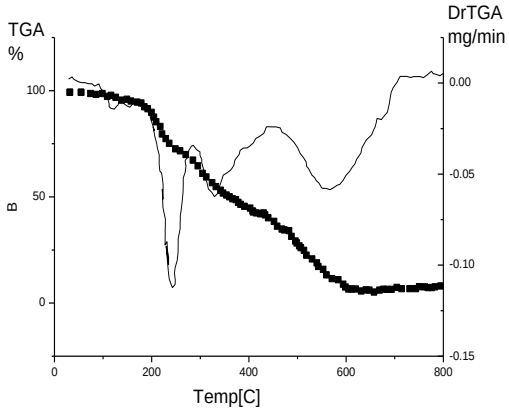

Fig. 6B. TG-DTG curve of $[(nor)_2I^+].I_3^-$ charge-transfer complex.

By combining the usual first-order equation with the Arrhenius equation, one gets:

$$\ln\left[\frac{dw/dt}{w_r}\right] = \ln Z - \frac{E}{RT}, \qquad (8)$$

where w is the total loss in weight up to time, t, $w_r = w_f - w$, w_f is the weight loss at the completion of the reaction, R is the gas constant and

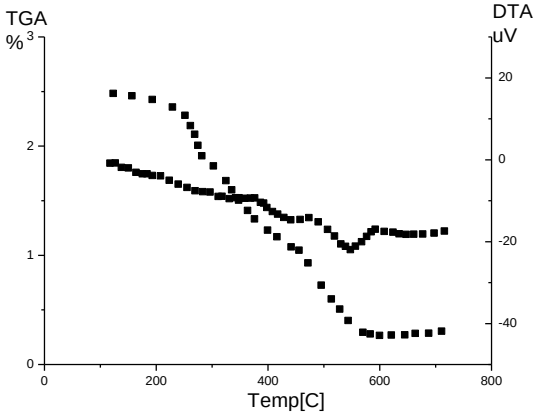

Fig. 6C. TG-DTA curve of $[(nor)_2I^+].I_3^-$ charge-transfer complex.

Table 7: Kinetic parameters of norfloxacin and $[(nor)_2I^+].I_3^-$CT-complex.
7a: nor

Method	n	Parameter					r
		E / kJmol^{-1}	Z / s^{-1}	ΔS / Jmol^{-1}K^{-1}	ΔH / kJmol^{-1}	ΔG / kJmol^{-1}	
HM	1	96.6	8.68*10^1	-37.9	93.3	108	0.9817
CR	1	93.6	2.00*10^1	-50.1	90.3	110	0.9853

7b: $[(nor)_2I^+].I_3^-$

Method	n	Parameter					r
		E / kJmol^{-1}	Z / s^{-1}	ΔS / Jmol^{-1}K^{-1}	ΔH / kJmol^{-1}	ΔG / kJmol^{-1}	
HM	1	137	7.93*10^4	-62.31	112	133	0.9932
CR	1	141	4.21*10^6	-70.33	130	141	0.9943

(dw/dt) is the weight-time gradient. A plot of $\ln\left[\frac{dw/dt}{w_r}\right]$ against 1/T was found to be linear. The energy of activation, E, was calculated from the slope while the pre-exponential factor, Z, was calculated from the intercept. The entropy of activation ΔS, was obtained from the following equation:

$$\Delta S = R\ln\left(\frac{Zh}{K_B T_m}\right) \qquad (9)$$

where K_B is the Boltzmann's constant, h is the Planck's constant and T_m is the DTG peak temperature.

ii) Horowitz and Metzger (HM) approximation method [49].

The following relation was derived [49]:

$$\ln\left[-\ln(1-\alpha)\right] = \frac{E}{RT_m}\Theta \qquad (10)$$

where α is the fraction of the sample decomposed at time t and $\Theta = T - T_m$.

A plot of $\ln\left[-\ln(1-\alpha)\right]$ against Θ was found to be straight line the slope of which is E, and Z can be deduced according to the relation:

$$Z = \frac{E\varphi}{RT_m^2}\exp\left(\frac{E}{RT_m}\right) \qquad (11)$$

where φ is the linear heating rate, the entropy of activation ΔS, was calculated using Equation (9). The order of reaction, n, can be calculated regarding the following relation [50]:

$$n = 33.64758 - 182.295\alpha_m + 435.9073\alpha_m^2 - 551.157\alpha_m^3 + 357.3703\alpha_m^4 - 93.4828\alpha_m^5 \quad \text{....(12)}$$

where α_m is the fraction of the substance decomposed at T_m.

iii) Coats and Redfern (CR) integral method [51].

For first-order reactions, the following equation of Coats-Redfern is fulfilled:

$$\ln\left[\frac{-\ln(1-\alpha)}{T^2}\right] = \ln\left(\frac{ZR}{\varphi E}\right) - \frac{E}{RT} \qquad (13)$$

A plot of $\ln\left[\frac{-\ln(1-\alpha)}{T^2}\right]$ against 1/T was found to be linear. From the slope E was calculated and Z can be deduced from the intercept. The enthalpy of activation, ΔH and the free enthalpy of activation, ΔG, can be calculated from the equations

$$\Delta H = E - RT_m \; ; \Delta G = \Delta H - T_m \Delta S \quad . \qquad (14)$$

The kinetic parameters evaluated using two of the above mentioned methods are listed in Table 7. The satisfactory values of the correlation coefficients (~1) in all cases indicate a good agreement with the experimental data. The values of the kinetic parameters are reasonable and in good agreement.

5. CONCLUSIONS

The crystal structure of Norfloxacin was recognized to be monoclinic with lattice constants a=11.6535 A, b= 4.6922 A, and c= 7.6034 A for α= 90°, β= 124.046° and γ= 90°. Space group and average grain size were found to be P 2_1/m 1 1 and 109 nm, respectively. The upfield shift in the NMR spectrum was attributed to the migration from donor to acceptor. Duplication in the NMR spectrum was ascribed to the existence of two Norfloxacin moieties. The disappearance of a COOH group was confirmed by the presence of a peak at m/z=275 in the mass spectrum. Kinetic parameters, such as E, z, ΔS, ΔH and ΔG were estimated.

REFERENCES

1. J.M. Nelson, T.M. Chiller, J.H. Powers, F.J. Angulo, *Clin. Infect. Dis*., **44**, 977 (2007).
2. E.N. Padeĭskaia, *Antibiot. Khimioter*., 48, 28 (2003).
3. V. Rafalsky, I. Andreeva, E. Rjabkova, Cochrane Database Syst. Rev.3:CD003597. doi:10.1002/14651858.CD003597.pub2.PMID 16856014 (2006).
4. http://www.faqs.org/rulings/rulings1999HQ545710.html.
5. E. M Kosower, *Prog. Phys. Org. Chem*., **3**, 81 (1965).
6. F.P. Fla, J. Palou, R. Valero, C.D. Hall, P. Speers, *JCS Perkin Trans*. **2**, 1925 (1991).
7. F. Yakuphanoglu, M. Arslan, *Opt. Mater*., **27**, 29 (2004).
8. F. Yakuphanoglu, M. Arslan, *Solid State Commun*., **132**, 229 (2004).
9. F. Yakuphanoglu, M. Arslan, M. Kucukislamoglu, M. Zengin, *Sol. Energy*, **79**, 96 (2005).
10. B. Chakraborty, A.S. Mukherjee, B.K. Seal, *Spectrochim. Acta* Part A, **57**, 223 (2001).
11. A. Korolkovas, Essentials of Medical Chem., 2nd Ed., Wiley, New York, 1998, Chapter 3.
12. K. Takahasi, K. Horino, T. Komura, K. Murata, *Bull. Chem. Soc. Jpn.*, **66**, 733 (1993).
13. S.M. Andrade, S.M.B. Costa, R. Pansu, *J. Colloid. Interf. Sci***., 226**, 260 (2000).
14. A.M. Slifkin, Charge-Transfer Interaction of Biomolecules, Academic Press, New York, 1971.
15. F. M. Abou Attia, *Farmaco*, **55**, 659 (2000).
16. K. Basavaiah, *Farmaco*, **59**, 315 (2004).
17. S.K. Das, G. Krishnamoorthy, S.K. Dofra, *Can. J. Chem.*, **78**, 191 (2000).
18. G. Jones, J.A.C. Jimenez, *Tetrahedron Lett*., **40**, 8551 (1999).
19. G. Smith, R.C. Bott, A.D. Rae, A.C. Willis, *Aust. J. Chem*., **53,** 531 (2000).
20. G. Smith, D.E. Lynch, R.C. *Bott*, *Aust. J. Chem*., **51,** 159 (1998).
21. G. Smith, D.E. Lynch, K.A. Byriel, C.H.L. Kennard, *J. Chem. Crystallogr*., **27,** 307 (1997).
22. P. Pal, T.N. Misra, *J. Phys. D: Appl. Phys*., **23,** 218 (1990).
23. C.D. Bryan, A.W. Cordes, R.C. Haddon, R.G. Hicks, R.T. Oakley, T.T.M. Palstra, A.S. Perel, S.R. Scottla, *Chem. Mater*., **6,** 508 (1994).
24. G.G. Roberts, D.G Thomas, *J. Phys. C: Solid State Phys.*, **7**, 2312 (1974).
25. H. Kusama, H. Sugihara, *Solar Energy Mat. & Solar Cells*, **90**, 953 (2006).
26. H.M.A. Salman, M.R. Mahmoud, M.H.M. Abou-El-Wafa, U.M. Rabie, R.H. Crabtree, *Inorg. Chem. Comm.*, **7**, 1209 (2004).
27. N.A. Al-Hashimi, *Spectrochim. Acta* Part A, **60**,, 2181 (2004).
28. Kh.A. Hassan, *Spectrochim. Acta* Part A, **60**, 3059 (2004).
29. L.I. Bebawy, N. El-Kousy, J.K. Suddik, M. Shokry, *J. Pharm. Biomedical Anal*., **21**, 133 (1999).
30. M.M. Ayad, *Spectrochim. Acta* Part A, **50**, 671 (1994).
31. G.A. Saleh, H.F. Askal, M.F. Radwan, M.A. Omar, *Talanta*, **54**, 1205 (2001).
32. H. Salem, J. Pharm. *Biomedical Anal*., **29**, 527 (2002).
33. D.A. Skoog, Principle of Instrumental Analysis, 3rd edn., Saunders College Publishing, New York, USA, 1985, Ch. 7.
34. W. Kiefer, H.J. Bernstein, *Chem. Phys. Lett*., **16**, 5 (1972).
35. L. Andrews, E.S. Prochaska, A. Loewenschuss, *Inorg. Chem*., **19**, 463 (1980).
36. K. Kaya, N. Mikami, Y. Udagawa, M. Ito, *Chem. Phys. Lett.*, **16**, 151 (1972).
37. R. Abu-Eittah, F. Al-Sugeir, *Can. J. Chem.*, **54,** 3705 (1976).
38. H. Tsubomura, R.P. Lang, *J. Am. Chem. Soc*., **86**, 3930 (1964).
39. M.S. Teleb and M. S. Refat, *Spectrochimica Acta* Part A, **60**, 1579 (2004).
40. E.M. Nour, S.M. Teleb, M.A.F. El-Mosallamy, M.S. Refat, *South Afr. J. Chem*., **56**, 10 (2003).
41. R. Rathone, S.V. Lindeman, J.K. Kochi, *J. Am. Chem. Soc*., **119**, 9393 (1997).
42. G. Aloisi, S. Pignataro, *J. Chem. Soc. Faraday Trans.* **69**, 534 (1972).
43. G. Briegleb, *Z. Angew. Chem*., **72,** 401 (1960); G. Briegleb, *Z. Angew. Chem*., **76**, 326 (1964).
44. G. Briegleb, J. Czekalla, Z. Physik. Chem. (Frankfurt), **24,** 237 (1960).
45. A.N. Martin, J. Swarbrick, A. Cammarata, Physical Pharmacy, 3rd ed., Lee and Febiger, (Philadelphia, PA 1969) p.344.
46. L.J. Bellamy, The infrared Spectra of Complex Molecules, Chapman & Hall, London, 1975.
47. M.S. Refat, *Spectrochim. Acta*, **68**, 1393 (2007).
48. E.S. Freeman and B. Carroll, *J. Phys. Chem*., **62**, 91 (1958).
49. H.H. Horowitz, G. Metzger, *Anal. Chem*., **35**, 1464 (1963).
50. H.A.Hashem, M.S. Refat, *Surf. Rev. Lett*, **13**, 439 (2006).
51. A.W. Coats, J.P. Redfern, *Nature*, **201**, 68 (1964)

СПЕКТРОСКОПСКИ И ФИЗИЧНИ ИЗМЕРВАНИЯ НА КОМПЛЕКС С ПРЕНОС НА ЗАРЯД НА МЕДИКАМЕНТА НОРФЛОКСАЦИН С ЙОДЕН АКЦЕПТОР

М.С. Рефат[a,b*], А. Елфалаки[c*], Е. Елеш[d]

[a] *Катедра по химия, Факултет по природни науки, Университет Порт Саид, Египет*
[b] *Катедра по химия, Факултет по природни науки, Университет Таиф, 888 Таиф, Саудитска Арабия*
[c] *Катедра по физика, Факултет по природни науки, Университет Загазиг, Загазиг, Египет*
[d] *Катедра по Физика, Факултет по природни науки, Университет Суецки Канал, Порт Саид, Египет*

Получена на 29 ноември 2010; Преработена на 15 март 2011

(Резюме)

Комплексът с пренос на заряд на норфлоксацин (нор) като донор с йоден (I_2) акцептор е изследван спектрофотометрично в хлороформ при стайна температура с абсорбционен спектрофотометър. Резултатите показват формиране на комплекс с пренос на заряд. Определена е стехиометрията на комплекса. Отношението между донор и акцептор е определен като 1:1 чрез метода на моларното отношение. Направена е оценка на константата на образуване (K_{CT}), моларния коефициент на екстинкция (ε_{CT}), стандартната свободна енергия (ΔG^o), силата на осцилатора (f), диполния момент на прехода (μ), енергията на резонанса (R_N) и потенциала на йонизация (I_D). Използвани са техниките с IR, HNMR, мас-спектри, UV-Vis, елементен анализ (CHN) и TG-DTG/ DTA изследвания за охарактеризиране на структурата на комплекса с пренос на заряд. Установено е, че взаимодействието с пренос на заряд е свързано с миграция на протон от донора към йода последвана от междумолекулна водородна връзка. В допълнение е проведено изследване с Рентгенови лъчи за изучаване на кристалната структура на комплекса.

Bulgarian Chemical Communications, Volume 43, Number 4 (pp 526 – 531) 2011

New cesium ion-selective PVC membrane electrode based on a novel calix[6]arene derivative

N. Aslan[a*], E. Canel[a], M. Yilmaz[b], E. Kiliç[a]

[a]*Department of Chemistry, Faculty of Science, Ankara University, Ankara, Turkey*
[b]*Department of Chemistry, Faculty of Arts and Sciences, Selçuk University, Konya, Turkey*

Received December 17, 2010; Accepted January 4, 2011

Cesium-selective polymeric membrane electrode, based on a recently synthesized calix[6]arene compound of 5,11,17,23,29,35-*tert*-butyl-37,39,41-trimethoxy-38,40,42-tricyanomethoxy-calix[6]arene, is described. The electrode exhibits a near Nernstian response for Cs (I) ions over a wide concentration range of 1.0×10^{-1} to 1.0×10^{-5} M with a slope of 55.3 ± 1.2 mV/p[Cs]. The developed electrode has a very short response time (4-5 s) and it can be used for at least 30 days without any considerable divergence in potentials. The proposed electrode shows high selectivity towards cesium (I) ions with respect to alkali, alkaline earth, several transition and heavy metal ions. The potentiometric response is independent of pH of the test solution in the pH range of 3.0-10.0. The electrode can be used as an indicator electrode in the potentiometric titrations of cesium (I) ions with sodium tetraphenylborate and for direct determination of cesium in tap water samples.

Keywords: PVC membrane; cesium; ion-selective electrode; calix[6]arene.

1. INTRODUCTION

In recent years, the development of novel sensors for the detection of various metal ions has been motivated by the control of the levels of environmental pollutants in natural waterways and potable water. Under normal conditions, cesium is not considered as a major contaminant of natural and groundwaters. It preferentially adheres to soils, thereby showing relatively low mobility. However, in the case of a nuclear reactor accident large amounts of radioactive cesium isotopes could be released into aquatic environments, which will be very dangerous for human health. That is why, the use of ion-selective electrodes (ISEs) for the detection of cesium has received much interest, and many ligands used as sensing molecules in new cesium ion-selective poly(vinyl chloride) (PVC) membrane electrodes have been reported [1-3].

Calix[*n*]arenes and their derivatives act as strong ligands, by selectively binding cations and small organic molecules (such as chloroform, toluene and fullerene). The presence of a cavity and of specific electron donor sites results in their ability to form stable host-guest systems with electron-acceptor molecules and that is why they are excellent complexing agents that are capable of binding alkali-metal cations [4]. In this respect, calixarenes have advantages over other classes of macrocyclic compounds as ionophores for poly(vinyl)chloride (PVC)-based ion-selective electrodes (ISEs) and ion-sensitive field effect transistors (ISFETs) [2-5]. Recently Cs-ISEs have seen increasing interest for clinical and environmental analysis. However, in comparison with sodium and potassium, only limited Cs-ISEs based on crown ethers and neutral ionophores have been reported [6-7]. In early studies about Cs-ISEs based on ion-exchangers, tetraphenylborate and its derivatives were reported [8]. Quadruply-bridged calix[6]arenes were first used as ionophores by Choi *et al*. Polymeric cesium ion-selective electrode exhibited high selectivity over alkali, alkaline earth and ammonium ions [9].

The purpose of this study was to develop a new cesium ion-selective electrode using the recently synthesized 5,11,17,23,29,35-*tert*-butyl-37,39,41-trimethoxy-38,40,42-tricyano-methoxy-calix[6]arene as a neutral carrier and to use this electrode for *in situ* determination of cesium ions in waste water. The lifetime, response time, optimum working range, and other response characteristics of the electrode were determined.

* To whom all correspondence should be sent:
E-mail: naslan70@gmail.com

2. EXPERIMENTAL

Reagents and solutions

5,11,17,23,29,35-*tert*-butyl-37,39,41-trimethoxy-38,40,42 - tricyanomethoxy – calyx [6] arene was synthesized at the Department of Organic Chemistry of Selçuk University by the procedures developed in ref. [10]. The structure of the ionophore studied in this work is shown in Fig.1. High-molecular-weight poly(vinylchloride) (PVC), 2-nitrophenyloctylether (2-NPOE), 2-nitrophenylpentylether (*2*-NPPE), tetrahydrofuran (THF) were obtained from Fluka as selectophores.

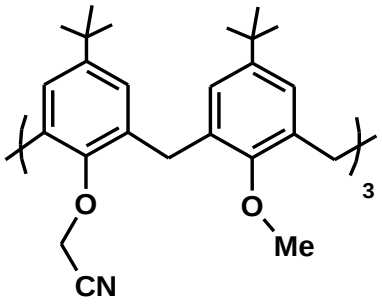

Fig. 1. 5,11,17,23,29,35-*tert*-butyl-37,39,41-trimethoxy-38,40,42-tricyanomethoxy-calix[6]arene.

Potassium tetrakis(*p*-chlorophenyl)borate (KTpClPB) and sodium tetraphenyl borate (NaTPB) as lipophilic anionic additives were obtained from Aldrich. Britton-Robinson (BR) buffer solutions (pH 2-12) were used to investigate the performance of the prepared cesium ion-selective electrode. All chemical substances were of reagent grade and were used without further purification. Metal solutions of different concentrations were made by dilution of 0.5 M stock solutions of each metal ion. Deionized water obtained from Human power I$^+$, Ultra Pure Water System was used throughout the experiments.

Membrane composition and electrode preparation

The Cs^+-selective electrode was constructed using a PVC-based membrane as reported previously [11-12]. The membrane was prepared by dissolving optimized amounts of PVC, plasticizer, liphophilic additives and ionophore in a ratio of 33.32: 64.86: 0.75: 1.06, respectively, in 5 mL of tetrahydrofuran. The mixture was shaken vigorously and the clear solution was poured onto a glass disc 3.5 cm in diameter. The solvent was allowed to evaporate at room temperature, until polymeric membrane was obtained. For preparation of the electrodes, 0.7 cm diameter disc of the polymer membrane was cut and fixed to the end of a glass tube with a diameter of 0.5 cm and a length of 10 cm. The tube was then filled with internal filling solution (1.0×10^{-3} M $CaCl_2$). The prepared PVC membrane electrode was conditioned for 24 h by soaking in 1.0×10^{-4} M CsCl solution. A silver/silver chloride electrode was used as an internal reference electrode.

Apparatus and potential measurements

Using the double-junction Ag/AgCl reference and the cesium-selective electrode the following electrochemical cells were prepared.

Reference//Analyte solution//Membrane//Inner filling solution/Ag,AgCl

The potential measurements were made by the use of Orion 720A Model pH ion meter. The reference electrode was a double-junction Ag/AgCl electrode (Orion 9002) and the pH measurements were done with an Ingold (10.402.3311) combined glass pH electrode. The performance of the proposed cesium-selective electrode was investigated by measuring the potential in Cs (I) solutions prepared in the concentration range of $1.0 \times 10^{-1} - 1.0 \times 10^{-6}$ M. The working solutions were stirred with a magnetic stirrer and the potentials were recorded after the equilibrium potentials had been reached.

3. RESULTS AND DISCUSSION

Ion selectivity

It is well known that the sensitivity and the selectivity of the ion-selective electrodes obtained for a given ionophore not only depend on the ion-binding properties of the ionophore but also significantly on the membrane ingredients as plasticizers, lipophilic additives and ratios of these ingredients in the membrane [13-14]. The former is an intrinsic property of the ionophore, while the membrane composition can be optimised experimentally. The literature survey showed that the usual range of composition in the preparation of PVC matrix membrane electrodes was 1–7% ionophore, 28–33% PVC (internal matrix), 60–69% plasticiser (solvent) and 0.03–2% lipophilic anion [15]. Since in preparation of many PVC membrane electrodes a plasticizer/PVC ratio (m/m) of nearly 2 has resulted in very suitable performance characteristics [16], this ratio was kept at about 2 in optimization of the ingredients of the cesium (I) ion-selective electrode proposed.

Effect of the anionic sites

The presence of lipophilic anionic sites in the cation-selective membrane electrode not only lowers ohmic resistance and significantly reduces response times and selectivity, but also enhances the sensitivity of the membrane electrode especially in case where the extraction capability of the ionophore is poor [15, 17]. Morover, lipophilic additives may catalyze the exchange kinetics at the membrane interface [18]. We prepared the electrode by using potassium tetrakis(*p*-chlorophenyl)borate (KT*p*ClPB) and sodium tetraphenylborate (NaTPB) as a lipophilic anion. The membrane containing sodium tetraphenylborate (NaTPB) did not show any response for cesium ions. This may be attributed to the fact that sodium ions form ion pairs with the tetraphenylborate that settle in the cavity of the calix[6]arene and decrease the number of active sites in the membrane.

Effect of the plasticizer

The influence of the plasticizer on the characteristics of the cesium ion-selective electrode was investigated. It is known that the nature of the solvent mediator influences the dielectric constant of the membrane phase, the mobility of the ionophore molecules and the state of the ligands. So, it plays an important role in determining the ISE characteristics [19]. In our study, in order to investigate the effect of the plasticizer on the characteristics of the proposed electrode, two sets of membranes of similar composition, but with different plasticizers (2-NPOE or *2*-NPPE) were prepared and tested. We observed only minor differences in the performance of the electrodes, however slightly better selectivity was obtained with 2-NPOE. That is why 2-NPOE was chosen for the further experiments.

Working range and slope of the electrode

Over the concentration range 10^{-1} – 10^{-5} M of cesium in the calibration solutions, the electrode potential response was linear (Fig. 2). The slope of the calibration curve was 55.3 ± 1.2 mV/pCs and the detection limit, calculated as recommended by IUPAC [20], was 4.36×10^{-6} M. The slope of the electrode was found to be close to the Nernstian value. Although the electrode does not give a full Nernstian response, it is stated in the literature that the electrodes with slopes in this vicinity range could be used for analytical applications [21, 22]. This range was found to be compatible with many PVC membrane electrodes mentioned in the literature [23 - 25].

Effect of pH on the response characteristics of the electrode

The influence of pH on the response of the Cs (I)-ion selective electrode with o-NPPE as the

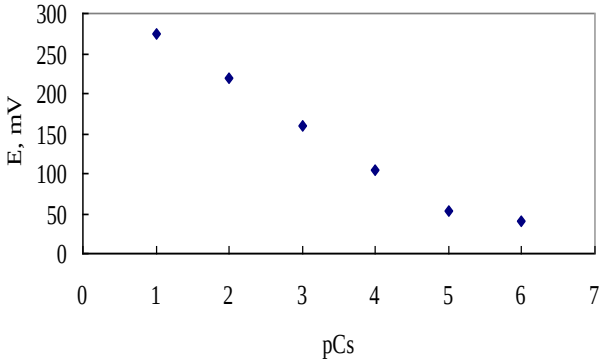

Fig.2. Calibration curve of the cesium ion-selective electrode based on 5,11,17,23,29,35-*tert*-butyl-37,39,41-trimethoxy-38,40,42-tricyanomethoxy-calix[6]arene

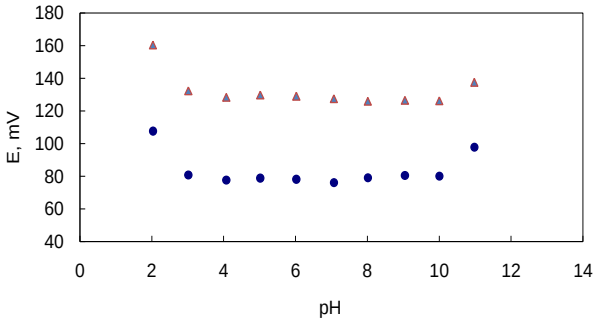

Fig.3. The effect of pH of test solutions containing a) 1.0×10^{-2} M (▲) and b) 1.0×10^{-3} M (●) cesium ions on the response of the Cs-selective electrode.

plasticizer was studied over the pH range 2 – 11 at 1.0×10^{-2} and 1.0×10^{-3} M Cs (I) containing solutions. We found that the response characteristics (response slope and linear working range) of the electrode did not change by changing the pH values of the solution in the range 3 – 10 (as illustrated in Fig. 3). This can be taken as the useful pH range over which the electrode can be used. All further measurements were made at pH 6.0.

The lifetime and the response time of the electrode

The lifetime of the electrode was determined by recording its potential at an optimum pH value and plotting its calibration curve for each day. No

significant change in the slope of the electrode was observed within one month, after which, a gradual decrease in the working concentration range, slope and response time of the electrode was registered. The response time and the lifetime of the proposed PVC membrane electrode is compatible with those of most similar electrodes reported in the literature [7, 21, 26]. The static response time was 4-5 s over the working ranges of the electrodes and no change was observed in 10 minutes.

Selectivity coefficients of the electrode

The selectivity coefficients for Cs (I) over a variety of interfering ions were determined by the fixed interference method, which is based on the Nicolsky-Eisenman equation recommended by IUPAC. In this work, the concentration of the cesium ion was varied in the concentration range $1.0 \times 10^{-1} - 1.0 \times 10^{-6}$ M, while that of the interfering ion was 1.0×10^{-3} M. It was observed that the proposed Cs (I)-selective electrode is highly selective with respect to a variety of other common cations (K^+, NH_4^+, Na^+, Li^+, Mg^{2+}, Ca^{2+}, Sr^{2+}, Ba^{2+},Zn^{2+}, Co^{2+}, Cd^{2+}, Ni^{2+}, Pb^{2+}). The values of the selectivity coefficients are listed in Table 1.

Table 1. Selectivity coefficients ($k^{pot}_{Cs,\ X}$) of the cesium(I) ion-selective electrode using fixed interference method

Interfering ions	Selectivity coefficients ($k_{Cs,X}$)	Interfering ions	Selectivity coefficients ($k_{Cs,X}$)
K^+	1.66×10^{-2}	Co^{2+}	3.16×10^{-4}
Li^+	1.00×10^{-2}	Cu^{2+}	3.16×10^{-4}
Na^+	1.58×10^{-2}	Cd^{2+}	1.66×10^{-2}
NH_4^+	7.38×10^{-3}	Ni^{2+}	3.16×10^{-4}
Mg^{2+}	3.16×10^{-4}	Pb^{2+}	4.91×10^{-4}
Ca^{2+}	4.46×10^{-4}	Sr^{2+}	4.37×10^{-4}
Zn^{2+}	3.16×10^{-4}		

The selectivity coefficients for some common interfering ions of the proposed calix[6]arene-based electrode are compatible with the corresponding values previously reported for PVC-membrane Cs (I)-selective electrodes based on different neutral ion carriers [4, 7, 10, 13, 23].

Analytical applications

The electrode was used in the titration of 25.0 mL 1.0×10^{-2} M cesium ions with 0.1000 M sodium tetraphenylborate. The titration curve was plotted and the concentration of cesium ions was determined in order to elucidate whether the prepared cesium ion-selective electrode can be employed as an indicator electrode. The titration curve is given in Fig. 4.

The proposed electrode was also applied to the determination of cesium ions in tap water. The water sample was analyzed without pH adjustment and filtering. The sample was divided into two equal parts and each part was spiked with an aliquot of a standard (1000 ppm) CsCl solution to give 5 and 10 ppm Cs^+, respectively. The cesium content in the sample was determined by direct potentiometric measurement. The tested samples

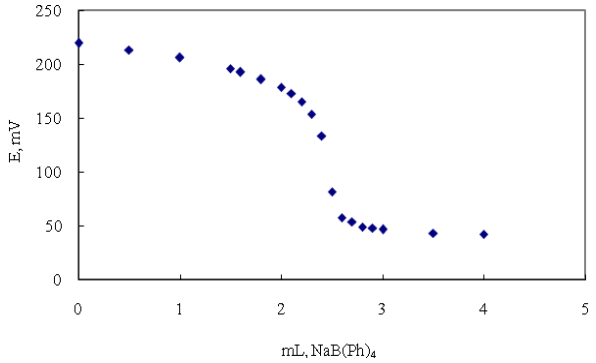

Fig.4. Potentiometric titration curve for 25 mL of 1.0×10^{-2} M Cs^+ solution with 0.1000 M $NaB(C_6H_5)_4$, using the proposed Cs(I)-ISE as an indicator electrode.

Table 2. Analysis of water samples spiked with cesium(I)

Sample No	[Cs] AES[a], ppm	[Cs] ISE[b], ppm	Recovery (%)
1	5.19 ± 0.02	5.03 ± 0.02	100.6
2	11.26 ± 0.12	11.43 ± 0.03	114.3

[a]Atomic emmission spectrometric method
[b]The developed Cs^+ ion-selective electrode

were also analyzed by atomic emission spectrometry to determine the reliability of the proposed electrode. As can be seen from Table 2, the results were found to be reliable at the 95% confidence level. Hence, the electrode prepared could be successfully employed in potentiometric titrations and direct potentiometric measurement of cesium ions.

4. CONCLUSIONS

Calix[6]arene can be successfully used as an ionophore in the cesium (I) ion-selective electrode. The prepared Cs^+ ion-selective electrode can be used to determine cesium ion concentrations in the range $1.0 \times 10^{-1} - 4.36 \times 10^{-6}$ M with a slope of 55.3 ± 1.2 mV/pCs. This electrode is very easy to prepare, shows high selectivity and sensitivity, wide dynamic range, and low detection limit. The

wide pH range (3-10), in which the electrode can be employed, is suitable for application in natural water samples without pH adjustment. It has a relatively fast response time (less than 4-5 seconds) and can be used for at least one month without any considerable divergence in potentials. Unlike most previously developed electrodes, for which there is no reported analytical application, e.g., [14,15], the electrode proposed in the present work is applied as a sensor for the determination of cesium ions concentration in tap water and the results show a good correlation with those obtained by atomic emission spectrometry. The electrode was also used as an indicator electrode in the potentiometric titration of cesium ions with sodium tetraphenylborate.

Acknowledgements: *We gratefully acknowledge the financial support of Ankara University Research Fund (Project No: 2002-07-05-068).*

REFERENCES

1. Y. Choi, H. Kim, J.K. Lee, S.H. Lee, H.B. Lim, J.S. Kim, *Talanta,* **64**, 975 (2004).
2. R.K. Mahajan, M. Kumar, (nee Bhalla)V. Sharma, I. Kaur, *Talanta*, **58**, 445 (2002).
3. L. Chen, H. Ju, X. Zeng, X. He, Z. Zhang, *Anal. Chim. Acta***, 437**, 41 (2001)**.**
4. P.L. Nostro, G. Capuzzi, E. Fratini, L. Dei, P. Baglioni, *Progress in Colloid and Polym. Sci.*, **118**, 238 (2001).
5. R. Berczki, B. Agai, I. Bitter, L. Toke, K, *J. Incl. Phenom. Macrocycl. Chem.*, **45**, 45 (2003).
6. M. Arvand-Barmchi, M.F. Mousavi, M.A. Zanjanchi, M. Shamsipur, S. Taghvaei, *Anal. Lett.*, **35**, 767 (2002).
7. M.B. Saleh, *Talanta,* **46**, 885 (1998).
8. E.W. Baumann, *Anal. Chem.*, **48,** 548 (1976).
9. E.M. Choi, H. Oh, S. Wang Ko, Y.K. Choi, K.C. Nam, S. Jeon, *Bull. Korean Chem. Soc.,* **22**, 1345 (2001).
10. G.U. Akkus, M. Yılmaz, *Polycycl. Aromat.Compd.* **22**, 1075 (2002).
11. D. Kuruoğlu, E. Canel, S. Memon, M. Yılmaz and E. Kılıç, *Anal. Sci.* **19**, 217 (2003).
12. S. Erden, A. Demirel, S. Memon, M. Yılmaz, E. Canel and E. Kılıç. *Sens. Actuators B* **113**, 290 (2006).
13. T. Rosatzin, E. Bakker, K. Suzuki, W. Simon, *Anal. Chim Acta* **280**, 197 (1993).
14. M.H. Mashhadizadeh, I. Sheikhshoaie, *Talanta* **60,** *73 (2003).*
15. Y.A. Zolotov, Macrocyclic Compounds in Analytical Chemistry. John Wiley and Sons, New York, p 1. (1997)
16. C. Hongbo, E.H. Hansen, J. Ruzicka, *Anal. Chim. Acta*, **169**, 209 (1985).
17. H.R. Pouretedal, A. Semnani, M.H. Keshavarz, *Turk. J. Chem.*, **30**, 711 (2006).
18. S.S.M. Hassan, W.H. Mahmud, A.H.M. Othman, *Talanta*, **44**, 1087 (1997).
19. E. Bakker, P. Buhlmann, E. Pretsch, *Chem. Rev.*, **97**, 2083 (1997).
20. IUPAC, *Pure Apply Chem.*, **48**, 27 (1976).
21. L. Ebdon, J. Braven, N.C. Frampton, *Analyst*, **115**, 189 (1990).
22. Y.K. Lee, J.T. Park, C.K Kim, *Anal. Chem.*, **58**, 2101 (1986).
23. A. Radu, S. Peper, C. Gonczy, W. Runde, D. Diamond, *Electroanalysis*, **18**, 1379 (2006).
24. M. Shamsipur, S.Y. Kazemi, H. Sharghi, K. Niknam, *Fresenius J. Anal. Chem.*, **371**, 1104 (2001).
25. A.A.M. Hassan, R.F. Aglan, S.A. El-Reefy, *Anal. Lett.*, **37**, 21 (2004).
26. D. Wang, J. Shang Shih, *Analyst*, **110**, 635 (1985).
27. C. Perez Jimenez, L. Escrichel, C. Casabo, *Anal. Chim. Acta*, **371,** 155 (1998).

НОВ СЕЛЕКТИВЕН КЪМ ЦЕЗИЕВ ЙОН МЕМБРАНЕН ЕЛЕКТРОД ОТ PVC НА ОСНОВАТА НА НОВПОЛУЧЕНО КАЛИКС[6]АРЕНОВО ПРОИЗВОДНО

Н. Аслан [a*], Е. Канел[a], М. Юлмаз[b], Е. Килич[a]

[a] *Катедра по химия, Факултет по природни науки, Университет Анкара, Анкара, Турция*

[b] *Катедра по химия, Факултет по изкуства и науки, Университет Селчук, Кония, Турция*

Получена на 11 декември 2010; Приета на 4 януари 2011

(Резюме)

Описан е цезий-селективен полимерен мембранен електрод, на основата на наскоро синтезирано каликс[6]ареново съединение 5,11,17,23,29,35-*терт*-бутил-37,39,41-триметокси-38,40,42-трицианометокси-каликс[6]арен. Електродът показва почти Нернстов отклик на йони Cs (I) при широк диапазон на концентрации от 1.0×10^{-1} до 1.0×10^{-5} M с ъглов коефициент 55.3 ± 1.2 mV/p[Cs]. Разработения електрод има много кратко време на отклик (4-5 s) и може да се използва поне 30 дни без някакво значимо отклонение на потенциалите. Предложеният електрод показва висока селективност към цезиевите (I) йони по отношение на йони на алкални, алкалоземни , някои преходни и тежки метали. Потенциометричният отклик не зависи от pH на опитния разтвор при изменение на pH от 3.0-10.0. Електродът може да се използва като индикаторен електрод при потенциометрично титруване на цезиеви (I) йони с натриев тетрафенилборат и за определяне на цезий в проби на водопроводна вода.

Bulgarian Chemical Communications, Volume 43, Number 4 (pp 532 – 537) 2011

The *in vitro* antioxidant and antibacterial activities of *Tanacetum pinnatum* boiss. grown in Iran

A. Esmaeili[1*] and H. Amiri[2]

[1]*Department of Chemical Engineering, North Tehran Branch, Islamic Azad University, Tehran, Iran*
[2] *Department of Biology, Lorestan University, Khoramabad, Iran.*

Received February 22, 2010; Revised July 5, 2010

This study was designed to examine the *in vitro* antioxidant and antibacterial activities of the aerial parts of *Tanacetum pinnatum* Boiss. GC and GC-MS analysis of the essential oil resulted in the identification of 25 compounds, representing 98.7% of the oil content. The main components in the oils were camphor (23.2%), *α*-pinene (8.5%), camphene (7.7%), 1,8-cineole (7.3%), *β*-eudesmol (5.8%) and caryophyllene oxide (5.6%). The possible antioxidant and antibacterial activity of the samples was studied using the DPPH and the *β*-carotene-linoleic acid assays and the disc agar diffusion test, respectively. In general, the nonpolar extract of *T. pinnatum* exhibited the greatest antioxidant activity in the DPPH test system. The essential oil displayed the highest antioxidant activity in the *β*-carotene-linoleic acid assay; it showed the best antibacterial activity against *Staphylococcus aureus.*

Keywords: *Tanacetum pinnatum*, antibacterial activity, camphor, *α*-pinene, antioxidant activity.

1. INTRODUCTION

The *Tanacetum* genus is represented in Iran's flora by 26 species including 12 endemics [1, 2]. Plants belonging to the *Tanacetum* genus are reputed to have excellent medicinal values, and a large number of sesquiterpenoids and sesquiterpene lactones, which are typical constituents of these drugs, have been isolated from *Tanacetum* species. These compounds might be partly or wholly responsible for the effect exhibited by the plants. Since the Middle Ages the plant *T. parthenium* has been used in the treatment of migraine, asthma, rheumatism and gynecological problems [3]. Previously, sesquiterpene lactones have been identified in the aerial parts of *T. polycephalum* [4]. The essential oil of *T. vulgare* has displayed antibacterial activity [5-7] and its sesquiterpene lactones [8] *T. pinnatum***,** *T. khorassanicum* and *T. fruticulosum* have been the subject of our previous studies [9-11]. Sesquiterpene lactones in *T. indicum* var. tuneful [12], and *T. argyrophyllum* [13], and terpenoid constituents in the oils of *T. cilicium*, *T. corymbosum* and *T. macrophyllum* have been reported. Anticoagulant and antifibrinolytic properties of these oils have also been reported [14-22]. Many applications, including food preservation, pharmaceuticals, alternative medicine and natural therapies, related to the antimicrobial and antioxidant activities of plant oils and extracts have been reported [23]. 25 components have been identified in the oil of *T. pinnatum*, in which camphor (23.2%), *α*-pinene (8.5%) and camphene (7.7%) were the main components [24]. The extract of *T. pinnatum* exhibited the greatest antioxidant activity in the DPPH test system. In the *β*-carotene-linoleic acid test system the highest antibacterial effect was displayed against *Staphylococcus aureus*.

2. EXPERIMENTAL

Plant Mmaterial

The samples of *T. pinnatum* were collected during the flowering stage from Khoramabad, Province of Lorestan, Iran, in June 2008. Voucher specimens were deposited at the Herbarium of the Research Center of Lorestan, Khoramabad, Iran.

Oil isolation

The aerial parts of *T. pinnatum* (200 g) were subjected to hydrodistillation for 3 h in a Clevenger-type apparatus. After decanting and drying of the oils over anhydrous sodium sulfate, the corresponding oils were isolated in yields of 0.35% (w/w).

Preparation of methanol extracts

The essential oil (5 μg) was dissolved in a minimum amount of methanol. The obtained

* To whom all correspondence should be sent:
E-mail: akbaresmaeili@iau.ac.ir:

sample was used in the antibacterial and antioxidant activity tests.

Analysis

GC analysis of the oils was performed on a Shimadzu 15A gas chromatograph equipped with a split/splitless injector (250°C). Nitrogen was used as carrier gas (1 mL/min), and the capillary column used was DB-5 (50 m × 0.2 mm, film thickness 0.32 μm). The column temperature was maintained at 60°C for 3 min, then increased to 220°C with a rate of 5°C/min and kept at 220°C for 5 min.

GC/MS analysis was performed using a Hewlett-Packard 6890/5973 instrument with an HP-5MS column (30 m × 0.25 mm, film thickness 0.25 μm). The column temperature was maintained at 60°C for 3 min, then programmed to 220°C at a rate of 5 °C/min, and kept at 220°C for 5 min. The flow rate of the helium carrier gas was 1 mL/min. MS was taken at 70 eV.

Identification of the constituents of each oil was made by comparison of their mass spectra and retention indices (RI) with those given in the literature for authentic samples [25, 26]. Relative percentage amounts were calculated from the peak areas using a Shimadzu C-R4A Chromatopac without correction factors.

Antibacterial Activity

A collection of four microorganisms was used, including the Gram-positive bacteria *Staphylococcus aureus* (PTCC 1113), *Staphylococcus epidermidis* (PTCC 1349), *Staphylococcus saprophyticus* (PTCC 1379) and the Gram-negative bacteria *Erichia coli* (PTCC 1330) and *Pseudomonas aeruginosa* (PTCC 1310) identified by the Research Centre of Science and Industry, Tehran, Iran.

The microorganisms (obtained from enriched culture of the microorganisms in 1 mL of Mueller-Hinton broth incubated at 37 °C for 12 h) were cultured on Mueller-Hinton agar medium.

The following method was used to measure the antibacterial activity: 40 μL of diluted essential oil (40 μL oil in 2 mL DMSO 10%) were added to 200 μL of a microbial suspension (1 loop from the medium in physiological serum that corresponded to a 0.5 McFarland standard) in well 1 of a microplate, and 100 μL from this well were added to a 100 μL microbial suspension in well 2, and thiscontinued until 8 wells in the microplate were filled. The microplates were incubated at 37°C for 24 h.

Antioxidant activity

DPPH assay

The 2,2-diphenyl-1-picrylhydrazyl (DPPH) assay usually involves hydrogen atom transfer reaction, but, based on kinetic data, electron transfer mechanism has also been suggested for this assay [27, 28]. The radical-scavenging activity (RSA) of *T. pinnatum* essential oils was determined using a published DPPH radical-scavenging activity assay method [29, 30] with minor modifications. The decrease in absorbance at 517 nm was measured on a Perkin-Elmer spectrophotometer for all samples. Methanol was used to zero the spectrophotometer. The absorbance of the DPPH radical without antioxidant (control sample) was measured daily. Special care was taken to minimize the loss of free radical activity of the DPPH radical stock solution.

The inhibition percentage of free radical DPPH (I%) was calculated as follows:

$$I\,\% = [(A_{blank} - A_{sample})/A_{blank}] \times 100$$

where A_{blank} is the absorbance of the control sample (containing all reagents except the test compound), and A_{sample} is the absorbance of the test compound. The sample concentration providing 50% inhibition (IC_{50}) was calculated by plotting inhibition percentage against sample concentration. All tests were carried out in triplicate and IC_{50} values were reported as means ± SD of triplicates.

β-Carotene/linoleic acid bleaching assay

Antioxidant activity was determined by measuring the inhibition of volatile organic compounds and conjugated diene hydroperoxides arising from linoleic acid oxidation. The method described by Miraliakbari and Shahidi (2008) [30] was used with slight modifications. A stock solution of *β*-carotene and linoleic acid was prepared with 0.5 mg of *β*-carotene in 1 ml chloroform, 25 μl of linoleic acid and 200 mg of Tween 40. The chloroform was evaporated under vacuum and 100 ml of aerated distilled water were then added to the residue. The samples (2 g/l) were dissolved in DMSO and 350 μl of each sample solution were added to 2.5 ml of the above mixture in test tubes. The test tubes were incubated in a water bath at 50 °C for 2 h, together with two blanks, one containing the antioxidant BHT as a positive control and the other containing the same volume of DMSO instead of the extracts. The test tube with BHT maintained its yellow color during the incubation period. The absorbances were

measured at 470 nm on an ultraviolet spectrometer. Antioxidant activities (inhibition percentage, I%) of the samples were calculated using the following equation:

$$I\,\% = (A_{\beta\text{-carotene after 2h assay}} / A_{\text{initial }\beta\text{-carotene}}) \times 100$$

where $A_{\beta\text{-carotene after 2 h assay}}$ is the absorbance of β-carotene remaining in the samples after 2 h and $A_{\text{initial }\beta\text{-carotene}}$ is the absorbance of β-carotene at the beginning of the experiments. All tests were carried out in triplicate and inhibition percentages were reported as means ± SD of triplicates.

3. RESULTS AND DISCUSSION

Chemical composition of essential oils

The percentage chemical compositions of the essential oil from the aerial parts of *T. pinnatum* Boiss. are listed in Table 1. 25 components representing 98.7% of the oil were identified. The main components of the oil were: camphor (23.2%), α-pinene (8.5%) and camphene (7.7%), 1,8-cineole (7.3%), β-eudesmol (5.8%), and caryophyllene oxide (5.6%).

Table 1. Percentage composition of the oils in the aerial parts of *Tanacetum pinnatum*

Compound	RI*	%
α-Thujene	931	0.6
α- Pinene	939	8.5
Camphene	953	7.7
β-Pinene	980	1.1
p-Cymene	1026	4.2
1,8- Cineole	1033	7.3
γ-Terpinene	1062	0.5
Linalool	1098	4.5
2,6-Dimethyl phenol	1102	1.1
Ocimene	1129	4.6
Camphor	1143	23.2
Borneol	1165	4.6
Terpin-4-ol	1177	1.2
cis-Pinocarveol	1183	1.8
Dihydro carveol	1192	0.6
Myrtenol	1193	1.8
Methyl chavicol	1195	1.0
Dihydro myrcenol acetate	1215	2.6
Sabinene hydrate acetate	1219	0.7
cis-Carveol	1229	1.3
Carvacrol	1356	3.4
Caryophyllene oxide	1581	5.6
α-Muurolol	1645	3.2
β-Eudesmol	1649	5.8
Hexadecanoic acid	1970	1.8
Total		98.7

Other notable constituents in the oil from the aerial parts of the plant were: ocimene (4.6%), borneol (4.6%), *p*-cymene (4.2%) and linalool (4.5%). One of the studies [31] compared the composition of essential oils from *T. argyrophyllum* L. and *T. parthenium* L, determined by GC/MS. In our experiments, the α-pinene content was 8.5% for *T. pinnatum*, which complies with the above-mentioned results.

Camphor is usually externally applied to relieve arthritic and rheumatic pains. It is also used in steam vaporizers to control coughs by producing a local anesthetic action to the throat and to loosen congestion due to colds [32, 33].

Both enantiomers of camphor are found in nature, but the (−)-form is less common compared to the (+)-form. Although these two enantiomers have similar camphoraceous odor [32], little is known about their biological activity. According to Ravid *et al*. [33], enantiomerically pure (−)-camphor (100%) was found in *T. parthenium*, while *T. vulgare* was rich in (+)-camphor (75%). Enantioselective analysis can easily differentiate between these two common *Tanacetum* oils. Enantiomerically pure (−)-camphor (100%) was also detected in *T. armenum* and *T. haradjani* leaf oils [34]. α-Pinene enantiomers are widespread in the nature. α-Pinene is used in fragrance industry as a starting material for the synthesis of terpineols, borneol and camphor [32]. (+)-α-Pinene has a slight minty-terpene odor while (−)-α-pinene has a coniferous odor. Yassaa and William recently reported that (+)-α -pinene was the major enantiomer in the *Pinus sylvestris* chemotypes [33].

Determination of antioxidant activity with the 2,2'-diphenyl-1-picrylhydrazyl (DPPH) radical

The antioxidant activity of the essential oil of *T. pinnatum* was determined by the scavenging method using two different test systems, namely DPPH and β-carotene/linoleic acid. The antioxidant activity of volatile compounds was measured in terms of hydrogen donating or radical scavenging ability, using the stable radical DPPH. The degree of discoloration indicates the free radical scavenging potentials of sample/antioxidant and it has been found that known antioxidants such as cysteine, glutathione, ascorbic acid, tocopherol and polyhydroxy-aromatic compounds reduce DPPH by their hydrogen donating ability [36]. In the present study, the weakest radical scavenging activity was exhibited by the essential oil (568.1±4.3 μg ml^{-1}). The antioxidant activity of the essential oil was superior to that of all samples tested with an IC_{50} value of 151.9± 0.6 μg ml^{-1}. On the other hand, none of the samples showed activity as strong as the positive control BHT (88.4 ± 0.4 μg ml^{-1}). Particularly, synergistic effects of

Table 2. Antibacterial activity of the oils from the aerial parts of *Tanacetum pinnatum* based on the dilution method using four reagents. Values represent the mean diameter of the inhibitory zone (mm)

Bacterial Species	Gram +/–	Plant oils	Gentamicin	Penicillin	Sefazolin	Norfloxacin
Staphylococcus aureus PTCC 1113	+	24.2	0.0	0.0	15.7	0.0
Staphylococcus epidermidis PTCC 1349	+	32.7	30.3	21.0	30.3	31.0
Staphylococcus Saprophyticus PTCC 1379	+	29.7	0.0	25.0	20.0	11.0
Escherichia coli PTCC 1330	–	9.3	19.0	0.0	17.7	28.3
Pseudomonas aeruginosa PTCC 1310	–	15.4	15.6	0.0	15.3	30.3

phenolic acids e.g., rosmarinic acid and polyphenols, as well as other chemicals such as flavonoids could be also taken into account for the radical scavenging activity observed in methanol extracts [37].

In the *β*-carotene/linoleic acid model system, *β*-carotene undergoes rapid discoloration in the absence of an antioxidant. This is because of the coupled oxidation of *β*-carotene and linoleic acid, which generates free radicals. The linoleic acid free radical formed upon abstraction of a hydrogen atom from one of its diallylic methylene groups attacks the highly unsaturated *β*-carotene molecules. As a result, *β*-carotene is oxidized and broken down in part; subsequently the system loses its chromophore and characteristic orange color, which is spectrophotometrically monitored. The % inhibition capacity of the essential oil (88.4±1.2) was found to be superior to that of the sample which is nearest to the inhibition capacity of the positive control BHT (96.2 ± 0.9).

The auto-oxidation of linoleic acid without volatiles and methanol extracts accompanies the rapid increase of peroxides. According to Farag *et al*. (1989)[38], there is a relationship between the inhibition of hydroperoxide formation and the presence of phenolic nuclei in the essential oils and extracts. The antioxidative effectiveness of natural sources has been reported to be mostly due to phenolic compounds [39].

Antibacterial activity

The results of the antibacterial screening showed that *T. pinnatum* oil was active against the Gram-positive bacteria *Staphylococcus aureus* (PTCC 1113), *Staphylococcus epidermidis* (PTCC 1349) *Staphylococcus saprophyticus* (PTCC 1379) (36, 23 and 22 mm diameter respectively). The same oil showed inhibitory activity against the Gram-negative bacteria *Escherichia coli* (PTCC 1330) while *Pseudomonas aeruginosa* (PTCC 1310) (36, 31 and 29 mm diameter respectively) had only moderate inhibitory activity against *Escherichia coli* (9.3 mm diameter). The results of the antibacterial screening showed that *T. pinnatum* oil was insensitive against Gram-positive and Gram-negative bacteria except *Escherichia coli* Gram-negative bacteria, for which it had only moderate activity (14.0 mm diameter) (Table 2).

4. CONCLUSIONS

The purpose of this research was to study the *in vitro* antioxidant and antibacterial activities of *Tanacetum pinnatum* Boiss. grown in Iran. The essential oil is bactericidal for certain strains tested. The antioxidant activity of *T. pinnatum* may help in preventing oxidative damages in the human body, such as lipid peroxidation, associated with cancer and diabetes. The essential oil of *T. pinnatum* exhibited greatest antioxidant activity in the DPPH and *β*-carotene–linoleic acid test systems. The oil of *T. pinnatum* exhibited the highest antibacterial activity against *Staphylococcus aureus*. The essential oil of *T. pinnatum* may be used in perfumery.

Acknowledgements: *The authors wish to thank Dr. Kambiz Larijani, Department of Chemistry, Science & Research Campus, Islamic Azad University, Tehran, Iran.*

REFERENCES

1. K.H. Rechinger, Tanacetum. In: Flora Iranica, Compositae No. 158., K.H. Rechinger and I.C. Hedge, Eds., Akademische Druck- and Verlagsanstalt, Graz, Austria (1986).
2. V. Mozaffarian, Dictionary of Iranian Plant Names. Farhang Moaser Publishers, Tehran, Iran (1996).
3. M.I. Berry, Feverfew faces the future. *Pharm. J.*, **232**, 611 (1984).
4. A. Rustaiyan, K. Zare, Z. Habibi, M. Hasheml, *Phytochem*., **29**, 3022 (1990).
5. P. Tetenyi, E. Hethelyl, G. Kulcsar, P. Kaposi, *Herba Hung.*, **20**, 57 (1981).
6. W.R. Schearer, *J. Nat. Prod*., **47**, 964 (1984).
7. M. Holopainen, V. Kauppinen, *Acta Pharm. Fenn.*, **98**, 213 (1989).
8. J. Nawrol, *Pr. Nauk. lnst. Ochr. Rosl*., **24**, 173 (1983).
9. O.O. Thomas, *Fitoterapia*, **60**, 329 (1989).
10. A. Rustaiyan, F. Mojab, M. Salsali, S. Masoudi, M. Yari, *J. Essent. Oil Res.*, **11**, 497 (1999).
11. A. Monfared, S.S.H. Davarani, A. Rustaiyan, S. Masoudi, *J. Essent. Oil Res.*, **14**, 1 (2002).
12. A.L.M. Jawad, A.B.J. Dhahir, A.M. Hussain, *J. Biol. Sci. Res.*, **16**, 5 (1985).
13. N. Goren, J. Jakupovic and S. Topal, *Phytochem.*, **29**, 1467 (1990).
14. O.O. Thomas, *Fitoterapia*, **60**, 131 (1989).
15. O.O. Thomas. *Fitoterapia*, **60**, 1357 (1989).
16. O.O. Thomas, *Fitoterapia*, **60**, 138 (1989).
17. O.O. Thomas, *Fitoterapia*, **60**, 225 (1989).
18. O.O.Thomas, *Fitoterapia*, **60**, 229 (1989).
19. O.O. Thomas, *Fitoterapia*, **60**, 231 (1989).
20. O.O. Thomas, *Fitoterapia*, **60**, 323 (1989).
21. O.O. Thomas, *Fitoterapia*, **60**, 327 (1989).
22. Z. Habibi, T. Biniyaz, T. Ghodrati, S. Masoudi, A. Rustaiyan, *J. Essent. Oil Res.*, **19**, 28 (2007).
23. T. Majed-Jabari, H. Vatanpoor, A. Rustaiyan, S. Masoudi, A. Monfared, *J. Essent. Oil Res.*, **14**, 380 (2002).
24. A. Esmaeili, H. Amiri, Sh. Rezazadeh, *J. Med. Plants.*, **8,** 45 (2009).
25. R.P. Adams, Identification of Essential Oil Components by Gas Chromatography/Quadrupole Mass Spectroscopy, Allured Publishing, Carol Stream, IL, 2001.
26. M.J. Pérez-Alonso, A. Velasco-Negueruela, A. Burzaco, Tanacetum alsamita L.: A medicinal plant from Guadalajara (Spain); in P. Tétényi, A. Mathé (editors). Acta Horticulturae 306: International Symposium on Medicinal and Aromatic Plants, XXIII IHC (1992).
27. K. Jaimand, M.B. Rezaee, *J. Essent. Oil Res*. **26**, 312 (2005).
28. M.C. Foti, C. Daquino, C. Geraci, *J. Org. Chem*., **69**, 2309 (2004).
29. D. Huang, B. Ou, R.L. Prior, *J. Agric. Food Chem.*, **53**, 1841 (2005).
30. S.D. Sarker, Z. Latif, A. Gray, Natural Products Isolation. New Jersey, USA: Humana Press Inc. p. 20 (2006).
31. H. Miraliakbari, F.Shahidi, *Food Chem.*, **111**, 421 (2008).
32. www.drugs.com,http://xenical-secure.com/npp/feverfew.html.
33. K. Bauer, D. Garbe, H. Surburg, Common Fragrance and Flavor Materials, VCH, Weinheim, 1997, pp. 49, 60.
34. U. Ravid, E. Putievsky, I. Katzir, *Flav. Frag. J.*, **8**, 225 (1993).
35. S. Gallori, G. Flamini, A.R. Bilia, I. Morelli, A. Landini, F. F. Vincieri, *J. Agric Food Chem.*, **49**, 4907(2001).
36. K.H.C. Baser, B. Demirci, N. Tabanca, T. Özek, N. Gören, *Flav. Frag. J.*, **16**, 195 (2001).
37. M. S. Blois, *Nature*, **181**, 1199 (1958).
37. C.W. Choi, S.C. Kim, S.S. Hwang, B.K. Choi, H.J. Ahn, M.Y. Lee, S.H. Park, S.K. Kim, *Plant Science*, **163**, 1161 (2002).
38. R.S. Farag, A.Z. M.A. Badei, G.S. A. El-Baroty, *J. Amer. Oil Chem. Soc.*, **66**, 800 (1989).

АНТИОКСИДАНТНО И АНТИБАКТЕРИАЛНО ДЕЙСТВИЕ *IN VITRO* НА *TANACETUM PINNATUM* BOISS., РАСТЯЩО В ИРАН

А. Исмаил[1*] и Х. Амири[2]

[1]*Катедра по инженерна химия, Клон Северен Тейран, Ислямски университет Азад, Тейран, Иран*
[2]*Катедра по биология, Университет Лорестан, Кхорамабад, Иран*

Получена на 22 февруари 2010; Преработена на 5 юли 2010

(Резюме)

Това изследване е предназначено да провери антиоксидантното и антибактериално действие *in vitro* на надземната част на *Tanacetum pinnatum* boiss., растящо в Иран. В резултат на анализ чрез GC и GC-MS на етеричното масло са идентифицирани 25 съединения, представляващи 98.7% от съдържанието на маслото. Основните компоненти на маслото са камфор (23.2%), *α*- пинен (8.5%),%), камфен (7.7%), 1,8-цинеол (7.3%), *β*-еудесмол (5.8%) и кариофиленен оксид (5.6%). Възможното антиоксидантното и антибактериално действие на пробите е изследвано чрез DPPH и *β*- каротин-линолева киселина и дискова дифузия в агар, съответно. По принцип неполярният екстракт на *T. pinnatum* показа най-голяма антиоксидантна активност при тестовата система с DPPH. Етеричното масло прояви най-висока антиоксидантна активност при изследванията с *β*-каротин-линолева киселина, то показа най-добро антибактериално действие срещу *Staphylococcus aureus.*

Bulgarian Chemical Communications, Volume 43, Number 4 (pp.538 - 543) 2011

Catalytic neutralization of nitrogen oxides on low-percentage Mn/ZnO catalysts, obtained via oxalate precursor

B.V. Donkova[1]*, K.I. Milenova[2], M.S. Khristova[3], D.R. Mehandjiev[2]

[1]*Department of Inorganic Chemistry, Faculty of Chemistry, University of Sofia, 1 J. Bouchier Av., Sofia 1164, Bulgaria*
[2] *Institute of Catalysis, Bulgarian Academy of Sciences, Acad. G. Bonchev Str., bl. 11, Sofia 1113, Bulgaria*
[3]*Institute of General and Inorganic Chemistry, Bulgarian Academy of Sciences, Acad. G. Bonchev Str., bl. 11, Sofia 1113, Bulgaria*

Received October 19, 2010; Accepted January 10, 2011

Doped catalysts Mn/ZnO (Mn ≈ 0.035 wt.%) are obtained through decomposition of zinc oxalate. The precursors are prepared at two different Zn^{2+}:$C_2O_4^{2-}$ ratios in the initial solutions. In spite of the low manganese content, the $T_{\eta=50\%}$ decreased by 66ºC after the doping. It was established that in the case of doped samples the amount of reacted NO is higher than that of reacted CO. This fact, as well as the results from the TPD measurements, suggest that in the presence of Mn another type of catalytically active sites are being formed in addition to those existing on the surface of pure ZnO. As a result of this, along with catalyzed reduction of NO with CO, direct decomposition of NO to N_2 and O_2 is observed at temperatures higher than 300ºC.

Keywords: doped ZnO, $ZnC_2O_4.2H_2O$, manganese, NO reduction

INTRODUCTION

One of the important contemporary problems, which has not been optimally solved yet, is the neutralization of nitrogen oxides, especially in the presence of other oxidizing agents and most often in the presence of oxygen. In order to solve this problem, investigations are directed towards searching for new and more efficient catalysts. The neutralization of NO is mainly accomplished through a reduction process and therefore the search is focused on substances catalytically active in the reaction of NO reduction. In this respect, it seems that the most promising catalysts are those based on transition elements [1–11].

In the search for active catalyst, an essential problem is the choice of precursor. During the last years the application of the slightly soluble $ZnC_2O_4.2H_2O$ for preparing nanosized pure ZnO and ZnO doped with transition metal ions is increasing in importance [12–23]. An advantage of the oxalate precursor is its easy synthesis, the low temperature of decomposition, the liberation of a large amount of volatile substances (CO, CO_2, H_2O vapour) and the possibility of obtaining ZnO with different crystal forms and sizes. This explains the application of zinc oxalate as a precursor of catalysts [25–29]. Another advantage is the fact that the oxalates belonging to the magnesium series (Mg, Mn, Co, Fe, Ni and Zn) are isomorphous. This enables the modifying of the ZnO physical properties by doping of the precursor in the course of its synthesis [20–22, 28, 29].

In a previous publication [29], we have established that the doping of ZnO with low concentrations of Mn considerably promotes the catalytic activity of the oxide with respect to the oxidation of CO. For this reason, the aim of the present work was to investigate the catalytic activity of Mn/ZnO in the model reaction of NO reduction with CO by tracing the influence of the concentration of the oxalate ions during the precursor preparation.

EXPERIMENTAL

Synthesis of the samples

The samples of pure and manganese doped ZnC_2O_4 were synthesized by chemical reaction between $ZnSO_4$ and $K_2C_2O_4$ solutions at two different ratios of the initial molar concentrations of zinc and oxalate ions. Samples having a ratio Zn^{2+}:$C_2O_4^{2-}$ = 1:2 were prepared, denoted as the (1:2) series, while those with a ratio Zn^{2+}:$C_2O_4^{2-}$ = 1:1 were denoted as the (1:1) series. The experimental conditions were as follows: temperature T = 25.0 ± 0.5ºC; initial acidity of the system pH = 3.0 ± 0.1; synthesis duration 10 days

*To whom all correspondence should be sent:
E-mail: : bdonkova@inorg.chem.uni-sofia.bg

under electromechanical stirring at 1000 r.p.m. For the preparation of the doped oxalate samples, a certain amount of the dopant (taken from 0.25 M $MnSO_4$ stock solution) was added to the $K_2C_2O_4$ solution before the mixing step. More details about the synthesis procedures and justification of the selected experimental conditions have been published previously [29].

In order to prepare pure and manganese doped ZnO, the synthesized oxalate precursors were calcined for 1 h in air at 470ºC. The oxalate decomposition was controlled by accounting for the changes in the weight of the sample.

The samples prepared in this way are denoted as ZnO (1:1), ZnO (1:2), 0.035 Mn/ZnO (1:1) and 0.039 Mn/ZnO (1:2). The labelling of the samples (1:2) or (1:1) indicates the initial ratio Zn^{2+}:$C_2O_4^{2-}$ during the precursor preparation, while the index 0.035 and 0.039 represents the content of manganese in the oxide sample in percentage by weight.

Sample characterization

The chemical composition of the samples was determined by means of atomic absorption analysis on a FAAS-SOLAAR M5 spectrometer. The X-ray diffraction (XRD) analysis was carried out on a Siemens powder diffractometer model D500. The scanning electron microscope (SEM) observation was carried out on a JEOL JSM–5510 apparatus. The electron paramagnetic resonance (EPR) spectra were registered using an ERS 220/Q instrument. The determination of the specific surface area of the samples was carried out by nitrogen adsorption at the boiling point temperature of liquid nitrogen 77.4 K using N_2/He mixture. The nitrogen adsorption isotherm was used to calculate the specific surface area (A_{BET}) according to the BET equation.

Catalytic activity testing

NO reduction reaction. The experimental runs to determine catalytic activity were carried out in a continuous flow reactor, described in details in [30]. The NO reduction with CO was investigated within the temperature range 20 – 400ºC. The catalytic activity tests were performed with a gas mixture: NO + CO + Ar, containing 1200 ppm NO and 1200 ppm CO. Argon (purity grade 99.99 vol.%) was used as a carrier at a gas hourly space velocity (GHSV) of 20ºº00 h^{-1}. A 1 cm^3 sample of the catalyst (sieve fraction 0.3 – 0.6 mm) was charged in the reactor representing a quartz glass tube of inner diameter d = 10 mm.

Temperature-programmed desorption (TPD) was accomplished in the following way. A reaction mixture, consisting of CO and NO, was fed into the reactor in advance, passing through the catalyst bed at 25°C for 30 min. Thereafter, preserving the same temperature, argon was fed into the reactor and an increase in the temperature was started at a rate of 13ºC min^{-1} in the temperature interval 25–400°C. The inlet concentrations of NO and CO were continuously monitored by gas analysers. The outlet concentrations of NO and CO were controlled by "UNOR–5" (Maihak, Germany), while that of CO_2 was followed using "Infralyt 2106" (Germany). The N_2O concentration was measured spectrophotometrically by "Specord 75 IR" (Germany) with a 1 m folded path gas cell (Specac).

RESULTS AND DISCUSSION

Table 1 lists the content of Mn, the specific surface area of the catalyst samples, as well as the phase composition of the pure and Mn doped zinc oxide. The table also presents the degree of oxidation of the manganese ions, determined on the basis of the EPR spectra of doped samples. The EPR investigation revealed that the type of the spectrum does not depend on the Zn^{2+}:$C_2O_4^{2-}$ ratio in the initial solution [29]. The sextet signal typical of isolated Mn^{2+} ions was registered. This means that if Mn^{3+} and Mn^{4+} ions are present in the sample, their amount is negligibly small. The well-shaped well-separated peaks show that the doping agent is present only in small concentrations and is uniformly distributed inside the crystal lattice of ZnO.

The X-ray diffraction analysis of the oxide samples indicates the formation of wurtzite ZnO (JCPDS 36–1451) in all samples of both series [29], because of the low manganese content. However, the electron micrographs (Fig. 1) show some difference in the morphology of series (1:1) and (1:2). Polyhedral crystals are observed in the former case, while the prevailing number of crystals in the latter one has a prismatic form and they form aggregates. It is obvious that the gases,

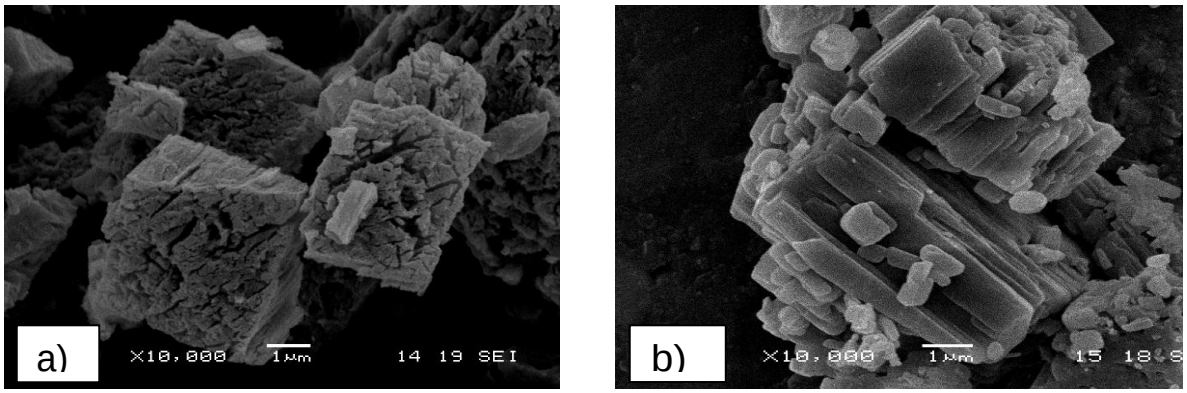

Fig. 1. Electron micrographs of a) ZnO (1:1); b) ZnO (1:2).

Table 1. Composition and properties of the samples studied

Sample	Content of Mn (wt. %)	Specific surface area A_{BET}, (m^2/g)	Phase composition (XRD)	Oxidation state of Mn (EPR)
ZnO (1:1)	-	27	ZnO	-
ZnO (1:2)	-	27	ZnO	-
0.035 Mn/ZnO (1:1)	0.0353	25	ZnO	Mn^{2+}
0.039 Mn/ZnO (1:2)	0.0385	25	ZnO	Mn^{2+}

which are liberated during oxalate decomposition, diffuse through the crystals in different ways, thus forming different types of channels. In the case of (1:1) series (Fig. 1a), pores and cracks on the surface of the polyhedra are observed, while in the case of (1:2) series the surface is smooth and the channels are probably located between the separate prismatic crystals. The doped ZnO possesses the same morphology.

Figure 2 represents the temperature dependence of the NO conversion degree for pure and manganese doped oxide samples. At the beginning of the studied temperature range, the reduction proceeds with low catalytic activity for all samples. However, the conversion with the non-doped samples begins at temperatures above 100ºC, while the doped samples already manifest activity at this temperature. Despite the low manganese content, the doping leads to a decrease of the starting temperature of NO active reduction with CO by 50ºC. At one and the same content of the active component, the sample belonging to the (1:2) series is more active than that of the (1:1) series. A possible cause is the more uniform distribution of manganese ions, which is associated with the different mechanism of inclusion that depends on the initial oxalate concentration [31]. A conversion degree of 70% for NO was achieved at 300ºC with the 0.039 Mn/ZnO (1:2) sample, while the same conversion degree was reached with the sample 0.035 Mn/ZnO (1:1) at 400°C. The studies revealed that with both samples under consideration, NO reduction with CO occurred with N_2 formation. Within the entire investigated temperature interval no N_2O was registered.

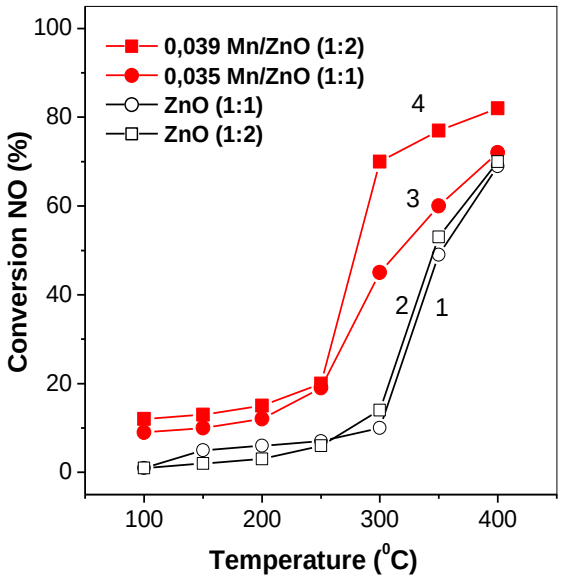

Fig. 2. Temperature dependence of the NO conversion degree in the reaction NO+CO: curve 1 - ZnO (1:1), curve 2 - ZnO (1:2), curve 3 – 0.035Mn/ZnO (1:1), curve 4 – 0.039Mn/ZnO (1:2).

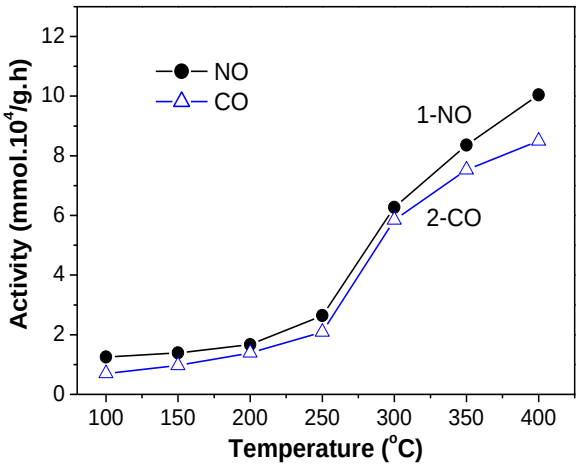

Fig. 3. Amount of NO (mmol.10^4/g.h) – curve 1, and amount of CO (mmol.10^4/g.h) – curve 2, reacted for sample 0.035 Mn/ZnO (1:1).

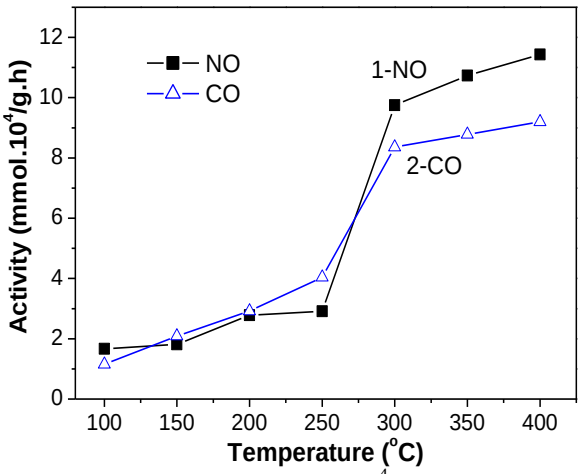

Fig. 4. Amount of NO (mmol.10^4/g.h) – curve 1, and amount of CO (mmol.10^4/g.h) – curve 2 reacted for sample 0.039 Mn/ZnO (1:2).

Figures 3 to 5 juxtapose the temperature dependences of the reacted amounts of NO and CO by 1 g catalyst per 1 hour for each studied sample. Figure 3 refers to the 0.035 Mn/ZnO (1:1) sample, Figure 4 – to the 0.039 Mn/ZnO (1:2) sample, while Figure 5 – to the pure ZnO samples of both series. With the non-doped catalyst samples the quantity of reacted NO is equal to the quantity of reacted CO, while in the case of the doped samples there is some difference between the two quantities. In both cases, at temperatures higher than 300°C the amount of reacted NO is higher than that, stoichiometrically necessary for the reaction with CO. For the 0.039 Mn/ZnO (1:2) sample this difference is slightly bigger. These data show that in addition to the catalytic reduction with CO one should also suppose the occurrence of the reaction of direct NO decomposition. Such parallel reaction

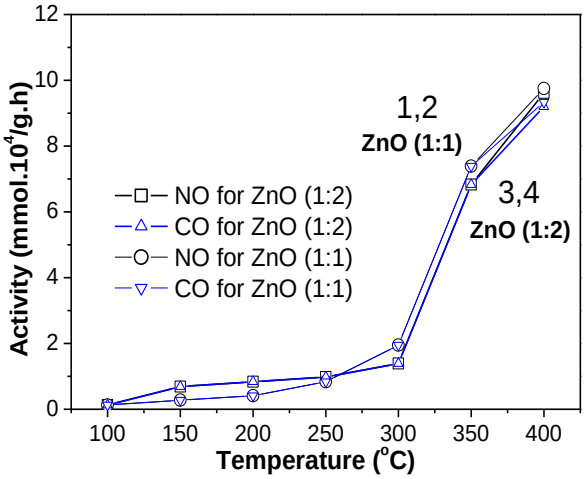

Fig. 5. Amount of NO (mmol.10^4/g.h) reacted for samples ZnO (1:1) – curve 1 and ZnO (1:2) – curve 3, amount of CO (mmol.10^4/g.h) reacted for samples ZnO (1:1) – curve 2 and ZnO (1:2) – curve 4.

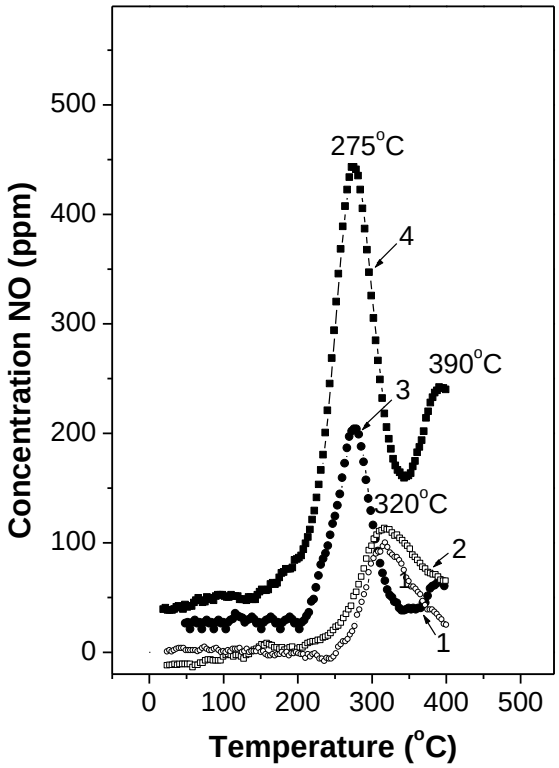

Fig. 6. TPD patterns of NO for the studied samples: ZnO (1:1) – curve 1 and ZnO (1:2) – curve 2, 0.035Mn/ZnO (1:1) – curve 3 and 0.039Mn/ZnO (1:2) – curve 4.

of direct decomposition of NO to N_2 and O_2 has also been observed for catalytic systems containing Ag and Pd [7, 32]. Therefore, two reactions are taking place on the surface of the doped catalyst – catalytic reduction of NO with CO and direct decomposition of NO.

The above conclusion is confirmed by the results of the TPD measurements. Figure 6 presents the TPD patterns of NO for all studied samples after carrying out the catalyzed reduction of NO with CO. The patterns were recorded in a flow of Ar within the temperature interval 25 – 400ºC. No peaks of CO and CO_2 desorption are observed within the entire studied temperature interval for all samples, which is an indication that CO is not adsorbed in any form on their surface. As far as the pure ZnO samples are concerned, a single desorption peak at 320°C is observed. In the case of the doped samples 0.035 Mn/ZnO (1:1) and 0.039 Mn/ZnO (1:2) two expressed NO desorption peaks are present in the pattern having maxima at 275ºC and ~390ºC. The NO is adsorbed on the surface of these samples in two different forms – one of which is weakly bound and the other has stronger bonding. These results imply that two different types of catalytically active sites are probably formed on the surface of doped samples.

The correlation between the quantities of reacted NO and CO in the case of non-doped samples, as well as the lack of CO desorption peaks, allow us to draw the conclusion that the probable mechanism via which the catalyzed reduction of NO with CO occurs on pure ZnO samples at temperatures higher than 250ºC belongs to the Eley-Rideal type. It occurs in accordance with Scheme (1): NO is adsorbed on the surface and thereafter CO from the gas phase reacts with it.

$$2\ NO + [CAC]_a \rightarrow NO[CAC]_a.NO$$
$$NO[CAC]_a.NO + 2(CO)_{gas} \rightarrow N_2 + 2\ CO_2 + [CAC]_a$$

Scheme 1

Here [CAC] is the catalytically active complex on the surface of the sample, which, in our opinion, may comprise several active sites.

The difference in the reacted amounts of NO and CO in the case of the doped samples, as well as the second peak in the TPD-NO curves show that in parallel to the reactions described in Scheme (1), one should also suppose a direct decomposition of NO to $N_2 + O_2$ according to Scheme (2), which proceeds on a different type of catalytically active sites $[CAC]_b$ at temperatures ≥ 300ºC.

$$2\ NO + [CAC]_b \rightarrow NO[CAC]_bNO$$
$$\rightarrow N_2 + O_2 + [CAC]_b$$

Scheme 2

Therefore, it may be assumed that two types of catalytically active complexes [CAC] are formed on the surface of the samples in the presence of manganese. This is confirmed by the fact that there is only one peak of NO desorption in the TPD pattern of the spent ZnO catalyst, while in the case of doped samples two desorption peaks are observed. As was mentioned above, proceeding of such parallel reactions was observed with Ag- and Pd-doped catalysts [7, 32].

CONCLUSIONS

The studies carried out revealed that the co-crystallization method applied for doping ZnO with manganese leads to uniform distribution of the manganese ions inside the structure of ZnO and there is no interaction between them.

In spite of the low manganese content in the samples (0.035% and 0.039%), the catalytic activity tests demonstrated the effectiveness of doping in view of purifying gaseous fluids by NO_x removal – lowering of the temperature of active reduction by 50ºC, as well as increasing the conversion degree from 10% up to 70% at 300ºC. On the basis of TPD measurements it may be concluded that this is due to the weaker bonding of NO molecules on the surface of doped samples which facilitates their reduction. At one and the same dopant content, the sample of the 1:2 series was more active than the respective sample of the 1:1 series, probably due to the more uniform distribution of manganese ions on the former samples. A conversion degree of 70% was achieved at 300ºC with the 0.039Mn/ZnO (1:2) catalyst sample, while with the sample 0.035 Mn/ZnO (1:1) the same conversion was reached at 400ºC.

The obtained data also enabled drawing the conclusion that Mn doping leads to the formation of another type of catalytically active complexes $[CAC]_b$ in addition to those existing on the surface of pure ZnO ($[CAC]_a$). As a result of this, beside the NO reduction reaction with CO on $[CAC]_a$, above a certain temperature there occurs also direct decomposition of NO on $[CAC]_b$.

Acknowledgements: *The authors acknowledge the financial support of the Scientific Research Fund of Sofia University (Project 020/2007) and DO-02-82/2008, project UNION.*

REFERENCES

1 M. Shelef, H. Gandhi, *Ind. Eng. Chem. Prod. Res. Dev.*, **13**, 80 (1974).
2 P. Araya, F. Gracia, J. Cortes, E. Wolf, *Appl. Catal. B*, **38**, 77 (2002).

3 P. Sreekanth, P. Smirniotis, *Catal. Lett.*, **122**, 37 (2008).
4 J. Shu, W. Xia, Y. Zhang, T. Cheng, M. Gao, *Chin. J. Chem.Phys.*, **21**, 393 (2008).
5 D. Mehandjiev, E. Bekyarova, M. Khristova, *J. Colloid Interface Sci.*, **192**, 440 (1997).
6 M. Khristova, D. Mehandjiev, *Carbon*, **36**, 1379 (1998).
7 L. Radev, M. Khristova, D. Mehandjiev, B. Samuneva, *Catal. Lett.*, **112** , 181 (2006).
8 N.B. Stankova, M.S. Khristova, D.R. Mehandjiev, *J. Colloid Interface Sci.*, **241**, 439 (2001).
9 R. Nickolov, N. Stankova, M. Khristova, D. Mehandjiev, *J. Colloid Interface Sci.*, **265**, 121 (2003).
10 D. Mantri, P. Aghalayam, *Catal. Today*, **119**, 88 (2007).
11 C. Neyertz, M. Volpe, D. Perez, I. Costilla, M. Sanchez, C. Gigola, *Appl. Catal. A*, **368**, 146 (2009).
12 K.G. Kanade, B.B. Kale, R.C. Aiyer, B.K. Das, *Mater. Res. Bull.*, **41**, 590 (2006).
13 G.M. Duffy, S.C. Pillai, D.E. McCormack, *J. Mater. Chem.*, **17**, 181 (2007).
14 S.C. Pillai, J.M. Kelly, D.E. McCormack, P. O'Brien, R. Ramesh, *J. Mater. Chem.*, **13**, 2586 (2003).
15 L. Guo, Y. Ji, H. Xu, Z. Wu, P. Simon, *J. Mater. Chem.*, **13**, 754 (2003).
16 T. Ahmad, S. Vaidya, N. Sarkar, S. Ghosh, A.K. Ganguli, *Nanotechn.*, **17**, 1236 (2006).
17 L. Yang, G. Wang, C. Tang, H. Wang, L. Zhang, *Chem. Phys. Lett.*, **409**, 337 (2005).
18 S.C. Pillai, J.M. Kelly, D.E. McCormack, R. Ramesh, *J. Mater. Chem.*, **14**, 1572 (2004).
19 H. Niu, Q. Yang, K. Tang, Y. Xie, F. Yu, *J. Mater. Sci.*, **41**, 5784 (2006).
20 C.J. Cong, L. Liao, J.C. Li, L.X. Fan, K.L. Zhang, *Nanotechn.*, **16**, 981 (2005).
21 C.J. Cong, L. Liao, Q.Y. Liu, J.C. Li, K.L. Zhang, *Nanotechn.*,**17**, 1520 (2006).
22 S. Thota, T. Dutta, J. Kumar, *J. Phys.: Condens. Matter.*, **18**, 2473 (2006).
23 H. Niu, Q. Yang, K. Tang ,Y. Xie, F.Yu, *J. Mater. Sci.*, **41**, 5784 (2006).
24 H. Wilmer, M. Kurtz, K. V. Klementiev, O. P. Tkachenko, W. Grünert, O. Hinrichsen, A. Birkner, S. Rabe, K. Merz, M. Driess, C. Wöll, M. Muhler, *Phys. Chem. Chem. Phys.*, **5**, 4736 (2003).
25 M. Muruganandham, J. Wu, *Appl. Catal. B*, **80**, 32 (2008).
26 J. Agrell, M. Boutonnet, I. Cabrera, J. Fierro, *Appl. Catal. A*, **253**, 201 (2003).
27 J. Agrell , M. Boutonnet, J. Fierro, *Appl. Catal. A*, **253**, 213 (2003).
28 B. Donkova, K. Milenova, D. Mehandjiev, *Oxid. Commun.*, **32**, 579 (2009).
29 B. Donkova, K. Milenova, D. Mehandjiev, *Cent. Eur. J. Chem.*, **6**, 115 (2008).
30 D. Panayotov, M. Khristova, D. Mehandjiev, *Appl. Catal.*, **34**, 49 (1987).
31 B. Donkova, J. Pentsheva, M. Djarova, *Cryst. Res. Technol.*, **39**, 207 (2004).
32 M. S. Khristova, S. P. Petrović, A. Terlecki-Baričević, D. R. Mehandjiev, *Cent. Eur. J. Chem.*, **7**, 857 (2009).

КАТАЛИТИЧНА РЕДУКЦИЯ НА АЗОТНИ ОКСИДИ ВЪРХУ НИСКО-ПРОЦЕНТНИ Mn/ZnO КАТАЛИЗАТОРИ, ПОЛУЧЕНИ ОТ ОКСАЛАТЕН ПРЕКУРСОР

Б.В. Донкова[1], К.И. Миленова[2], М.С. Христова[3], Д.Р. Механджиев[2]

[1]Катедра по неорганична химия, Химически факултет, СУ "Св. Климент Охридски", бул. Дж. Баучер 1, София 1164

[2] Институт по катализ, Българска академия на науките, ул. Акад. Г. Бончев бл.11, София 1113

[3]Институт пообща и неорганична химия Българска академия на науките, ул. Акад. Г. Бончев бл.11, София 1113

Постъпила на 19 октомври, 2010 г.; приета на 10 януари, 2011 г.

(Резюме)

Катализатори Mn/ZnO (Mn ≈0.035 wt.%) са синтезиране чрез разлагане на дотиран цинков оксалат, получен при две различни съотношения Zn^{2+}:$C_2O_4^{2-}$ в изходните разтвори. Дотирането на ZnO води до понижаване на $T_{\eta=50\%}$ с 66°C, независимо от ниското съдържание на манган в пробите. Установено е, че при дотираните образци количеството реагирал NO е по-високо от това на реагиралия CO. Този факт, както и данните от TPD измерванията, водят до предположението, че в присъствие на Mn на повърхността на катализатора се формират и друг тип каталитично активни центрове в допълнение на наличните при недотиран ZnO. В резултат на това, освен катализирана редукция на NO с CO протича и директно разлагане на NO до N_2 и O_2 при температури по-високи от 300ºC.

Bulgarian Chemical Communications, Volume 43, Number 4 (pp 544 – 551) 2011

Inhibitive action of the catechol-zinc system in controlling the corrosion of carbon steel

H. Benita Sherine[1*], S. Felci Sagaya Mary[2], S. Rajendran

[1,2] *Department of Chemistry, Holy Cross College, Tiruchirappalli – 620 002, Tamilnadu, India*
[3] *Department of Chemistry, GTN Arts College, Dindigul – 624 005, Tamilnadu, India.*

Received December 17, 2010; Accepted January 4, 2011

The inhibition efficiencies of inhibitor systems constituting various combinations of catechol and zinc ions in controlling corrosion of carbon steel immersed in ground water for 3 days was evaluated by the weight-loss method. 100 ppm of Zn^{2+} has only 15% inhibition efficiency (IE). When 100 ppm of catechol was added, the IE increased to 90%. Weight-loss method, polarization studies and AC impedance spectra were employed. The nature of the protective film formed on the metal surface was analyzed by FTIR spectroscopy. The protective film was found to consist of Fe^{2+} - catechol complex. Synergism parameters and analysis of variance (ANOVA) were used to evaluate the synergistic effect existing between the inhibitors.

Keywords: Carbon steel, corrosion inhibition, catechol, F-test, synergistic effect, FTIR.

1. INTRODUCTION

Corrosion and scaling of carbon steel may be inhibited by the use of inhibitors. It has been observed that the effect of corrosion inhibitors is always caused by change in the state of the protected surface due to adsorption or formation of hardly soluble compounds with metal cations. A review including extensive listing of various types of organic inhibitors has been published [1]. The most often used corrosion inhibitors are nitrogen, sulphur, oxygen and phosphorous containing compounds [2-6]. These compounds get adsorbed onto the metal from the bulk of the environment and form a film at the metal surface. The inhibition efficiency (IE) increases in the order O<N<S<P [7]. The corrosion inhibition of metals in acidic media by different types of organic compounds has been widely studied [8-13]. The inhibition action of organic molecules is primarily due to their adsorption on the surface of the metal through the presence of active centres. Rodge *et al*. [14] have evaluated the effect of phenol on the corrosion of mild steel in nitric acid of various concentrations. The percent loss in weight was found to increase linearly with increase in acid concentration. The IE values were ordered as follows: *p*-cresol>*m*-cresol>2-naphthol>phenol>1-naphthol>2-nitrophenol. Muller *et al*. have studied the use of phenol and substituted phenols such as amino phenols and nitro phenols for aluminium pigment in acid and alkaline medium as corrosion inhibitors [15]. Viswanathan *et al*. [16] have studied the inhibitory action of methoxy phenol (MPH) and nonyl phenol (NPH) on the corrosion of N80 steel in 15% HCl. MPH and NPH have shown maximum inhibition at about 83 and 78% inhibitor concentration in the acid, respectively, after 6 h exposure test at ambient temperature. Kulkarni *et al*. [17] have studied the inhibition of the corrosion of mild steel in nitric acid, sulphuric acid and hydrochloric acid media by phenols. The trend observed was: p-cresol>m-cresol>phenol>2-naphthol>1-naphthol>2-nitrophenol. Among naphthols, 2-naphthol was stronger inhibitor than 1-naphthol. In general, 2-naphthol and p-cresol were found to be stronger over the range of concentrations of acids used.

The corrosion inhibition characteristics of *m*-nitrophenol-Zn^{2+}, thiophenol-Mn^{2+} in ground water and hydroquinone-Zn^{2+} in well water was studied by Benita *et al*. [18-20] in controlling the corrosion of carbon steel. Most of the industries require water for cooling purpose. The major problems in the industrial use of the cooling water systems are the corrosion of the metal equipment and the scale formation. Hence, an attempt was made to assess the inhibition efficiency of catechol with zinc ions in controlling the corrosion of carbon steel in ground water.

The aim of the present study was:

1. To evaluate the inhibition efficiency of catechol in controlling the corrosion of carbon steel immersed in ground water in the presence and absence of zinc ions;

* To whom all correspondence should be sent: E-mail: beni2@rediffmail.com

2. To evaluate the synergistic effect of catechol and zinc ions by determining synergism parameters;
3. To investigate whether the synergistic effect established for this inhibitor system is statistically significant or not by means of the F-test using analysis of variance (ANOVA);
4. To propose a suitable mechanism of corrosion inhibition based on the results obtained from the weight-loss method, FTIR, AC impedance and polarization studies.

2. METHODS AND MATERIALS

Carbon steel specimens (containing 0.03% S, 0.05% P, 0.5% Mn, and 0.15% C) of dimensions 1.0×4.0×0.2 cm were used in the weight-loss study. Carbon steel encapsulated in Teflon, polished to mirror finish and degreased with trichloroethylene, with surface area of the exposed metal surface 1 cm^2, was used in the electrochemical studies.

The experiments were carried out at room temperature (36° C). Three carbon steel specimens were immersed in 100 ml of solutions containing ground water and various concentrations of catechol in the absence and presence of Zn^{2+} ($ZnSO_4.7H_2O$) for a period of 3 days. The weights of the specimens before and after immersion were determined using a Shimadzu balance AY62. Inhibition efficiency (IE) was calculated from the relationship $IE = (1-W_2/W_1) \times 100$, where W_1 = corrosion rate in the absence of inhibitor, and W_2 = corrosion rate in the presence of inhibitor.

After being immersed in the test solutions, the specimens were taken out and dried. The nature of the film formed on the surface of the metal specimens was analyzed by surface analysis technique. IR spectra were recorded with the Perkin Elmer 1600 spectrophotometer. The FTIR spectrum of the protective film was recorded by carefully removing the film, mixing it with KBr and preparing a pellet.

The polarization study was carried out in an H and CH electrochemical workstation impedance analyzer Model CHI 660A provided with iR compensation facility, using a three-electrode cell assembly. Carbon steel was used as working electrode, platinum as counter electrode and saturated calomel electrode (SCE) as reference electrode. After having done iR compensation, polarization study was carried out at a sweep rate of 0.01 V/s. The corrosion parameters such as linear polarization resistance (LPR), corrosion potential $E_{corr,}$ corrosion current I_{corr} and Tafel slopes (b_c and b_a) were measured. During the polarization study, the scan rate (V/s) was 0.01; hold time at Ef (s) was zero and quiet time (s) was 2. The values of I_{corr} were used to calculate the inhibition efficiency using the following equation:

$$IE\% = [(I^0_{corr} - I^1_{corr})/ I^0_{corr}] \times 100,$$

where I^0_{corr} and I^1_{corr} are the corrosion current density values in the absence and presence of inhibitor, respectively.

AC impedance spectra were recorded on the instrument used for polarization study, using the same three-electrode cell assembly. The real part (Z') and the imaginary part (Z") of the cell impedance were measured in Ohms for various frequencies. The charge transfer resistance (R_t) and double layer capacitance (C_{dl}) values were calculated.

$R_t = (R_s + R_t) - R_s$, where R_s = solution resistance;

$C_{dl} = ½\pi\ R_t\ f_{max}$, where f_{max} = maximum frequency.

The R_t values estimated from the above-mentioned equivalent circuit were used to calculate IE% according to the following equation:

$$IE\% = [(R^1_t - R^0_t)/ R^1_t] \times 100,$$

where R^0_t and R^1_t are the charge transfer resistances in the absence and presence of additive, respectively.

Carbon steel specimens immersed in a blank and in an inhibitor solution for a period of one day were taken out, rinsed with redistilled water, dried and observed in a scanning electron microscope to examine the surface morphology. The surface morphology measurements of the carbon steel were performed on a Hitachi S-3000 H computer-controlled scanning electron microscope.3.

3. RESULTS AND DISCUSSION

The ground water used in this study is given in Table 1. The corrosion rates of carbon steel, immersed in ground water in the absence and presence of catechol and Zn^{2+}, determined by the weight-loss method, are presented in Table 2. The inhibition efficiencies are presented in Table 3.

It is seen from Table 2 that when carbon steel was immersed in ground water, the corrosion rate was 139.29 mpy. Upon addition of various concentrations of catechol, the corrosion rate slowly decreased, i.e., the metal was protected against corrosion**.**

The influence of a divalent metal ion, Zn^{2+}, on the inhibition efficiency of catechol in controlling

Table 1. Water Quality Parameters

Parameters	Value
pH	7.30
Total Dissolved Solids	1236 ppm
Chloride	232 ppm
Sulphate	75 ppm
Total Hardness	416 ppm
Conductivity	1792 μmhos/cm

the corrosion of carbon steel, is given in Table 3. It is seen that the addition of 250 ppm of catechol alone gives a maximum IE of 52% and additions of various concentrations of Zn^{2+} ions to ground water offer a maximum IE of 15% at 100 ppm of Zn^{2+}. The combination of Zn^{2+} and catechol provides for better IE. For example, 100 ppm of Zn^{2+} gives an IE of 15%; 100 ppm of catechol gives an IE of 32%, while their simultaneous use offers a maximum inhibition efficiency of 90%. The improvement in

Table 2. Corrosion rates (CR) obtained from catechol- Zn^{2+} system, when carbon steel is immersed in ground water. Inhibitor: Catechol +Zn^2

Catechol (ppm)	Corrosion rate (CR) mpy*					
-	0	10	25	50	75	100
0	132.29	132.32	128.14	126.75	122.57	118.39
50	78	78	32	17	12	13
100	59	78	81	22	58	8
150	48	66	35	27	17	22
200	43	43	48	32	23	25
250	41	61	50	37	28	17

*) mpy- mils per year

Table 3. Inhibition efficiencies (IE) obtained from catechol- Zn^{2+} system, when carbon steel is immersed in ground water. Inhibitor: Catechol +Zn^2

Catechol (ppm)	Corrosion rate (CR) mpy*					
-	0	10	25	50	75	100
0	0	5	8	9	12	15
50	10	10	64	81	87	85
100	32	10	6	75	83	90
150	45	23	25	69	81	75
200	50	50	44	64	73	71
250	52	29	42	58	67	80

Inhibitor: Catechol +Zn^2

Table 4 Synergism parameters derived from inhibition efficiencies of Catechol–Zn^{2+} system.

Catechol (ppm)	Zn^{2+} 0 (ppm)	10 (ppm)	S_I	25 (ppm)	S_I	50 (ppm)	S_I	75 (ppm)	S_I	100 (ppm)	S_I
0	0	0	5	-	8	-	9	-	12	-	15
50	50	10	10	0.95	64	2.30	29	1.15	81	4.16	85
100	100	32	23	0.72	6	0.66	67	1.87	33	0.89	90
150	150	45	50	0.68	25	0.67	76	2.08	81	2.54	75
200	200	50	29	0.95	44	0.82	72	1.62	73	1.62	71
250	250	52	27	0.64	42	0.76	64	1.21	67	1.28	80

the protection efficiency was attributed to the synergistic effect resulting from the combination of the two inhibitors, Zn^{2+} and catechol, which form a complex. As a result of the complex formation, the inhibitor molecules are readily transported from the bulk of the solution to the metal surface [21-23].

Synergism parameters (S_I) were calculated using the relation

$$S_1 = \frac{1- \theta_{1+2}}{1- \theta'_{1+2}}$$

where:

$\theta_{1+2} = (\theta_1 + \theta_2) - (\theta_1 \theta_2)$

θ_1 = Surface coverage (θ) of inhibitor catechol

θ_2 = Surface coverage (θ) of inhibitor Zn^{2+}

θ'_{1+2} = Combined surface coverage (θ) of inhibitor catechol and Zn^{2+}.

Synergism parameters are indicative of the synergistic effect existing between two inhibitors [24-26]. The values of the synergism parameters (Table 4) are greater than unity, indicating a synergistic effect existing between Zn^{2+} and various concentrations of catechol.

To investigate whether the influence of Zn^{2+} on the inhibition efficiency of catechol is statistically significant, analysis of variance (F-test) was carried

Table 5. Distribution of F – value between the inhibition efficiencies of various concentrations of catechol (0 ppm Zn^{2+}) and the inhibition efficiencies of catechol in presence of 10, 25, 50, 75, 100 ppm Zn^{2+}.

Zn^{2+} (ppm)	Source of variance	Sum of squares	Degrees of freedom	Mean square	F	Level of significance
10	Between	300	1	300	1.09	P < 0.05
	Within	2197.68	8	274.71		
25	Between	2.16	1	2.16	0.005	P < 0.05
	Within	3386.15	8	423.27	64.79	
50	Between	3267	1	3267	1.74	P < 0.05
	Within	1877.68	8	234.71		
75	Between	3137.64	1	3137.64	7.64	P < 0.05
	Within	1812.83	8	410.71		
100	Between	5292	1	5292	20.72	P < 0.05
	Within	2043.68	8	255.46		

out [27-28]. The results are given in Table 5. As can be seen, the influence of 10, 25, 50, 75 and 100 ppm of Zn^{2+} on the inhibition efficiencies of 50, 100, 150, 200, 250 ppm of catechol is investigated. The obtained F-value of 1.09 for 10 ppm Zn^{2+}, 0.005 for 25 ppm Zn^{2+} and 1.74 for 50 ppm Zn^{2+} is not statistically significant, since it is less than the critical F-value of 5.32 for 1.8 degrees of freedom at a 0.05 level of significance. Therefore, it is concluded that the influence of 10 ppm Zn^{2+}, 25 ppm Zn^{2+} and 50 ppm Zn^{2+} on the inhibition efficiencies of various concentrations of catechol is not statistically significant.

The obtained F-value of 7.64 for 75 ppm of Zn^{2+} and 20.72 for 100 ppm Zn^{2+} is statistically significant, since it is greater than the critical F-value of 5.32 for 1.8 degrees of freedom at a 0.05 level of significance. Therefore, it is concluded that the influence of 75 ppm Zn^{2+} and 100 ppm Zn^{2+} on the inhibition efficiencies of various concentrations of catechol is statistically significant.

The potentiodynamic polarization curves of carbon steel immersed in ground water in the absence and presence of inhibitors are shown in Fig.1. The corrosion parameters such as corrosion potential (E_{corr}), corrosion current (I_{corr}), Tafel (LPR) are given in Table 6. When carbon steel was immersed in ground water, the corrosion potential slopes (b_a, b_c) and linear polarization resistance was -807 mV *vs* SCE. In presence of the inhibitors (100 ppm of catechol and 100 ppm of Zn^{2+}), the corrosion potential shifted to the anodic side (-690 mV *vs* SCE). The electron transfer became more difficult, since the metal surface has become nobler. This fact was supported by the observation that the LPR value increased from 4.95×10^4 Ohm cm^2 to 1.069×10^5 Ohm cm^2 and the corrosion current

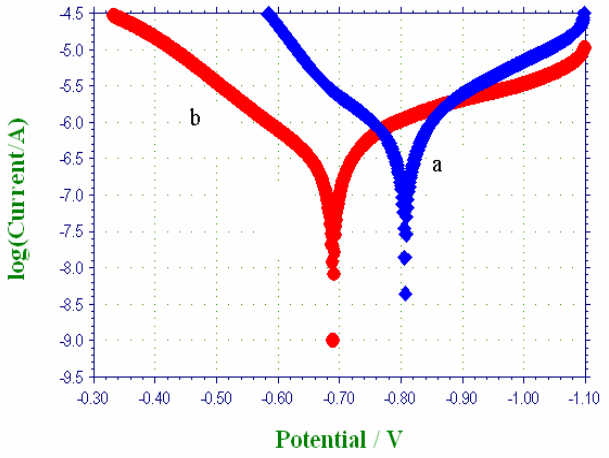

Fig. 1. Polarization curves of carbon steel immersed in test solution. (a) Ground water (b) Ground water containing 100 ppm of catechol and Zn^{2+}.

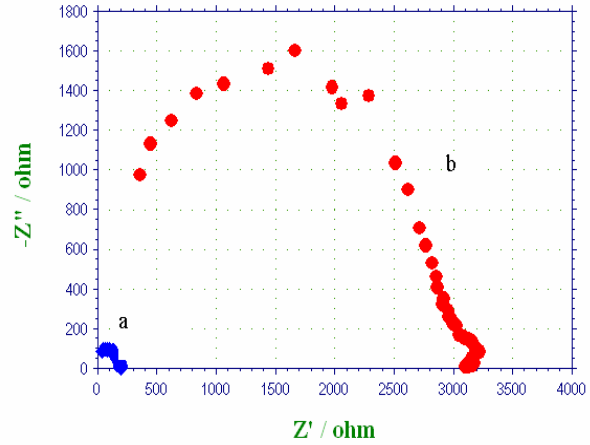

Fig.2. AC impedance spectra of carbon steel immersed in test solution.(a) Ground water (b) Ground water containing 100 ppm of catechol and Zn^{2+}

decreased from 7.157×10^{-7} A/cm^2 to 3.965×10^{-7} A/cm^2. These results suggest that a protective film (probably of Fe^{2+}-catechol complex) is formed on the metal surface, thus preventing the electron transfer process and corrosion [29].

Table 6. Corrosion parameters of carbon steel immersed in ground water in the absence and presence of inhibitors obtained by potentiodynamic polarization method. Inhibitor system: catechol + Zn^{2+}.

System	$E_{corr,}$ vs. SCE mV	b_c mV/ decade	b_a mV/ decade	LPR Ω cm^2	I_{corr} A/0.00785 cm^2	IE %
Ground water	-807	196.9	139.2	4.95×10^4	7.157×10^{-7}	80.5
Ground water + 100 ppm of catechol + 100 ppm of Zn^{2+}	-690	260.1	156	1.069×10^5	3.965×10^{-7}	

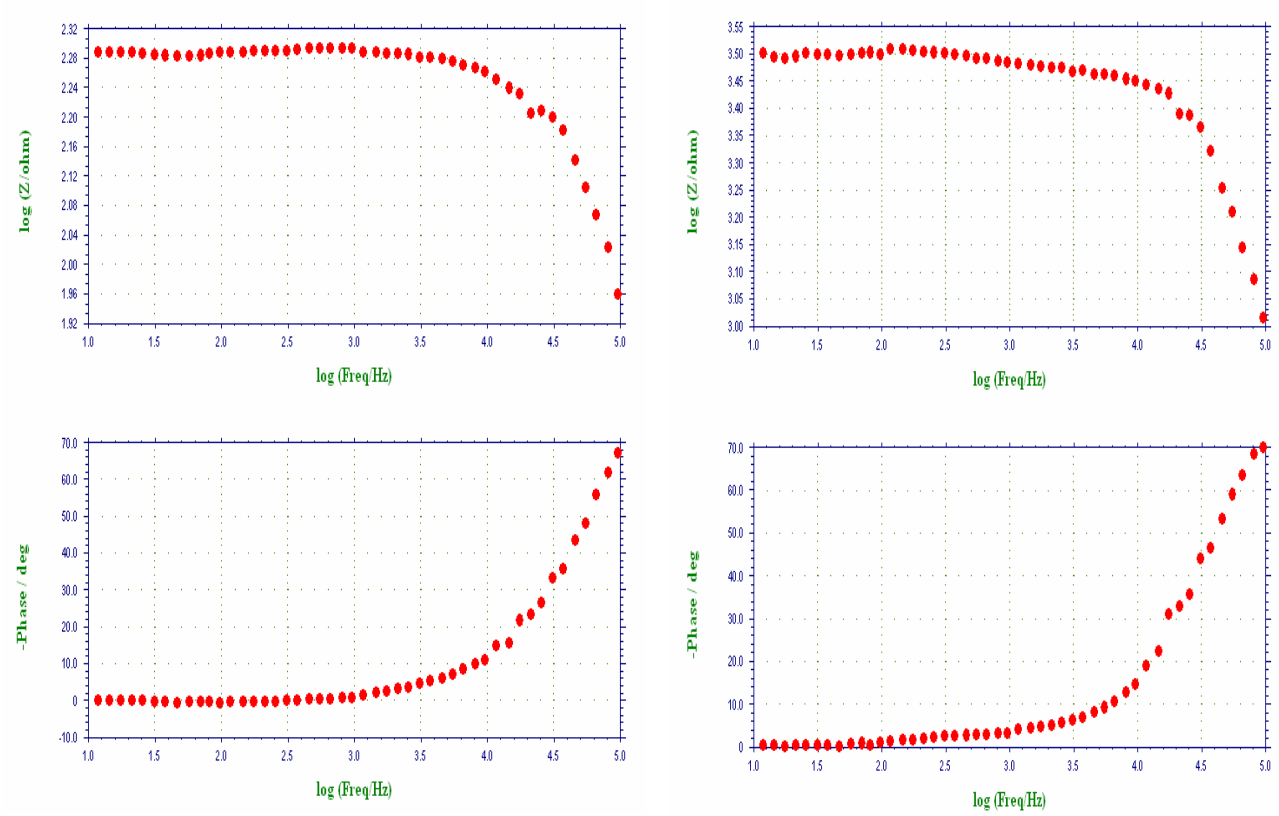

Fig. 3. Analysis of Bode plot. (a)The Bode plot of carbon steel immersed in Ground water. b) The Bode plot of carbon steel immersed in Ground water containing 100 ppm of catechol and Zn^{2+}.

The IE% calculated by the weight-loss method and by the polarization study slightly differed and this difference may be attributed to the change in surface state during polarization, which plays an important role in the adsorption process [30].

When carbon steel was immersed in ground water, the R_t value was found to be 162.23 Ohm cm^2. The C_{dl} value was 3.14×10^{-8} F/cm^2. Upon addition of 100 ppm of catechol and 100 ppm of Zn^{2+}, the R_t value increased to 2869.0 Ohm cm^2. This pointed to the formation of a protective film on the metal surface, probably by deposition of Zn

$$Fe \rightarrow Fe^{2+} + 2e^-$$
$$Zn^{2+} + 2e^- \rightarrow Zn$$

on the metal surface, which prevented further corrosion.

The prevention of corrosion was further supported by the decrease in the double layer capacitance value (from 3.14×10^{-8} F/cm^2 to 1.78×10^{-9} F/cm^2) **is given in Table 7**. The polarization study rapidly measures the rate of electron transfer reactions, while AC impedance spectra shown in Fig.2 record the prolonged formation of a protective film on the metal surface. This behaviour means that the film obtained acts as a barrier to the corrosion process and clearly proves the film formation and adsorption of inhibitor on the metal surface [31].

Table 7. AC- Impedance parameter of carbon steel immersed in the presence of inhibitors obtained from AC impedance spectra.

System	R_t Ω cm^2	C_{dl} F/0.00785 cm^2	Impedance log (z/ Ω)	IE %
Ground water	162.23	3.14×10^{-8}	2.287	
Ground water + 100 ppm of catechol + 100 ppm of Zn^{2+}	2869	1.78×10^{-9}	3.496	94.3

The corresponding Bode plots are shown in Fig. 3a. It is observed that in the absence of inhibitors the real impedance value (log Z) is 2.28 Ohm. In the presence of inhibitors this value increases to 3.49 (see Fig. 3b). The increase in the impedance value suggests a high protective efficiency of this system. The plot obtained in the presence of inhibitor is characterized by a single time constant. This indicates the formation of a homogeneous film on the metal surface [32,33].

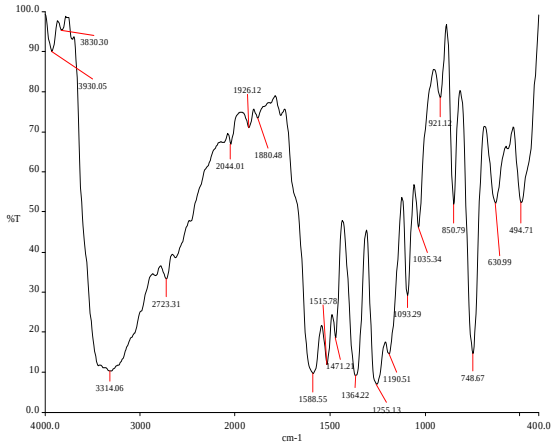

Fig. 4a. The FTIR spectra of pure catechol

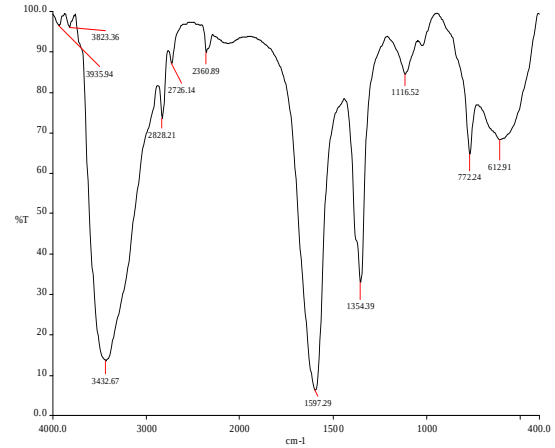

Fig.4b. The FTIR spectra of the film formed on the surface of carbon steel after immersed in ground water containing catechol (100 ppm) and Zn^{2+}(100 ppm).

The FTIR spectrum of pure catechol (KBr) is shown in Fig.4a. The OH stretching frequency appeared at 3314 cm^{-1}. The C=C ring stretching frequency appeared at 1588.55 cm^{-1}. The FTIR spectrum of the film formed on the metal surface after immersion in the solution containing ground water, 100 ppm of catechol and 100 ppm of Zn^{2+} is shown in Fig 4b. It is seen that the OH stretching frequency has shifted from 3314 to 3432 cm^{-1} and the C=C ring stretching frequency has shifted from 1588.55 to 1597 cm^{-1} [34]. These observations indicated that catechol coordination to Fe^{2+} through the oxygen atoms of the phenolic group and the π electrons of benzene ring resulted in the formation of a Fe^{2+}-catechol complex at the anodic sites of the metal surface. The peak at 1354 cm^{-1} was due to $Zn(OH)_2$ formed on the cathodic sites of the metal surface [35].

The SEM images (magnification 2000×) of carbon steel specimens immersed in ground water for 1 day in the absence and presence of inhibitor system are shown in Fig. 5(a-c) respectively.

The SEM micrograph of polished carbon steel surface (control) in Fig. 5a shows the smooth surface of the metal with no corrosion products on the metal surface. On the SEM micrograph of carbon steel surface immersed in ground water (Fig. 5b) rough metal surface is seen which indicates the corrosion of carbon steel in ground water. Fig. 5c reveals that in the presence of 100 ppm of catechol and 100 ppm of Zn^{2+} in the water, the surface coverage increases, which in turn results in the formation of an insoluble complex on the surface of the metal (catechol-Zn^{2+} inhibitor complex) and the surface is covered by a thin layer of inhibitors which effectively controls the dissolution of carbon steel [36].

Mechanism of corrosion inhibition

The results of the weight-loss study revealed that the formulation consisting of 100 ppm of catechol and 100 ppm of Zn^{2+} offers an inhibition

efficiency of 90%. Results of the polarization study showed that this formulation acts as an anodic inhibitor. The FTIR spectra showed that Fe^{2+}-catechol complex and $Zn(OH)_2$ are present on the inhibited metal surface.

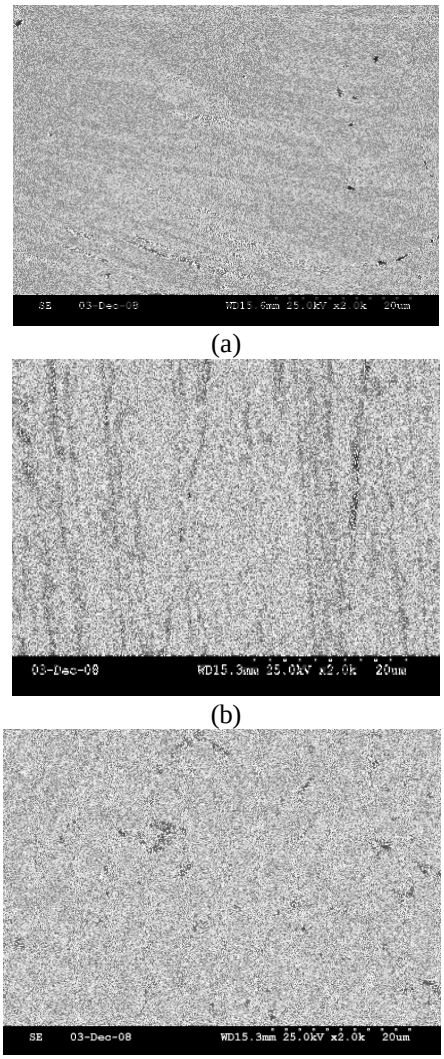

Fig. 5. SEM micrographs of : (a)Carbon steel (control); Magnification-X 2000; (b) Carbon steel immersed in well water; Magnification-X 2000; (c) Carbon steel immersed in well water containing catechol (100 ppm) + Zn^{2+}(100 ppm); Magnification–X 2000.

In order to explain all observations in a holistic way, a suitable mechanism of corrosion inhibition was proposed as follows.

When a carbon steel specimen is immersed in the neutral aqueous environment, the anodic reaction is:

$$Fe \rightarrow Fe^{2+} + 2e^-$$

and the cathodic reaction is

$$2H_2O + O_2 + 4e^- \rightarrow 4OH^-$$

- When the formulation consisting of 100 ppm of catechol and 100 ppm of Zn^{2+} was prepared, the Zn^{2+} - catechol complex was formed in solution.
- When carbon steel was immersed in this solution, there was diffusion of Zn^{2+} -catechol complex towards the metal surface.
- On the metal surface, it was converted to Fe^{2+}-catechol complex. Zn^{2+} was released and $Zn(OH)_2$ was formed:

$$Zn^{2+} \text{ - catechol} + Fe^{2+} \rightarrow Fe^{2+}\text{-catechol} + Zn^{2+}$$

$$Zn^{2+} + 2OH^- \rightarrow Zn(OH)_2 \downarrow$$

- Thus the protective film consists of Fe^{2+}-catechol complex formed on anodic sites of the metal surface and is more stable than the Zn^{2+}-catechol complex [37-38] and the $Zn(OH)_2$ precipitate in the local cathodic regions.

4. CONCLUSIONS

The inhibition efficiency of the catechol - Zn^{2+} system in controlling the corrosion of carbon steel in ground water was evaluated by the weight-loss method. The present study leads to the following conclusions:

- Weight-loss study revealed that the formulation consisting of 100 ppm of catechol and 100 ppm of Zn^{2+} had 90% inhibition efficiency in controlling corrosion of carbon steel immersed in ground water.
- Synergism parameters suggested that a synergistic effect exists between catechol and Zn^{2+}.
- ANOVA test revealed that the synergistic effect of the above formulation is statistically significant.
- Polarization study revealed that this system acts as anodic inhibitor.
- AC impedance spectra (Bode plots) revealed that a protective layer is formed on the metal surface.

FTIR spectra revealed that the protective film consisted of Fe^{2+}-catechol complex and $Zn(OH)_2$.

REFERENCES

1. V. Trabanelli , Garaaiti, in: Fontana MG, Staehle RW Eds., Advances in Corrosion Science and Technology, Plenum Press, New York, 1970, p.147.
2. J. I. Bregmann, Corrosion Inhibitors, Macmillan PT, New York, 1963.
3. H. Kaesche, N.J. Hacherman, *Electrochem. Soc*., **105**, 191 (1958).
4. B. E. Blomgren, J. O' Bockriss, *J. Phys. Chem.*, **63**, 1475 (1959).
5. S. L. Granese, *Corros Sci*., **44**, 322 (1987).
6. T. Notoya, *Corros. Eng. Jpn*., **27**, 661 (1978) .
7. A. Chetouani, B. Hammouti, A.Aouniti, N. Benchat, T. Benhadda, *Progr Org Coat*., **45**, 805 (1957).
8. G. Banerjee, S.N. Malhotra, *Corrosion*, **48**, 10 (1992).

9. J. O' M. Bockriss, B. Yang, *J. Electrochem. Soc.*, 138, 2237 (1991).
10. S. Kertit, A. Elkholy, J. Aride, A. Srhiri, A. Ben Bachir, M. Etman, *J. Appl. Electrochem.*, **19**, 83 (1989).
11. B. Sathianandhu, K. Balakrishnan, N. Subramaniyan *Bras. Corros. J.*, **5**, 270 (1970).
12. J. Uhrea, K. Aramaki, *J. Electrochem. Soc.*, **138**, 2237 (1991).
13. F. Zucchi, G. Trabanelli, G. Brunoro, *Corros. Sci.*, **33**, 1135 (1992).
14. J.K. Rodge, M.R. Muley, D.R. Kulkarni, M.N. Deshpande, *Asian J. Chem.*, **19**, 4745 (2007).
15. B. Muller, M. Shahid, G. Kinet, *Corrosion Sci.*, **41**, 1323 (1999).
16. S. Viswanathan, N. Haldar, *Indian J. Chem Technol.*, **14**, 501 (2007).
17. D.R. Kulkarni, M.R. Muley, J.K. Rodge, M.N. Deshpande, *Asian J. Chem.*, **19**, 3877 (2007).
18. H. Benita Sherine, A.J.A. Nasser, S. Rajendran, *J. Electrochem. Soc. India*, **58**, 30 (2009).
19. H. Benita Sherine, A.J.A. Nasser, S. Rajendran, *J. Electrochem. Soc. India*, **58**, 69 (2009).
20. H. Benita Sherine, A.J.A. Nasser, S. Rajendran, *Intern. J. Eng. Sci. Technol.*, **2**, 341 (2010).
21. S. Rajendran, S.M. Joany, B.V. Apparao, N. Palaniswamy, *Indian J. Chem. Technol.*, **9**, 197 (2002).
22. S. Rajendran, A.J. Amalraj, M.J. Joice, N. Anthony, D. C. Trivedi, M. Sundaravadivelu, *Corrosion Revs*, **22**, 233 (2004).
23. S. Rajendran, B.V. Apparao, N. Palaniswamy, *J. Electrochem. Soc. India*, **47**, 43 (1998).
24. S.A. Kanimozhi, S. Rajendran, *Int. J. Electrochem. Sci.*, **4**, (2009).
25. S. Rajendran, S. Shanmugapriya, T. Rajalakshmi, A.J. Amalraj, *Corrosion*, **61**, 685 (2005).
26. K. Anuradha, R. Vimala, B. Narayanasamy, A. Arockia Selvi, S. Raji, *Chem. Eng. Commun.*,**195**, 352 (2005).
27. S. Rajendran, A. Raji, J. Arockia Selvi, A. Rosaly, S. Thangasamy, *J. Mat. Edu.*, **29**, 245 (2007).
28. S. Rajendran, A. Raji, J.A. Selvi, A. Rosaly, S. Thangasamy, *EDUTRACKS*, **6**, 30 (2007).
29. S. Rajendran, M. Kanagamani, M. Sivakalaivani, J. Jeyasundari, B. Narayanasamy, K. Rajam, *ZASTITA MATERIJALA*, **49**, 4 (2008).
30. M.S. Morad, *J.Appl. Electrochem.*, **38**,1509 (2008).
31. S. S. Mahmoud, *J. Mater. Sci.*, **42**, 989 (2007) .
32. E. Kalman, B. Varhegyi, I. Felhosi, *J. Electrochem. Soc.*, **14**, 3357 (1994).
33. A. Bonnel, F. Dabosi, C. Deslovis, *J. Electrochem. Soc.*, **130**, 753 (1983).
34. R.M. Silverstein, G.C. Bassler, T.C. Morrill, Spectrometric Identification of Organic Compounds, John Wiley& Sons, 4th ed. 1981, pp. 120-121.
35. K. Nakamoto, Infrared and Raman Spectra of Inorganic and Coordination Compounds, Part B, Vth ed. Wiley Publications, 1997, p. 271.
36. T. Horvath, E. Kalman , *Russian J. Electrochem.*, **36**, 1085 (2000).
37. S. Rajendran, B.R. Earnest, J. Peter, A. Peter, P. Regis, A.J. Amalraj, M. Sundaravadivelu, *Trans. SAEST*, **38**, 11 (2003).
38. A. Nithya, S. Rajendran, *Bulg. Chem. Commun.*, 42 119 (2010).

ИНХБИРАЩО ДЕЙСТВИЕ НА СИСТЕМА КАТЕХОЛ-ЦИНК ПРИ КОНТРОЛИРАНЕ НА КОРОЗИЯТА НА ВЪГЛЕРОДНА СТОМАНА

Х. Бенита Шерин[1*], С. Фелси Сагая Мари[2], С. Раджендран[3]

[1,2] *Катедра по химия, Колеж Холи крос, Тирушираппали – 620 002, Тамилнаду, Индия*
[3] *Катедра по химия, Колеж на изкуствата ГТН, Диндигул – 624 005, Тамилнаду, Индия*

Получена на 17 декември 2010; Приета на 4 януари 2011

(Резюме)

Инхибиращата ефективност на инхибиторни системи, състоящи се от различни комбинации на катехол и йони на цинк, при конролиране на корозията на въглеродна стомана, потопена в подпочвена вода, е оценена по метода на загубата на тегло. 100 ppm от Zn^{2+}имат само 15% инхибиращата ефективност (ИЕ). При добавяне на 100 ppm катехол, ИЕ се увеличава до 90%. Използвани са метод на загубата на тегло, поляризационни изследвания и импедансни спектри. Природата на предпазния филм, образуван върху повърхността на метала, се анализира чрез инфрачервена спектроскопия с Фурие трансформация (FTIR). Беше установено, че предпазния филм се състои от комплекс Fe^{2+} - катехол. За оценка на синергичния ефект на инхибиторите са използвани параметри на синергизъм и дисперсионен анализ.

Bulgarian Chemical Communications, Volume 43, Number 4 (pp 552 –557) 2011

Characterization and application of activated carbon from biomass and coal wastes for naphthalene removal

B. Tsyntsarski, B. Petrova, T. Budinova, N. Petrov, L. Velasco, C.O. Ania

[1]*Institute of Organic Chemistry, Bulgarian Academy of Sciences, Sofia 1113, Acad.G. Bonchev str.,BL. 9, Bulgaria*
[2]*Instituto Nacional del Carbon, CSIC, Apartado 73, 33080, Oviedo, Spain*

Received January 20, 2011; Accepted February 25, 2011

Activated carbons were prepared from different waste materials (coal tar pitch and apricot stones) by pyrolysis in the presence of water vapor. The adsorption of naphthalene from aqueous solution at 298 K on the obtained activated carbons was studied. It was established that the adsorption capacity of the activated carbons depends on the surface area and porosity. It was found that naphthalene adsorption follows Langmuir isotherms. The adsorption capacity of activated carbon obtained from coal tar pitch/furfural was 18.75 mg/g and for activated carbon from apricot stones - 29.95 mg/g.

Keywords: coal tar pitch, furfural, apricot stones, adsorption, naphthalene.

1. INTRODUCTION

Solving the problems of pollution of ground water, which is the principal source of drinking water in most countries of the region, is an action of special importance that has already been globally discussed. Increasing the number of the existing water treatment facilities and construction of new facilities will be needed to improve drinking water quality because of human health concern. Industry generates a variety of pollutants which have negative impact on ecosystems and humans (toxicity, carcinogenic and mutagenic properties) [1, 2].

In order to ensure consistent protection of surface waters, the European Parliament and the Council of the European Union issued Directives on the environmental quality standards in the field of water policy. The European Environmental Agency (EEA) has included PAH compounds in the list of priority pollutants to be monitored in industrial effluents - Directive 60/EC and Directive 2008/105/EC [3,4].

Adsorption is a powerful technique for treating domestic and industrial pollutants. Activated porous carbons constitute one of the most important types of industrial carbons. The term activated carbon defines a group of carbon adsorbents with highly developed internal surface area and porosity. Activated carbons are extremely versatile adsorbents of industrial significance and they are used in a wide range of applications, principally related to the removal of undesired species, in order to effect purification or recovery of chemical constituents. Industrial waste is a potential low-cost source for preparation of activated carbons. Generally, industrial wastes are generated as a by-product of various industrial and agricultural production. Since these materials are locally available in large quantities, they are inexpensive. Such wastes are different agricultural by-products, wastes from coal conversion, different polymer wastes, etc. [5-12].

In our days the scientists worldwide are focused on searching of novel effective methods and new carbon materials for water purification from different toxic organic compounds. In this sense, a combination of various waste materials for production of activated carbons, for example wastes from coals and biomass materials, is suitable, and adsorption seems to be an attractive approach.

In this study naphthalene was adopted as a representative model compound of polycyclic aromatic hydrocarbons. Their static adsorption from aqueous solution on two types of adsorbents synthesized from different waste materials - coal and biomass (mixture of coal tar pitch/furfural and apricot stones) - was investigated.

2. MATERIALS AND METHODS

2.1. Materials

2.1.1. Preparation of activated carbon from coal tar pitch and furfural. A mixture of coal tar pitch and furfural (50:50 wt. %) was treated with concentrated H_2SO_4 (drops of H_2SO_4 were added under continuous stirring) at 120 ºC until

* To whom all correspondence should be sent:
E-mail: goriva@orgchm.bas.bg

solidification. The obtained solid product was heated up to 600 ºC in a covered silica crucible with a heating rate of 10 ºC min^{-1} in nitrogen atmosphere. The carbonized solid material was further submitted to water steam activation at 800°C for 1 h. The obtained carbon adsorbent is noted ACCF.

2.1.2. Preparation of activated carbon from apricot stones. Apricot stones (100 g) were heated in a laboratory installation in a flow of water vapor (120 ml/min) with a heating rate of 15°C/min to a final carbonization temperature of 800°C. The duration of treatment at the final temperature was 1 h. After treatment the sample was allowed to cool down. The obtained carbon adsorbent is noted ACA.

2.2. Porous and chemical structure analyses

The nanotexture of the synthesized carbon materials was characterized by N_2 adsorption at -196ºC, carried out in an automatic volumetric apparatus (ASAP 2020 from Micromeritics). Before the experiments, the samples were outgassed under vacuum at 120°C overnight. The isotherms were used to calculate specific surface area S_{BET}, total pore volume V_T, micropore volume $W_{o.}$ (using the DR formulism) [13]. The samples were further characterized by elemental analysis and chemical character of the surface was determined. A procedure based on Boehm's method [14] was used to quantify total and individual acidic oxygen groups on the adsorbent surface. The basic group content was determined by titration with HCl [15].

2.3. Adsorption measurements

Adsorption measurements of naphthalene from aqueous solutions on the carbon adsorbents were performed at ambient temperature in a stirred batch system, thermostatically controlled by an external circulating bath. Kinetic studies revealed that the adsorption equilibrium was established after 30 minutes. The determinations were performed by introducing 50 ml portions of naphthalene solution into a series of conical flasks containing 100 mg amount of adsorbent. After 2 h the content of the flasks was filtered through a microporous filter and naphthalene was determined spectrophotometrically on a UV spectrometer Pfaro 300 at a wavelength of 275.5 nm. The amount of adsorbed mass (q_e) per unit of adsorbent was evaluated from the equation:

$$q_e = V(C_o-C_e)/m ,$$

where V (ml) is the volume of the solution, m (g) - the mass of the adsorbent, and C_o and C_e are the initial and equilibrium concentrations of the aromatic compound in the liquid phase (mg l^{-1}), respectively.

A Langmuir isotherm study was carried out with initial concentrations of naphthalene: 5, 10, 15 and 20 mg/l and adsorbent mass of 100 mg/50 ml at pH 5.80.

3. RESULTS AND DISCUSSION

3.1. Chemical composition and textural properties of the activated carbons.

The chemical composition data for the raw precursor and the prepared activated carbons (AC) are presented in Table 1. The preliminary results from the elemental analysis showed that the activated carbons are suitable for adsorption of pollutants, probably due to their low ash content. Activation with water vapor leads to a considerable increase in the oxygen content of the activated carbon obtained from the coal tar pitch/furfural mixture, in comparison with the activation of apricot stones, where a considerable decrease in the oxygen content was established. Both activated carbons have similar contents of carbon, hydrogen, nitrogen and sulphur.

The elemental analysis data indicated that the amount of oxygen containing structures in the pitch is not high. It can be seen that the introduction of furfural in the process of preparing the AC leads to aproximately 6-fold increase in the oxygen content. As furfural inserts oxygen in the precursor, the higher amount of furfural increased the content of oxygen in the synthesized carbon and made it more alkaline.

Table 1. Chemical composition of coal tar pitch, apricot stones and synthesized activated carbons

Sample	Ash (wt.%)	Volatiles (wt.%,daf)	C (wt.%)	H (wt.%)	N (wt.%)	S (wt.%)	O (wt.%)
Coal tar pitch	-	-	90.90	4.95	0.90	0.50	2.75
ACCF	0.80	1.90	81.59	2.56	0.28	0.59	14.98
Apricot stones	0.20	80.60	51.50	6.30	0.20	0.10	41.90
ACA	2.01	3.70	89.50	2.40	0.90	0.80	6.40

Table 2. Textural parameters of activated carbons produced by apricot stones

Sample	Iodine adsorption, mg/g	Surface area, BET m^2/g	Pore volume, m^3/g			
			Vmicro	Vmeso	Vmacro	Vtot
ACCF	1100	678	0.236	0.121	0.031	0.388
ACA	925	960	0.500	0.110	0.040	0.650

Previous studies carried out in our research group have shown that the composition of agricultural by-products has a strong influence on the final porous and chemical features of the solid products obtained by pyrolysis and subsequent activation [6]. It was found that the high lignin content favors the development of a macroporous structure, whereas cellulose yields predominantly microporous materials. Analysis of the chemical composition of the initial waste material showed that apricot stones, used as a carbon source, are mainly composed of cellulose and hemicellulose (30 wt % and 28 wt %, respectively), lignin (30 wt %) and a small amount of lipids (12 wt %), which makes this material suitable for preparation of carbons with well-developed microstructure.

In this work, coal tar pitch was selected as another carbon precursor. Earlier studies carried out in our research group have shown that furfural resin is a suitable oxygen-containing raw material for the production of carbon adsorbents with a large number of oxygen-containing groups on the surface [16]. The addition of furfural to the coal tar pitch used in the precursor mixture aimed to incorporate reactive structures in the carbon matrix, which induce polymerization and polycondensation reactions – this facilitates the solidification of the mixture. The resulting solid product was carbonized and submitted to steam activation to produce a suitable porous adsorbent.

Despite the large oxygen content, the synthesized carbon displays a strong alkaline character, as inferred from the pH value (Table 3).

The nitrogen adsorption isotherm of the activated carbons obtained from coal tar pitch/furfural and apricot stones are presented on Fig.1. The part of the isotherm in the range of the relatively lower pressures (a steep increase with a tendency for saturation) is typical for microporous adsorbents. The N_2 adsorption isotherm obtained corresponds to the IV type according to Brunauer *et al*. [15] (low pressure). Type IV isotherms are obtained for solids containing pores in the mesopore range. The shape of a type IV isotherm follows the same path as the type II at lower pressures. These adsorption isotherms have led to the development of the theory of capillary condensation. Broadly speaking, it is assumed that in the initial part of the isotherm the adsorption is restricted to a thin layer on the walls of the pores until capillary condensation begins in the smallest pores [15].

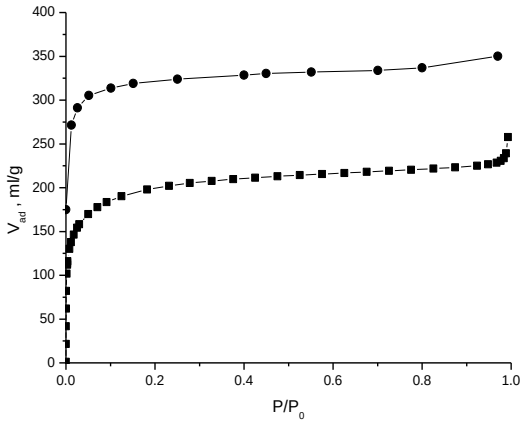

Fig. 1. N_2 adsorption isotherms at -196 ºC of the studied carbons (■ -activated carbon from coal tar pitch/furfural; ● -activated carbon from apricot stones).

Table 2 compares the porosity characteristics of activated carbons obtained from coal tar pitch/furfural and apricot stones. Both activated carbons possess close values of BET surface area.

The sample of activated carbon prepared from apricot stones has higher BET surface area and larger total pore volume with significant prevalence of the micropores, in comparison with activated carbon prepared from coal tar pitch and furfural.

In a previous work [17] about the effect of the ratio furfural:coal tar pitch in the carbon precursor, we have observed that the furfural content has a strong effect on the porosity of the resulting carbons. Low proportion of furfural give rise to activated carbons with a narrow microporosity, which is gradually opened in favor of large micropores and mesopores as the furfural content rises. Notwithstanding, the carbon yield also sharply decreases upon rising the furfural content, due to the reactivity of the precursor mixture. In this regard, if the sample ACCF is prepared with a low proportion of furfural in the precursor mixture (45 wt. %); it is characterized by a moderate value of BET surface area and well developed microporosity (Table 3). These porous features should be very suitable for the removal of aromatics from aqueous phase.

Table 3. Nature of the oxygen groups of the prepared carbons, obtained by Boehm titration

Sample	pH	Acidic groups (meq.g^{-1})				Basic groups (meq.g^{-1})
		Carboxylic	Lactonic	Phenolic	Carbonyl	Hydroxyl
ACCF	8.1	0.019	0.011	0.026	0.550	0.592
ACA	8.2	0.120	0.090	0.200	0.990	1.240

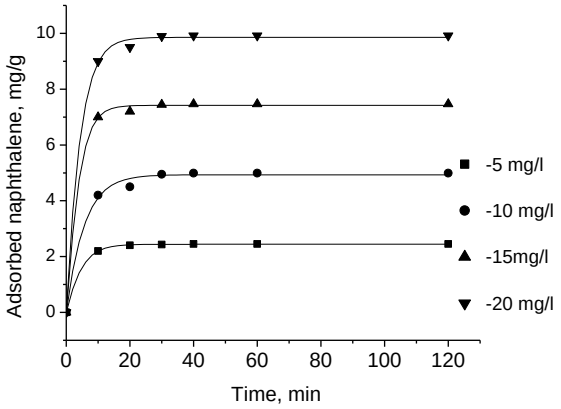

Fig. 2. Effect of contact time on adsorption of naphthalene on activated carbon from apricot stones. Conditions: carbon concentration: 100mg/50 ml; Naphthalene concentrations: 5mg/l(■) ; 10mg/l(●) ; 15mg/l(▲) ; 20 mg/l (▼).

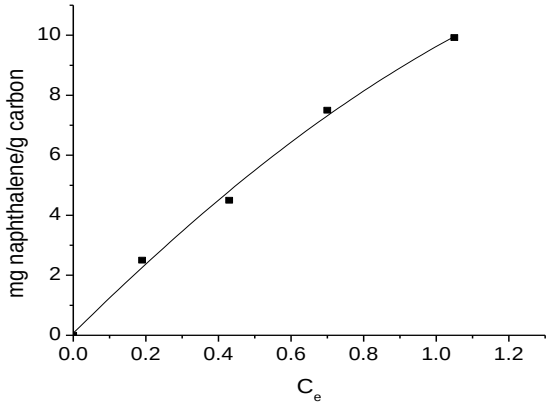

Fig. 3. Langmuir plots for adsorption of naphthalene on both activated carbons: (■- carbon from coal tar pitch/furfural; ● - carbon from apricot stones.

3.2. Surface functionalities of the activated carbons

The data of Table 3 show the nature of the surface functionalities created upon pyrolysis of the carbons. Analysis of the chemical composition of ACCF showed that along with the prevailing content of aromatic structures in the pitch, the resulting material has a relatively large oxygen content (Table 1). This corroborates the fact that inserting oxygen in the carbon precursor (i.e. furfural) leads to the formation of oxygen containing structures on the surface of the final product. Despite the large amount of oxygen, the synthesized carbon displayed strong alkaline character, as inferred from the pH value. It was found that activated from apricot stones has a two times higher content of oxygen, carbonyl and basic groups than activated carbon from coal tar/pitch, despite the two-fold higher content of oxygen in the latter. This implies that the greater part of oxygen is inserted in the non-functional oxygen structures, which are obviously formed during the process of pyrolysis. The obtained data showed that the surface chemistry of carbons ACCF and ACA is characterized by carbonyl and phenolic functionalities, which render a basic character to the adsorbent.

3.3. Adsorption of naphthalene from aqueous solution

Initially, the adsorption kinetics of naphthalene on the studied carbons was evaluated in order to assess the time needed to attain equilibrium before determining the maximum adsorption capacity of each adsorbent. The kinetics of adsorption of naphthalene on both activated carbons ACA and ACCF from aqueous solution in concentrations ranging from 15 to 20 g/l are shown in Figure 2.

Equilibrium was attained for less than 1 h. The kinetic curves are smooth and continuous, and they lead to saturation, which suggests the possibility of the formation of monolayer coverage of naphthalene on the surface of adsorbent.

The Langmuir model [18] was tested and proved to fit the experimental data. The linear plot of the isotherm of the equation is an obligatory condition for the proper application of the theory of monomolecular adsorption. The linear plot of C_e/q_e *versus* C_e in Fig. 3 shows that the description of the adsorption of naphthalene on both adsorbents by the Langmuir isotherm model is satisfactory. Q_o and b were determined from the slope and intercept of the plot, respectively. The adsorption capacity of the coal/furfural adsorbent was 18.75 mg/g and that for the activated carbon from apricot stones - 29.55 mg/g. The estimated intensity of the adsorption parameter b varies from 0.4790 to 0.8735 (i.e.

between 0 and 1) [19], which implies favorable adsorption of naphthalene on the prepared carbons. For both adsorbents, excellent correlation coefficients were obtained when the data were fitted to the Langmuir theory. The Langmuir theory (1918) [20] is based on the assumption that all adsorption sites are equally "active", the surface is energetically homogeneous and a monolayer surface coverage is formed with no interactions between the adsorbed molecules. Hence, in aqueous media, the very good agreement with Langmuir equation indicated that the saturation limit was attained, which was also supported by the specific shape of the isotherms (Figure 4).

Figure 4 presents the isotherm of naphthalene in water – it has a typical L type shape (concave curvature at low concentrations) according to the Giles classification [21], which is characteristic for systems where the adsorbate has high affinity towards the adsorbent.

It is well known that the key factors influencing the adsorption capacity on activated carbons are the pore texture, surface chemistry and mineral content. The adsorption capacity of carbon materials is not connected in simple way with their surface area and porosity – the relation is complex. Generally the adsorption capacity depends on the access of the organic molecules to the inner surface of the adsorbents, which depends on their size. In our study, a good relation between the adsorption capacity and the porous and surface characteristics of the carbons was established. The activated carbon from apricot stones showed a higher adsorption capacity than that from coal tar pitch/furfural, because of its higher surface area

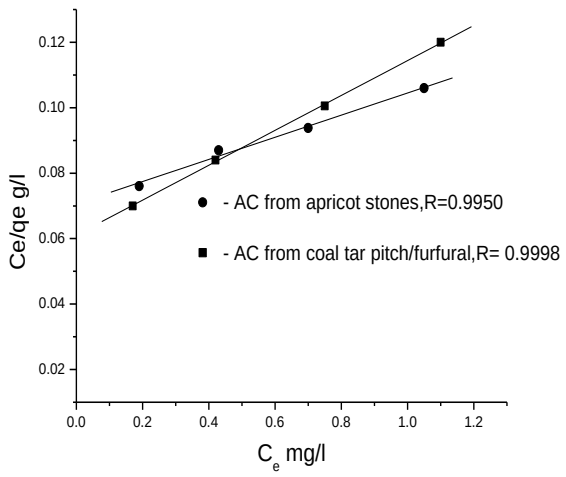

Fig. 4. Langmuir plots for adsorption of naphthalene on both activated carbons: Conditions: naphthalene concentrations, 5-20mg/l; treatment time - 120 min; carbon concentration - 100mg/50ml.

(BET), significant total pore and micropore volumes, as well as higher content of carbonyl and basic groups.

4. CONCLUSIONS

The present study shows that wastes from apricot stones and mixtures of coal tar pitch and furfural can be effectively used as raw materials for the preparation of activated carbons for removal of naphthalene. The carbons were characterized and utilized for the removal of naphthalene from water in the concentration range 5-20 mg/g. The maximum adsorption capacities were 18.75 mg/g for activated carbon from coal tar pitch/furfural and 29.95 mg/g for activated carbon from apricot stones. These results were found to be highly promising. It was established that the increase in adsorption affinity depends on both textural parameters and surface chemistry.

Acknowledgement:*We gratefully appreciate the funding by the Bulgarian Ministry of Education Youth an, Science (contract No Do 02-222/17.12.2008).*

REFERENCES

1. 1.P. T. Williams, *J. Inst. Energy*, **63**, 23 (1990) .
2. C. O. Ania, B. Cabal, C. Pevida , A. Arenillas, J. B. Parra, E. Rubiera, *Water Research*, **41**, 333 (2007).
3. Directive European 2000/60/EC, EU Water Framework Directive. *Off.J.* 327, 2000.
4. Directive 2008/105/EC.Environmental Quality Standards for Priority Substances and Certain Other Pollutants, 16 December 2008.
5. T.J. Bandosz, Activated carbon surface in environmental remediation, in: T. J. Bandosz (Ed.), Interface Science and Technology Series, Elsevier, New York, 2006.
6. D. Savova, E. Apak E. Ekinci, F. Yardim, N. Petrov,T. Budinova, M. Razvigorova, V. Minkova. *Biomass & Bioenergy*, **21**, 133 (2001).
7. N. Petrov, T. Budinova, M. Razvigorova, J. Parra, P. Galiatsatou, Conversion of olive wastes to volatiles and carbon adsorbents, *Biomass & Bioenergy*, **32**, 1303 (2008).
8. L.R. Radovic, L.R. Moreno-Castilla, C.J. Rivera Utrila, Carbon materials as adsorbent in aqueous solutions, In: Radovic, L. R. (Ed.) Chemistry and Physics of Carbon, vol.27, pp.227-406, Dekker, New York (2000).
9. C. Moreno-Castilla, J. Rivera-Utrilla, M.V. Lopez-Ramon, F. Carrasco-Marín, *Carbon*, 33, 845-851 (1995).
10. N. Petrov, T. Budinova, *Chemie Ingenieur Technik*, **64,** 64 (1992).
11. H. Marsh, H. Rodriguez-Reinoso, in: Activated Carbon, Elsevier Science 2006, Oxford, UK.

12. A.S. Mestre, J. Pires, J.M.F. Nogueira, J. B. Parra, A.P. Carvalho, C.O. Ania, *Bioresource Technol.* **100**, 1720 (2009).
13. F. Rouquerol, J. Rouquerol, K. Sing, in: Adsorption by powders and porous solids. Principles, methodology and applications, Academic Press, London (1999).
14. H.P. Boehm, in: Adv. Catal. Rel. Subj., vol.16, D.D. Eley, H. Pines, P.B. Weisz (Eds.), Academic Press, New York, pp.179-274 (1966).
15. E. Papier, S. Li., J.B. Donnet, *Carbon*, **25**, 243 (1987).
16. N. Petrov, T. Budinova, M. Razvigorova, E. Ekinci, F. Yardim, V. Minkova, *Carbon*, **38**, 2069 (2000).
17. B. Petrova, B. Tsyntsarski, T. Budinova, N. Petrov, C.O. Ania, J.B. Parra, M. Mladenov, P. Tzvetkov, *Fuel Process. Technol.*, **91**, 1710 (2010).
18. S. J. Gregg, K.S. W. Sing, in: Adsorption, Surface Area and Porosity, Academic Press, London, 1982.
19. D.O. Cooney, Adsorption Design for Waste Water Treatment. Lewis Publishers, CRS Press LLC, Boca Raton, 1999.
20. I. Langmuir, *J. Am. Chem. Soc*., **40**, 361 (1918).
21. C.H. Giles, T.H. MacEwan, S.N. Nakhwa, D.J. Smith, *Chemical Society*, 3973 (1960).

ОХАРАКТЕРИЗИРАНЕ И ПРИЛОЖЕНИЕ НА АКТИВЕН ВЪГЛЕН ОТ БИОМАСА И ВЪГЛИЩНИ ОТПАДЪЦИ ЗА ИЗВЛИЧАНЕ НА НАФТАЛИН

Б. Цинцарски, Б. Петрова, Т. Будинова, Н. Петров, Л. Веласко, К.О. Аниа
Институт по органична химия с Център по фитохимия, Българска академия на науките,
ул. Акад. Г. Бончев, бл. 9, София 1113, България
Национален институт по въглерода, Висш съвет за научни изследвания, Апартадо 73, 33080, Овиедо, Испания

Постъпила на 20 януари, 2011 г.; приета на 25 февруари 2011 г.

(Резюме)

Получени са активни въглени от различни отпадни материали (каменовъглен пек и кайсиеви костилки) чрез пиролиз в присъствие на водна пара. Беше изследвана адсорбцията на нафталин от водни разтвори при 298 K. Беше установено, че адсорбционният капацитет на активните въглени зависи от тяхната специфичната повърхност и порьозност. Беше установено, че адсорбцията на нафталин следва изотермите на Лангмюир. Адсорбционният капацитет та активният въглен получен от къменовъглен пек и фурфурол 18.75 mg/g, а за активния въглен от кайсиеви костилки - 29.95 mg/g.

Bulgarian Chemical Communications, Volume 43, Number 4 (pp 558 – 562) 2011

X-ray powder diffractometry and NMR studies of europium-dibenzoylmethane complexes

J. Ts. Zaharieva, M. M. Milanova, N. Vasilev[1], B. Morgenstern[2], D. S. Todorovsky*

Faculty of Chemistry, University of Sofia, 1, J. Bourchier Blvd., Sofia 1164, Bulgaria
[1] Institute of Organic Chemistry, Bulgarian Academy of Sciences,Acad. G. Bonchev Str., Bl. 9, Sofia 1113, Bulgaria
[2]Chair of Inorganic Chemistry, Saarland University, 66123 Saarbrücken, Germany

Received November 8, 2010; Accepted January 12, 2011

The X-ray powder diffractogram of the europium complex $Eu(DBM)_3$ (DBM – dibenzoylmethane) is reported for the first time. It is shown that the mixed-ligand complex $Eu(DBM)_3$.dpp (dpp - 1,4-diphenyl-1,10-phenanthroline) is X-ray amorphous. The ^1H and ^{13}C NMR spectra of $Eu(DBM)_3$, $Eu(DBM)_3$.phen (phen – 1,10-phenanthroline) and $Eu(DBM)_3$.dpp are interpreted and their applicability as a tool for evaluation of the stoichiometry of the complexes, the content of water and the completeness of the synthetic reaction is shown.

Key words: europium complexes, ^1H, ^{13}C NMR spectroscopy, X-ray diffractometry.

1. INTRODUCTION

Due to their fluorescent properties, the complexes of lanthanides (Ln) with β- diketones (incl. dibenzoylmethane, HDBM) have a lot of applications [1] as active components of organic LED, laser materials, NMR shift reagents, luminescent labels in biomedical investigations, optical sensors, promising materials for high-density recordable optical materials, etc. Europium β-diketonates are distinguished due to their narrow emission bands resulting from the electron transition between 4f levels. The organic components of the complexes, efficient photon absorbers, play the role of "antenna", transferring the energy to the $^5D_0$ long-lived visible light emitted state of the metal ion, thus giving significant advantage of Eu(III) when used as spectroscopic probe [1].

Recently the chemistry and application of the lanthanide diketonates have been object of the reviews [2, 3]. Some peculiarities of the lanthanide dibenzoylmethanates synthesis have been discussed in [4]. The literature data on their crystal structure are limited due to the difficulties to be obtained in crystal state. Some β-diketonates cannot be prepared in such a state even if they are produced by a solid state reaction [5]. Results from X-ray crystal structure determination are published for the mixed-ligand, DBM-containing complex $Eu(NO_3)(DBM)_2(TBPO)_2$, where TBPO – triphenylphosphine oxide [1]. Tetrakis-complexes can be prepared relatively easier in crystal state. The structure of tetrakis (dibenzoylmethanato) europates has been studied in relation to triboluminescense phenomena observed with some of them. Crystals have been prepared by the Hurt's method [6] (for example by the reaction of $EuCl_3$ and dibenzoylmethane with morphine in absolute ethanol [7]). As a counter ion triethylammonium [7-9], dimethylbenzyl ammonium [10-12], 2-hydroxyethylammonium and pyrrolidinium [12] were used (the structure of the compounds with the two latter ions is not reported). Recently, the structure of tetrabutylammoniumtetrakis(dibenzoylmethanato) europium(III)]/dimethyl sulfoxide (1:1) has been reported [13].

However, to our best knowledge, the only published X-ray powder diffraction data (without exact values of interplanar distances and relative intensities) for complexes of the type $Ln(DBM)_3$ (Ln–lanthanides) are those for La- and Tb-dibenzoylmethanates [5].

The first ^1H and ^{13}C NMR data for anhydrous tris(dibenzoylmethanido)(o-phenanthroline)-europium(III) complexes are reported in [14] in rather general form. No spectra, neither detailed assignment of the shifts is given. Data on $Eu(DBM)_3$ and DBM-4,7-diphenyl-1,10-phenanthroline are not available.

In the present paper the results from X-ray powder diffractometry and ^1H and ^{13}C NMR spectroscopy observations of $Eu(DBM)_3$ and of

* To whom all correspondence should be sent:
E-mail: nhdt@wmail.chem.uni-sofia.bg

complexes of the type $Eu(DBM)_3.Q$ (Q - 1,10-phenanthroline /Phen/ or 4,7-diphenyl-1,10-phenanthroline /dpp/) are reported.

2. EXPERIMENTAL

Materials

HDBM (purum, > 98 %, Fluka), 1,10-phenanthroline (phen, 99 %) and 4,7-diphenyl-1,10-phenanthroline (dpp, >98 %), both from Alfa Aesar and $EuCl_3.6H_2O$ (>99 %, Fluka) as starting materials and ethanol (> 96 %) as a solvent were used for complexes production.

Complexes preparation

$Eu(DBM)_3$ was prepared by the method proposed in [15]. To 48 cm^3 of an ethanol solution containing 6 mmol HDBM, 12 cm^3 0.5 M NaOH and 10 cm^3 aqueous solution containing 2 mmol $EuCl_3$ were added. The solution was boiled at reflux (60 ^oC) and stirred for 4 h. The formed crystals were filtered and dried at 110 ^oC for 7 h under vacuum and were stored in a vacuum dessicator. The content of H and C was determined by means of the elemental analyzer Vario EL III V5.018 and for a product stored for 2 months, the following percent content was found: H 4.44, C 65.19; calculated for $Eu(DBM)_3$: H 4.40, C 65.53.

$Eu(DBM)_3$.phen and $Eu(DBM)_3$.dpp were synthesized by the method [16]. Saturated ethanol solutions of $EuCl_3$ and of DBM were mixed and a 0.5 M aqueous solution of NaOH was added adjusting DBM:$EuCl_3$ mole ratio = 3 and pH = 6. The solution was stirred at ambient conditions for 4 h; the crystals formed were filtered, washed with absolute ethanol and dried at room temperature. Ethanol solution of 1,10-phenanthroline or 4,7-diphenyl-1,10-phenanthroline was added to the crystals, the suspension was stirred for 4 h, filtered, the separated crystals were washed with absolute ethanol, and dried in a desiccator over silica gel at reduced pressure.

X-ray diffractometry

The X-ray powder diffractograms were taken on a powder diffractometer Siemens D500 at CuK_α, 40 kV, 2θ step 0.02°/2s.

NMR spectroscopy

^1H and ^{13}C NMR spectra of the complexes were recorded using a Bruker DRX Avance 400 MHz NMR spectrometer (resonance frequencies: 400.13 MHz for ^1H and 100.6 MHz for $^{13}C\{^1H\}$). Chemical shifts were given in ppm relative to tetramethylsilane (dimethylformamid-d_7, DMF) as internal standard (δ = 0 ppm) or on a Bruker Avance DRX250 instrument in CD_3Cl solution. The spectra were referred to the solvent signal. The assignment of the ^1H and ^{13}C spectra was accomplished by measurement of DEPT-135 and 2D inverse detected heteronuclear (C-H) correlation (HSQC for DRX250 or HMQC for the DRX400).

$Eu(DBM)_3$: ^1H NMR (400.13 MHz, DMF-d_7, 21° C): δ = 2.35(s, 1H, 2-CH), 5.55(d, J=7.2Hz, 4H, o-Ph), 6.65(t, J=7.2Hz, 4H, m-Ph), 6.77(t, J=7.2Hz, 2H, p-Ph). ^{13}C NMR (100.6 MHz, DMF-d_7, 21°C): δ = 58.7(2-CH), 94.1(i-Ph), 124.4(o-Ph), 125.2(m-Ph), 131.3(p-Ph), 165.6(C=O).

$Eu(DBM)_3$.phen: ^1H NMR (250 MHz, $CDCl_3$, 25°C): δ = 3.22(s, 3H, 2-CH), 6.19(bs, 12H, o-Ph), 6.84(bs, 18H, m-Ph and p-Ph), 8.94(d, J=7.5Hz, 2H, 3,8-H), 10.19(bs, 2H, 2,9-H), 10.61(s, 2H, 5,6-H), 10.96(d, J=7.7Hz, 2H, 4,7-H). ^{13}C NMR (69 MHz, $CDCl_3$, 25°C): δ = 60.2(2-CH), 93.1(i-Ph), 109.6(3,8-C), 116.8(4a,6a-C), 124.6(m-Ph), 124.8(o-Ph), 129.3(5,6-C), 130.8(p-Ph), 150.3(4,7-C), 168.1(10a,10b-C), 173.0(C=O), 180.3(2,9-C).

$Eu(DBM)_3$.dpp: ^1H NMR (250 MHz, $CDCl_3$, 25°C): δ = 3.26(s, 3H, 2-CH), 6.22(bs, 12H, o-Ph), 6.86(bs, 18H, m-Ph and p-Ph), 8.09(bs, 2H, p-Ar), 8.36(bs, 4H, m-Ar), 8.90(bs, 2H, 3,8-H), 9.06(bs, 4H, o-Ar), 10.13(bs, 2H, 5,6-H), 11.34(s, 2H, 2,9-H). ^{13}C NMR (69 MHz, $CDCl_3$, 25°C): δ = 60.7(2-CH), 93.6(i-Ph), 110.8(3,8-C), 111.5(4a,6a-C), 124.6(m-Ph), 124.8(o-Ph), 126.4(5,6-C), 129.7(m-Ar), 130.0(p-Ar), 130.8(p-Ph), 133.1(o-Ar), 162.4(10a,10b-C), 173.7(C=O), 183.2(2,9-C).

3. RESULTS AND DISCUSSION

X-ray diffractometry

The X-ray diffractogram of the powdered $Eu(DBM)_3$ is shown on Fig. 1. The interplanar distances (d) and the relative intensities of the

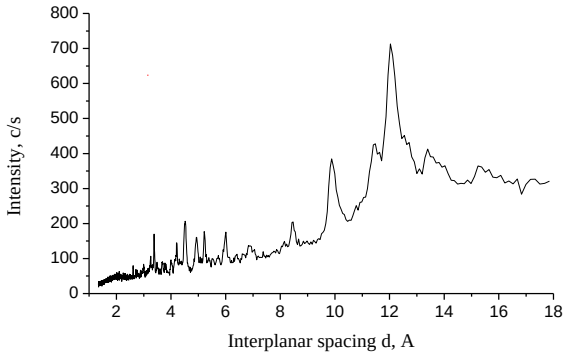

Fig. 1. X-ray diffractogram of $Eu(DBM)_3$.

peaks are shown in Table 1 compared with the data for HDBM (JCPDS 34-1688), $La(DBM)_3$ and $Tb(DBM)_3$ evaluated from the X-ray diffractogram picture reported in [5]. It is seen that the diffractograms of the complexes of the different lanthanides are similar and rather different from that of the pure ligand. The interplanar distances are large as could be expected accounting for the large ligand size. The crystallization is not completed and X-ray amorphous phase exists in the sample studied. Introducing an additional large ligand in $Eu(DBM)_3$.dpp inhibits the crystallization and the complex is X-ray amorphous.

NMR spectroscopy

The coordination mode of the lanthanide ion in solution was examined by measuring ^1H, ^{13}C, ^{13}C DEPT and ^1H,^{13}C-HSQC (250 MHz)/HMQC (400 MHz) NMR spectra of the complexes. All NMR spectra confirmed the structure and purity of the target complexes.

Table 1. Interplanar distances (d, Å) and relative intensities (I, %) for dibenzoylmehane (HDBM) and $Ln(DBM)_3$

HDBM (JCPDS 32-1641)		$La(DBM)_3$ [5][1]		$Tb(DBM)_3$ [5] [1]		$Eu(DBM)_3$	
d	I	d	I	d	I	d	I
5.41	90	11.00	100	15.40	100	15.23	51
5.27	30	6.62	61	12.83	67	13.41	57
5.20	100	5.50	72	7.70	74	12.02	100
4.52	40	4.81	60	7.00	51	11.48	19
4.30	18	4.28	86	5.13	69	9.88	68
4.11	40	4.05	51	4.53	65	8.47	22
						6.90	15
3.97	25	3.67	68	3.85	73	6.01	26
3.84	10	3.50	64	3.50	75	5.21	30
3.619	65	3.35	31	3.21	61	4.93	23
3.368	14	3.21	51	3.08	75	4.52	42
3.132	25	3.08	48	2.96	43	4.20	18
		2.85	55			3.38	35
						3.26	13

[1] The data are evaluated from the published diffractogram [5].

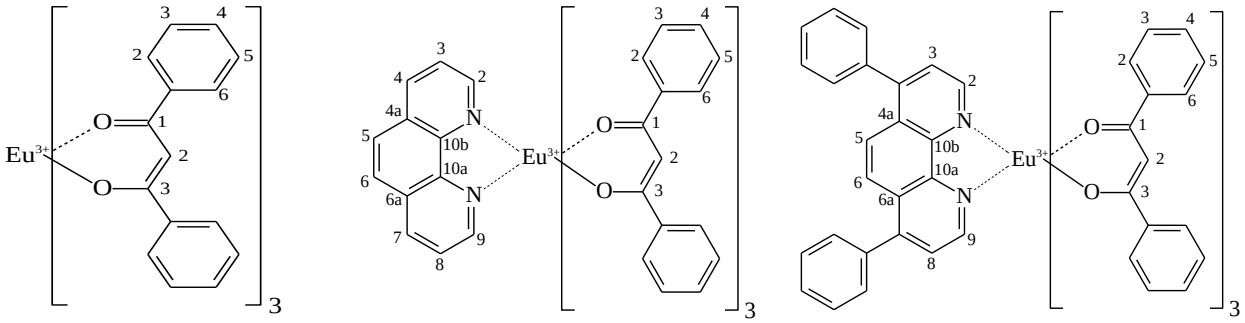

$Eu(DBM)_3$ $Eu(DBM)_3$.phen $Eu(DBM)_3$.dpp

Fig. 2. Structure and numbering of the studied complexes.

The structure and numbering of the studied complexes are shown on Fig. 2. The peaks assignments are presented in the experimental section.

The integral intensity of the peaks in proton spectra is in good agreement with the number of hydrogen atoms in the studied complexes. The signals at 2.30 ppm in $Eu(DBM)_3$, 3.22 ppm in $Eu(DBM)_3$.phen and 3.26 ppm in $Eu(DBM)_3$.dpp were assigned to 2-CH protons in the complexes. Recently, chemical shifts of β-protons in Eu(III) complexes with β-diketonates were reported in the range of 2.74 to 3.43 ppm [17]. The peaks of aromatic protons for the Eu(III) complexes are shifted to a higher field, compared to the same peaks in the spectra of the starting ligands. That is due to the strong paramagnetic properties of the Eu(III) ions which usually deshield the adjacent nuclei in the second coordination sphere. In the studied complexes the ligands are directly

coordinated to Eu(III) and the Fermi contact term is expected to prevail over the pseudocontact shifts and therefore the resonances are shifted upfield [18]. In fact, such kind of β-diketonate complexes of Eu(III) are lanthanide shift reagents and can be used for transforming second order NMR spectra into first order [18].

The expected ^{1}H NMR resonances of aromatic protons are significantly broadened upon coordination. There is no change in the symmetry of ligands upon coordination and all resonances are in the same form and position as for free ligands, indicating uniform interaction of all C=O groups with Eu(III) ion within the ^{1}H NMR time scale.

All ^{1}H and ^{13}C NMR spectra of $Eu(DBM)_3$, $Eu(DBM)_3$.phen and $Eu(DBM)_3$.dpp complexes are clean from peaks of free ligands, indicating the completeness of the complexation process.

Determination of the content of water in the complex is possible comparing the signal intensities of the shifts at 2.3 ppm (s, 3H, 2-CH) and at 3.96 ppm in the spectrum taken from solution of the complex in dry DMF. The latter signal belongs to hydrogen which is not correlated with carbon and is ascribed [4] to the hydrogen from water. (The proton from the enolic form of the ligand, the only alternative source of the 3.96 ppm shift, exhibits at 16.89 ppm [14]). It was shown by this way that a complex dried at a pressure of ~3 kPa contains ~1 mol H_2O/mol complex. The routine synthetic procedure, described in the Experimental part, requires the drying to be performed at 0.7 Pa. If this procedure is followed, the final product is practically anhydrous.

4. CONCLUSIONS

The X-ray powder diffraction pattern of Eu $(DBM)_3$ is reported for the first time. ^{1}H, ^{13}C spectra of $Eu(DBM)_3$, $Eu(DBM)_3$.phen and $Eu(DBM)_3$.dpp are interpreted in details. The capability of the NMR study concerning determination of stoichiometry of the complexes, coordination mode, presence of water and free ligands in the final product is shown.

The measured ^{1}H and ^{13}C NMR and ^{1}H,^{13}C HSQC spectra of $Eu(DBM)_3$ in DMF-d7, $Eu(DBM)_3$ phen in $CDCl_3$ and of $Eu(DBM)_3$.dpp in $CDCl_3$ are available as supporting materials from the authors upon request.

Acknowledgements: *The work is performed with the financial support of the Bulgarian Fund for Scientific Investigation (contract VUH 05/2005) and by the contract for bilateral co-operation between the Saarland University and University of Sofia.*

REFERENCES

1. J.-C. G. Bünzli, E. Moret, V. Foiret, K. J. Schenk, W. Mingzhao, J. Linpei, *J. Alloys Comp*. **207/208**, 107 (1994).
2. K. Binnemans, in: Handbook on the Physics and Chemistry of Rare Earths, Vol. 35, K.A. Gschneidner, Jr., J.-C.G. Bünzli, V.K. Pecharsky Eds., Chapter 225, p. 111, Elsevier, 2005.
3. K. Binnemans, *Chem. Rev*. **109**, 4283 (2009).
4. J. Zaharieva, M. Milanova, D. Todorovsky, Synthesis Reactivity Inorganic, Metal-Organic, Nano-Metal Chemistry (2010) (in press).
5. Lu Jingci, Y. Kelan, Ch. Junsheng, L. Chongshan, Su Qingde, *J. Shanghai Univ*. **3**, 167 (1999).
6. C. R. Hurt, N. McAvoy, S. Bjorklund, N. Filipescu, *Nature*, **212**, 179 (1966).
7. Xi-R. Zeng, R.-G. Xiong, X.-Z. You, K. K. Cheung, *Inorg. Chem. Commun*. **3**, 341 (2000).
8. L. M. Sweeting, A. L. Rheingold, *J. Am. Chem. Soc*., **109**, 2562 (1987).
9. F. A. Cotton, L. M. Daniels, P. Huang, *Inorg. Chem. Commun*., **4**, 319 (2001).
10. L. M. Sweeting, A. L. Rheingold, *J. Phys. Chem*. **92**, 5648 (1988).
11. X.-F. Chen, X.-H. Zhu, R. S. S. Sundara, S. Oztturk, H.-K. Fun, X.-Z. You, *J. Mater. Chem*., **9**, 2919 (1999).
12. R.-G. Xiong, X.-Z. You, *Inorg. Chem. Commun*., **5**, 677 (2002).
13. M. Milanova, J. Zaharieva, B. Morgenstern, K. Hegetschweiler, D. Todorovsky, *Z. Kristallogr*., NCS 225 (2010), 17-22/ DOI 10.1524/ ncrs.2010.008.
14. M. O. Ahmed, J.-L. Liao, X. Chen, S.-An Chen, J. H. Kaldis, *Acta Cryst*., **E59**, m29-m32 (2003).
15. L. R. Melby, N. J. Rose, E. Abramson, J. C. Caris, *J. Am. Chem. Society*, 5117 (1964).
16. Q.G. Meng, L.S. Fu, S.B. Wang, H. J. Zhang, H. R. Li, X. H. Chuai, Y.H. Li, S.Y. Zhang, *Thin Solid Films* **388**, 87 (2001).
17. S. Stanimirov, A. Vasilev, E. Haupt, I. Petkov, T. Deligeorgiev, *J. Fluoresc.*, **19**, 85 (2009).
18. S. P. Babailov, Yu. G. Krieger, *J. Structural Chem*., **39**, 580 (1998).

РЕНТГЕНО-ДИФРАКТОМЕТРИЧНИ И ЯМР ИЗСЛЕДВАНИЯ НА ЕВРОПИЕВИ ДИБЕНЗОИЛ-МЕТАНАТИ

Й. Цв. Захариева, М. М. Миланова, Н. Василев[1], Б. Моргенщерн[2], Д. Ст. Тодоровски*

Химически факултет, Софийски университет, бул. Дж. Баучер 1, София 1164, България
[1] Институт по органична химия с Център по фитохимия, Българска академия на науките, ул. Г. Бончев, бл. 9, София 1113, България
[2] Катедра Неорганична химия, Саарландски университет, Саарбрюкен 66123, Германия

(Резюме)

В работата за пръв път се съобщават праховите рентгенограми на комплекса на европия $Eu(DBM)_3$ (DBM – дибензоилметан). Показано е, че смесено-лигандният комплекс $Eu(DBM)_3$.dpp (dpp – 1,4-дифенил-1,10-фенантролин) е рентгено-аморфен. ^1H и ^{13}C ЯМР спектрите на $Eu(DBM)_3$, $Eu(DBM)_3$.phen (phen - 1,10-фенантролин) и $Eu(DBM)_3$.dpp са интерпретирани и е показана тяхната приложимост като средство за оценяване на стехиометрията на комплексите, съдържанието на вода в тях и пълнотата на реакцията на синтез.

AUTHOR INDEX

SUBJECT INDEX

АВТОРСКИ УКАЗАТЕЛ

ПРЕДМЕТЕН УКАЗАТЕЛ

BULGARIAN CHEMICAL COMMUNICATIONS

Instructions about Preparation of Manuscripts

General remarks: Manuscripts are submitted in English by e-mail or by mail (in duplicate). The text must be typed double-spaced, on A4 format paper using Times New Roman font size 12, normal character spacing. The manuscript should not exceed 15 pages (about 3500 words), including photographs, tables, drawings, formulae, etc. Authors are requested to use margins of 3 cm on all sides. For mail submission hard copies, made by a clearly legible duplication process, are requested. Manuscripts should be subdivided into labelled sections, e.g. **Introduction, Experimental, Results and Discussion**, *etc*.

The title page comprises headline, author's names and affiliations, abstract and key words.

Attention is drawn to the following:

a) **The title** of the manuscript should reflect concisely the purpose and findings of the work. Abbreviations, symbols, chemical formulas, references and footnotes should be avoided. If indispensable, abbreviations and formulas should be given in parentheses immediately after the respective full form.

b) **The author**'s first and middle name initials, and family name in full should be given, followed by the address (or addresses) of the contributing laboratory (laboratories). **The affiliation** of the author(s) should be listed in detail (no abbreviations!). The author to whom correspondence and/or inquiries should be sent should be indicated by asterisk (*).

The abstract should be self-explanatory and intelligible without any references to the text and containing not more than 250 words. It should be followed by key words (not more than six).

References should be numbered sequentially in the order, in which they are cited in the text. The numbers in the text should be enclosed in brackets [2], [5, 6], [9–12], etc., set on the text line. References, typed with double spacing, are to be listed in numerical order on a separate sheet. All references are to be given in Latin letters. The names of the authors are given without inversion. Titles of journals must be abbreviated according to Chemical Abstracts and given in italics, the volume is typed in bold, the initial page is given and the year in parentheses. Attention is drawn to the following conventions:

a) The names of all authors of a certain publications should be given. The use of "*et al*." in the list of references is not acceptable.

b) Only the initials of the first and middle names should be given.

In the manuscripts, the reference to author(s) of cited works should be made without giving initials, e.g. "Bush and Smith [7] pioneered...". If the reference carries the names of three or more authors it should be quoted as "Bush *et al*. [7]", if Bush is the first author, or as "Bush and co-workers [7]", if Bush is the senior author.

Footnotes should be reduced to a minimum. Each footnote should be typed double-spaced at the bottom of the page, on which its subject is first mentioned.

Tables are numbered with Arabic numerals on the left-hand top. Each table should be referred to in the text. Column headings should be as short as possible but they must define units unambiguously. The units are to be separated from the preceding symbols by a comma or brackets.

Note: The following format should be used when figures, equations, *etc*. are referred to the text (followed by the respective numbers): Fig., Eqns., Table, Scheme.

Schemes and figures. Each manuscript (hard copy) should contain or be accompanied by the respective illustrative material as well as by the respective figure captions in a separate file (sheet). As far as presentation of units is concerned, SI units are to be used. However, some non-SI units are also acceptable, such as °C, ml, l, etc.

The author(s) name(s), the title of the manuscript, the number of drawings, photographs, diagrams, etc., should be written in black pencil on the back of the illustrative material (hard copies) in accordance with the list enclosed. Avoid using more than 6 (12 for reviews, respectively) figures in the manuscript. Since most of the illustrative materials are to be presented as 8-cm wide pictures, attention should be paid that all axis titles, numerals, legend(s) and texts are legible.

The authors are asked to submit **the final text** (after the manuscript has been accepted for

publication) in electronic form either by e-mail or mail on a 3.5'' diskette (CD) using a PC Word-processor. The main text, list of references, tables and figure captions should be saved in separate files (as *.rtf or *.doc) with clearly identifiable file names. It is essential that the name and version of the word-processing program and the format of the text files is clearly indicated. It is recommended that the pictures are presented in *.tif, *.jpg, *.cdr or *.bmp format, the equations are written using "Equation Editor" and chemical reaction schemes are written using ISIS Draw or ChemDraw programme.

The authors are required to submit the final text with a list of three individuals and their e-mail addresses that can be considered by the Editors as potential reviewers. Please, note that the reviewers should be outside the authors' own institution or organization. The Editorial Board of the journal is not obliged to accept these proposals.

EXAMPLES FOR PRESENTATION OF REFERENCES

REFERENCES

1. D. S. Newsome, *Catal. Rev.–Sci. Eng.*, **21**, 275 (1980).
2. C.-H. Lin, C.-Y. Hsu, *J. Chem. Soc. Chem. Commun.*, 1479 (1992).
3. R. G. Parr, W. Yang, Density Functional Theory of Atoms and Molecules, Oxford Univ. Press, New York, 1989.
4. V. Ponec, G. C. Bond, Catalysis by Metals and Alloys (Stud. Surf. Sci. Catal., vol. 95), Elsevier, Amsterdam, 1995.
5. G. Kadinov, S. Todorova, A. Palazov, in: New Frontiers in Catalysis (Proc. 10th Int. Congr. Catal., Budapest, 1992), L. Guczi, F. Solymosi, P. Tetenyi (eds.), Akademiai Kiado, Budapest, 1993, Part C, p. 2817.
6. G. L. C. Maire, F. Garin, in: Catalysis. Science and Technology, J. R. Anderson, M. Boudart (eds), vol. 6, Springer-Verlag, Berlin, 1984, p. 161.
7. D. Pocknell, *GB Patent* 2 207 355 (1949).
8. G. Angelov, PhD Thesis, UCTM, Sofia, 2001.
9. JCPDS International Center for Diffraction Data, Power Diffraction File, Swarthmore, PA, 1991.
10. CA **127**, 184 762q (1998).
11. P. Hou, H. Wise, *J. Catal.*, in press.
12. M. Sinev, private communication.
13. http://www.chemweb.com/alchem/articles/1051611477211.html.

CONTENTS

СЪДЪРЖАНИЕ